NTNU
Norwegian University of
Science and Technology

Numerical Simulations of Flow Around Step Cylinder Configurations

Are Sørbø Wahlstrøm

Marine Technology
Submission date: February 2020
Supervisor: Bjørnar Pettersen, IMT
Co-supervisors: Fengjian Jian and Cai Tian

Norwegian University of Science and Technology
Department of Marine Technology

NTNU
Norwegian University of Science and Technology
Department of Marine Technology

MASTER THESIS IN MARINE HYDRODYNAMICS

SPRING 2020

FOR

Stud.techn. Are Sørbo Wahlstrøm

NUMERICAL SIMULATION OF VISCOUS FLOW AROUND STEP CYLINDERS.

The candidate shall investigate viscous flow around step cylinders using the software FINE/Marine. Initially, a two-dimensional cylinder is going to be implemented and analyzed in order to familiarize with the software and visualization techniques. The effects of different mesh configurations, boundary conditions of the domain and time steps are important to document.

The main study will be done with a cylinder of one or more steps. Special focus should be on the computational domain, grid resolution, and length and diameter ratios. All simulations will be performed with parameters and Reynolds number specified by the candidate. Details in the wake flow should be documented by performing visualization of physical quantities.
The thesis should also include a literature review that will be used in the discussions and comparisons of the results in the thesis.

In the thesis the candidate shall present his personal contribution to the resolution of the problem within the scope of the thesis work. Theories and conclusions should be based on mathematical derivation and logic reasoning identifying the various steps in the deduction. The original contribution of the candidate and material taken from other sources shall be clearly defined. Work from other sources shall be properly referenced. The candidate should utilize the existing possibilities for obtaining relevant literature.
The thesis should be organized in a rational manner to give a clear exposition of results, assessments and conclusions. The text should be brief and to the point, with a clear language.

The thesis shall contain the following elements: A text defining the scope, preface, list of contents, summary, main body of thesis, conclusions with recommendations for further work, list of symbols and acronyms, references and appendices. All figures, tables and equations shall be numerated.
It is supposed that Department of Marine Technology, NTNU, can use the results freely in its research work by referring to the student's thesis.
The thesis shall be submitted February 9th, 2020.

Bjørnar Pettersen
Professor/supervisor

Co-supervisors: Research Scientist Fengjian Jiang, SINTEF Ocean
                   PhD student Cai Tian

Summary

This master thesis presents the research and numerical investigations on the topic of viscous flow around circular cylinders, and step cylinders. The first part of the thesis works as an introduction to the theory of viscous fluid flows and the main concepts behind flow around circular cylinders. The next part of the thesis involves a literature review presenting the most relevant research and findings from studies performed for the main topics of this thesis. Moreover, an introduction to computational fluid dynamics is given, as well as the theory behind the numerical framework of CFD-solvers. The actual simulations in this thesis were performed in the CFD-software FINE/Marine. Geometry, computational domain and mesh configuration is performed in HEXPRESS, the numerical solving is performed with the ISIS-CFD solver, and the post-processing is performed in CFView. All mentioned components are a part of the software designed by NUMECA. The main objective of the thesis is to explore the flow development around circular step cylinders of different lengths.

An initial two-dimensional validation case was performed in order to gain more confidence in the software and the numerical framework of FINE/Marine. The results from the case study showed the importance of grid refinement, computational domain setup, and time step analysis. Solution convergence studies gave satisfactory results, which created the important foundation of the simulation model, with the transition to three-dimensional geometries.

Simulations were then performed for three-dimensional single step and dual step cylinders at Reynolds number 150 and diameter ratio D/d = 5. The initial simulations for the 5D step cylinder showed little effect of the step, as the spanwise length was to small to capture the full development in the wake. However, first signs of downwash from the step were visible. For the 10 and 15D step cylinders, the effect of the step was very visible. The disturbance from the step created significant downwash, and oblique shedding was clearly visible in the wake behind the large step. The fine mesh that was applied in the region around the step and in the wake of the cylinders gave satisfactory results. The flow in the junction between the large and the small cylinder was visually rotational, and in agreement with the early stages of junction and edge vortex formation. In addition, the vortex structures in the wake were captured well with the λ_2 vortex detection. The influence of the step was measured to extend as far as 10D into the wake of the large cylinder, also referred to as the N-cell region. Of the more interesting observations made for the 15D step cylinder simulations was the long oscillating drag coefficient frequency that described the vortex dislocation process. The development of the dislocation process was thoroughly described, with results comparable to the important study of (Tian et al., 2017a).

More simulations were conducted for dual step cylinders, with the intent of investigating the influence of different spanwise lengths of the large cylinder. For the 20D cylinder the same vortex dislocation process was observed as for the 15D single step cylinder. With

the contribution from both the upper and the lower step, the L-cell region changed much in size. Moreover, so-called hairpin vortices could be observed in the wake of the large cylinder, with maximum deflection at the "climax" of the dislocation process. As the N-cell region was measured to be approximately 10D at the longest, the L-cell region almost disappeared for the 20D cylinder. Simulations of a 30D dual step cylinder revealed that the N-cell region reached a maximum of 11D from both sides, and that the L-cell region now was 7D. An interesting observation made for the 30D simulations were the streamwise vortex fingers stretching out in the interaction between the N-cell and L-cell regions. The vortices showed resemblance to the modes first described by (Gerrard, 1978).

Sammendrag

Denne masteroppgaven presenterer litterære studier og numeriske undersøkelser av den tredimensjonale viskøse strømningen rundt sirkulære sylindere, og steg-sylindere. Den første delen av oppgaven gir en introduksjon til grunnleggende teori om viskøse strømmer og de grunnleggende konseptene ved strømning rundt sirkulære sylindere. Den neste delen av oppgaven inneholder et grundig litterært studie av den mest relevante forskningen om dette temaet. Videre blir det gitt en introduksjon til CFD og den numeriske grunnmuren i CFD-løsere. De faktiske simuleringene i denne oppgaven har blitt gjennomført i programvaren FINE/Marine. Geometri, domener og gridoppløsning har blitt gjennomført i HEXPRESS, den numeriske løsningen har blitt gjort i ISIS-løseren, og all prosessering av resultatene har blitt gjort i CFView. Alle de nevnte komponentene er en del av programvaren produsert av NUMECA. Hovedmålet med denne masteroppgaven er å undersøke strømningsutviklingen rundt sirkulære steg-sylindere av forskjellig lengde.

En todimensjonal casestudie har blitt brukt som validering for å bli trygg på programvaren, og hvordan man bygger opp en god numerisk modell. Resultatene fra studie synliggjorde viktigheten av gridoppløsning, domene-størrelse og tidssteg-analyser. Konvergenstestene som ble gjennomført gav gode resultater, som igjen skapte et godt grunnlag for den numeriske modellen, spesielt med tanke på videreutviklingen til tredimensjonale geometrier.

Simuleringer ble gjennomført for tredimensjonale steg og to-steg-sylindere for Reynoldstall 150 og diameterforhold D/d =5. De første simuleringene for en 5D steg-sylinder viste liten effekt fra steget, og den korte sylinderlengden gjorde det vanskelig å se påvirkningen til steget i waken. Allikevel kunne man se de første tegnene på nedstrøm fra steget. For 10D og 15D steg-sylinderene var effekten fra steget mye tydeligere. Forstyrrelsene som ble skapt rundt steget skapte betydelig nedstrøm, og skrå avløsning kunne tydelig bli sett i waken bak den store sylinderen. Den fine meshen som ble påført rundt steget og i waken var tilstrekkelig for å få gode resultater. Strømningen i skjøten mellom den store og den lille sylinderen var tydelig roterende, og viste tegn som indikerte et tidlig stadie av skjøt-virvler og kant-virvler. I tillegg kunne man tydelig detektere virvlene som ble skapt i waken. Påvirkningen fra steget ble målt til å strekke seg 10D inn i waken til den store sylinderen, et område som blir kalt for N-cell området. Av de mer interessante observasjonene for steg-sylinderen var den lange oscillerende drag koeffisient-frekvensen. Denne frekvensen var beskrivende for avkoblingsprosessen som skjedde for virvlene i waken. Utviklingen til denne avkoblingsprosessen ble grundig beskrevet, og resultatene var sammenlignbare med studiene gjennomført av (Tian et al., 2017a).

Flere simuleringer ble gjennomført for to-steg sylindere, med en hensikt om å undersøke påvirkningen av forskjellige sylinderlengder for den store sylinderen. For 20D sylinderen ble den samme avkoblingsprosessen observert, som for 15D steg-sylinderen. Med bidrag fra både det øvre og det nedre steget endret L-cell området seg mye i størrelse.

Videre, ble det observert såkalte hårnål-virvler observert i waken til den store sylinderen, med størst utbøying ved klimaks i avkoblingsprosessen. Da N-cell området ble målt til å være på sitt lengste (rundt 10D), forsvant nesten hele L-cell området. Simuleringer for 30D to-steg sylinderen viste at N-cell området nådde en maks lengde på 11D fra begge sider, og at L-cell området da ble rundt 7D. En ytterligere interessant observasjon som ble gjort for 30D sylinderen var horisontale strømnings-fingre som strakk seg ut i interaksjonsområdet mellom N-cell og L-cell området. Disse virvlene kunne minne om modene som tidligere ble beskrevet av (Gerrard, 1978).

Preface

This report is the result of the work done during the autumn term of 2019, and is the final part of my M.Sc. degree in Marine Hydrodynamics at the Department of Marine Technology at the Norwegian Institute of Science and Technology.

The topic of this thesis was proposed by my supervisor Bjørnar Pettersen. He had gathered a highly competent team which made me confident and motivated to dive into the challenges. The underlying motivation of the task was to gain experience in the implementation of Computational Fluid Dynamics to fluid flow problems. I was very motivated by the fact that this thesis could be directly linked to challenges met by the marine industry today.

This master thesis is built on the work done in the project thesis previously written. The whole process has been long but very interesting. Knowing only the basics of CFD, the start was tedious and slow, but after a while and several weeks of trial and error my confidence and experience increased. This master thesis has taught me a lot about the process of researching and writing a scientific report. I am very proud of the things I have accomplished, and the outcome of the thesis, as well as my whole degree!

Finally I would like to express my gratitude to my supervisor Professor Bjørnar Pettersen, and my two co-supervisors Research Scientist Fengjian Jian and PhD student Cai Tian. I have been very fortunate to have such competent and experienced supervisors. The weekly meetings have been very important and valuable for the progress in the thesis, and our conversations have been very helpful and motivating.

Are Sørbø Wahlstrøm
Trondheim, February 9, 2020

Table of Contents

Nomenclature

Abbreviations

2D	Two Dimensional
3D	Three Dimensional
BC	Boundary Conditions
CFD	Computational Fluid Dynamics
CV	Control Volume
FDM	Finite Difference Method
FEM	Finite Element Method
FVM	Finite Volume Method
Ref. no.	Number of refinements
NS	Navier-Stokes
ODE	Ordinary Differential Equations
PDE	Partial Differential Equations
RANS	Reynolds Averaged Navier Stokes
RMS	Root Mean Square
VIV	Vortex Induced Vibrations

Symbol list

C_D	Drag coefficient
C_L	Lift coefficient
δ	Boundary Layer Thickness
ν	Kinematic viscosity
μ	Dynamic viscosity
U	Uniform flow velocity
u	Velocity component x-direction
v	Velocity component y-direction
w	Velocity component z-direction
ρ	Fluid density
$\Delta_{X1}, \Delta_{X2}, \Delta_{X3}$	Initial mesh size
f	Frequency
St	Strouhal number
Re	Reynolds number
f_V	Vortex shedding frequency
F_D	Drag force
F_L	Lift force
p	Lift force
T_V	Vortex shedding period
p	Pressure
D	Large cylinder diameter
d	Small cylinder diameter
L	Large cylinder length
l	Small cylinder length

Chapter 1

Introduction

Offshore hydrocarbon extraction has had a large impact on the marine industry, and especially in countries where oil reservoirs are located at deeper water, like in Norway. As the extraction and production is moving to larger depths, new challenges arise. The most common method to extract oil and gas from the reservoirs at the sea bed is through risers. For this reason the offshore industry is interested in reliable and efficient riser configurations that are tailor made for the harsh weather conditions in the exposed areas far away from land. Among the challenges the industry has to face is the phenomenon of vortex induced vibrations (VIV). VIV may occur when ocean currents flow past the cylindrical riser, and vortices are shed. More specifically, due to varying pressure gradients on the surface of the riser, oscillating forces are induced, creating movement in the structure. If the frequency of the forces are close to the natural frequency of the structure, resonance will occur, causing large amplification of motions, which again may lead to fatal fatigue and material damage.
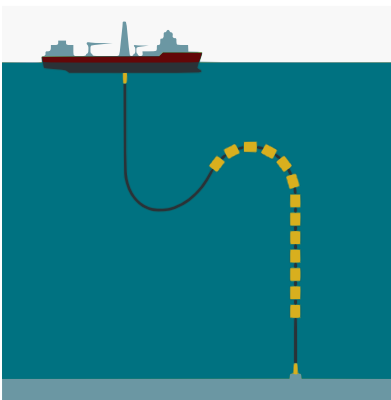
(a) Riser from ship to reservoir
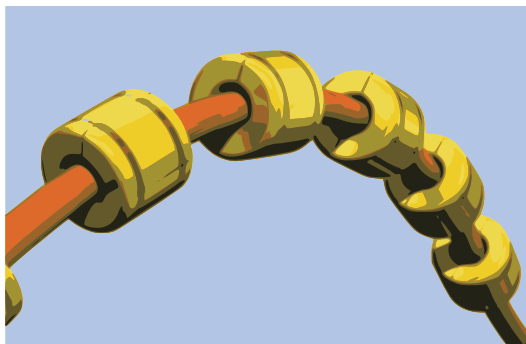
(b) Buoyancy elements on riser

Figure 1.1: Riser configuration on offshore installations

The industry today faces a complicated task trying to understand the nature of vortex induced vibrations. Three dimensional flow patterns are highly complex, and for more complicated structures the complexity of the flow increases. However, even though the challenge of simulating complex flow patterns require a lot of resources, it is important to understand the physics in order to prevent damage or economical loss.

In the offshore oil industry today different solutions have been developed in order to relieve the turret at the platform/FPSO from the heavy load of the long riser. A common solution to minimize the vertical top tension of the riser is by use of buoyancy elements, as shown in Figure 1.1a and 1.1b. By introducing the buoyancy elements to the riser, the complexity of the flow regime increases, and new methods must be developed to model the structure. Discretising the structure from the surface to the sea bed makes it possible to model and analyse separate parts with simpler geometries. Many studies have been conducted on the topic of uniform flow past cylindrical structures of different configurations, both straight and curved. However, fewer have investigated the effects of adding cylindrical components of different diameter to the cylinder. The structural configuration with the buoyancy elements on the riser can be represented by a more simple geometry, namely a step cylinder. A step cylinder is a geometry consisting of two cylinders with circular cross section and of different diameters. Fluid flow problems with this configuration has received increasing attention in research lately, mostly because of its wide application in the marine industry. The results from the research show great promise, but there are still aspects that needs to be investigated further.

1.1 Scope of the thesis

The scope of this master thesis is to investigate how the geometrical properties of the step cylinder affect the flow regime, and thus how the pressure and forces act on the structure. The method that will be used in the research is numerical simulations performed in a computer software called FINE/Marine.

The first part of the thesis will include an introduction to the relevant background theory of fluid dynamics. It is important to establish a good theoretical foundation in order to validate and draw conclusions from the results obtained in the research. In addition to the theoretical background there will be included a thorough research and presentation of earlier similar studies on the same topic. This chapter is of high relevance, as it is the main source of validation and verification of this thesis.

Working with numerical simulations and computational fluid dynamics (CFD) requires experience through practice, as there are few shortcuts. It is also important to build up a basic understanding of the most important concepts, how they are integrated in the software, and how they affect the solution of the model. For this reason the thesis is constructed from the foundation of CFD, all the way up to a solid high performance simulation model. The groundwork of the research includes exploring the computer aided design tool (CAD), constructing a suitable mesh, investigating different domain configurations and simulation

parameters. The initial simulations are of very high importance as they give a good understanding of the physics of the model, and how it reacts to changes and tuning.

This thesis will investigate the effects of change in lengths in the cylindrical structure, primarily at low Reynolds numbers. The simulations will be performed for several geometrical properties, with change in cylinder length for both single and dual step cylinders. The results from the simulations will be compared against findings in earlier studies to draw conclusions of possible similarities or deviations. This master thesis will hopefully contribute to the research concerning flow over cylindrical structures, and create a wider resolution of the flow problem of step cylinders. The following list gives a brief description of the structure of the thesis:

- **Introduction**

- **Chapter 2:** This chapter introduces the theoretical background that forms the basis of the thesis. The theoretical concepts of viscous fluid flow phenomena are presented, as well as the numerical framework that is required for the understanding of the results from the simulations.

- **Chapter 3:** In this chapter a literature review is included. The review presents the most relevant and recent research on the topic of flow around both straight cylinders, single and dual step cylinders. The review includes results from both numerical simulations and experimental studies.

- **Chapter 4:** This section introduces the theory behind computational fluid dynamics, with the governing equations, boundary conditions, and the numerical framework that is the foundation of the numerical solver.

- **Chapter 5:** Introduction to the software FINE/Marine, and primary construction of the model. In this section the most important parameters are explored. These include; investigating choice of mesh size and mesh configuration, defining an appropriate computational domain, establishing boundary conditions and selecting a sufficient time step.

- **Chapter 6:** Simulation of single and dual step cylinders with simulation set up, results and discussion.

- **Chapter 7:** Conclusion and summary of the results and the discussion. In this section there is also included suggestions to further work.

- **Appendix:** Additional figures, plots and codes

Arguably one of the better ways to study flow around geometric figures is by visualization methods, plots and figures. For that reason animations have been made on the results from the simulations. All the simulation files, images and additional scripts are delivered to the supervisor Bjørnar Pettersen for storage, and further work.

Chapter 2

Theoretical background

This chapter is included to serve as a introduction to the world of fluid dynamics, and to present the necessary background theory required to discuss the observations and conclusions drawn from the results of the numerical simulations performed later in the thesis.

2.1 Fluid flow

The contribution to fluid mechanics theory can be dated back to 285 B.C. when the Greek mathematician Archimedes formulated the principle of buoyancy. Since then there has been published numerous books, papers and articles on the topic of fluid mechanics. Many of the fluid principles and laws we know and use today exist as a result of the scientific research done the last 500 years. Sir Isaac Newton formulated the laws of motion of fluids, and studied fluid inertia, resistance and viscosity. Later, based on Newtons work Daniel Bernoulli and Leonard Euler defined the energy and momentum equations (Cengel and Cimbala, 2010).

The French and English scientific communities were great contributors to the fast developing field of fluid flow theory, with the work of Louis Navier and George Stokes as one of the highlights with the famous equations of motion of fluids. The differences between laminar and turbulent flow were examined by Gotthilf Hagen, and later Lord Osborne Reynolds developed the dimensionless number predicting flow patterns in different fluid situations. In the late nineteenth century a large number of problems were investigated. These included dimensional analysis, vortex motion and irrotational flow, cavitation and wave mechanics.

A discovery that had a huge impact and a significant influence on later research was the work done by the German Ludwig Prandtl. He showed that a fluid flow can be divided into two parts. A layer near a boundary called a *boundary layer*, where friction effects are dominant, and an outer layer where friction is more or less negligible or inviscid and the Euler and Bernoulli equations are applicable (Cengel and Cimbala, 2010).

2.2 Potential flow

Potential flow, or potential theory is based on the assumption of the fluid being irrotational, inviscid and incompressible. Potential theory is based on time independent solutions with the flow velocity being the gradient of the potential satisfying Laplace's equation. The fact that the fluid is assumed inviscid means that the boundary layer that Prandtl described is non-existing, which implicates that there are no drag forces acting on the body, thus the total force will be zero (D'Alemberts paradox).
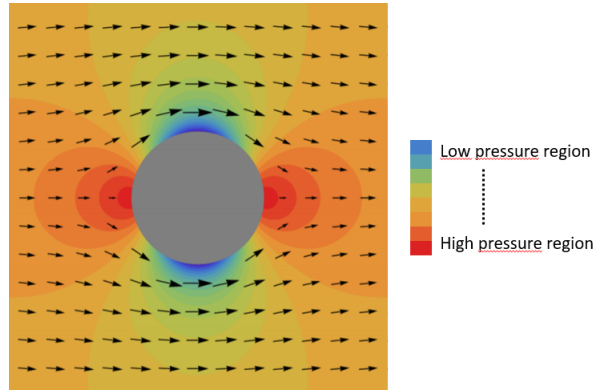
Figure 2.1: Potential plow over cylinder, pressure contour

Figure 2.1 shows the flow characteristics around a circular body when potential theory is applied. The flow follows the curve of the cylinder, and there are indications of high pressure on both sides of the body in streamwise direction. The high pressure behind the body appears as a result of the potential theory equations inability to take into account the viscosity of the fluid. It is also the reason why there are no drag forces exerted to the body. Potential theory can give a good description of the flow outside the boundary layer, but has limitations in the viscous area near the body.

2.3 Viscous flow

Different from potential flow theory, viscous flow theory takes into account the viscosity of the fluid. In almost all cases, a fluid has a certain degree of viscosity that will affect the flow in a particular way. One of the most important properties of a viscous flow is the frictional effects that leads to the phenomenon called no-slip, or the no-slip condition. This condition involves the friction between the fluid particles and the surface of a physical wall. The viscosity makes the fluid stick to the wall, meaning all the velocity components at the surface of the wall are equal to zero. Moving away from the wall the velocity components gradually develop until they reach the free stream velocity. The region of reduced velocity close to the wall is called the boundary layer. The boundary layer is dominated by the viscous forces and are highly dependent on the flow properties, as will be demonstrated later. Related to the boundary layer is the phenomenon of flow separation.

Separation occur when the velocity of the fluid particles on the surface is reversed. This phenomenon is very important in fluid theory as it initiates the process of vortex shedding and wake disturbances for bluff bodies in particular. A precondition for these vortices to appear is rotationality, another feature that is included in viscous flow theory. All the mentioned features of viscous flow theory are dominating for the problem description of this thesis, namely flow around cylindrical structures. Therefore the different phenomena will be explained in more detail in the following sections.

2.4 Flow around a circular cylinder

This thesis will surround the topic of flow past circular cylinders. The next sections will be used to explain and describe the characteristics of the flow past a blunt object. The circular cylinder will be used as a tool of highlighting the main properties and the above mentioned phenomena that appear when a steady incident flow passes the object. In a comprehensive study of flow around circular cylinders (Zdravkovich, 1997) describes and categorises four different flow regions. He defines the narrow region in front of the cylinder where the velocity is retarded (the stagnation), the boundary layer created along the surface of the cylinder that leads to flow separation, the regions above and below the cylinder where the flow accelerates, and finally the wide region downstream of the cylinder called the wake.
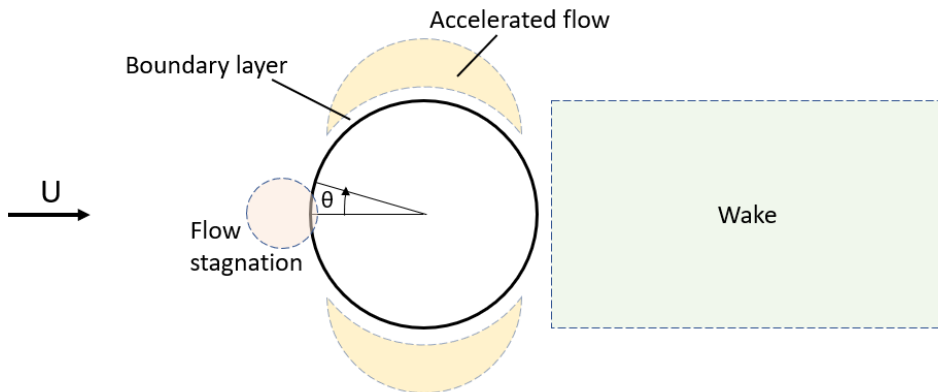
Figure 2.2: Steady state incident flow past a circular cylinder with respective flow regions

Figure 2.2 shows a sketch of a steady incident flow past a circular cylinder. In the figure the four important flow regions are highlighted. U is the incident flow velocity, and θ is the angular coordinate. This value will be used to indicate the locations along the cylinder surface, where $\theta = 0$ corresponds to the forward stagnation point on the cylinder.

2.4.1 Reynolds number

The Reynolds number contains the main parameters influencing the flow characteristics. It is a dimensionless number used to describe the characteristics of different flow situations.

$$Re = \frac{UD}{\nu} = \frac{\rho UD}{\mu} \tag{2.1}$$

The U is the characteristic free-stream velocity, D is the characteristic length of the body the flow is passing and ν is the kinematic viscosity. The equation can also be written in terms of dynamic or absolute viscosity μ, which is a product of the kinematic viscosity and the fluid density ρ. In addition to these important variables other factors influence the flow. Examples are; *roughness number* k/D, body shape, free-surface effects or sea floor effects (Faltinsen, 1990).

Reynolds number expresses the relation between inertia forces and viscous forces in the fluid. If the free-stream velocity U is low, the flow is dominated by viscous forces, and if the velocity is high the inertia forces are most dominant. Reynolds number also gives an indication of the dynamic stability of the flow. At low Reynolds numbers the flow is smooth and predictable (laminar). For high Reynolds numbers the flow is chaotic and unpredictable (turbulent). These phenomena are very important in the world of fluid mechanics, and must be given more attention in the theory description.

2.5 Laminar and turbulent flow

As mentioned, the main difference between laminar and turbulent flow is the degree of order or disorder. Laminar flow can be characterized by the fluid particles moving in smooth layers, with every layer moving alongside the adjacent layers with little or no interaction between the layers. Laminar flow usually occurs for lower velocity flows, but as the Reynolds number tells us, the flow is also highly dependent on geometry dimensions and viscosity. Turbulent flow however, is characterized by a higher level of disorder, and the formation of swirling regions called eddies. These eddies cause rapid fluctuations in pressure and velocity in the flow, which again provide additional mechanisms for momentum and energy transfer. A laminar flow transfers energy across the streamlines by molecular diffusion, different to turbulent flow which transfers energy and momentum through the eddies to other regions in the flow. The result is higher values of friction, heat transfer and mass transfer (Cengel and Cimbala, 2010).

Non-linear effects are the reasons for the fluctuations of velocity and pressure, and arise from the acceleration term in the Navier-Stokes equation. Because of their random nature the fluctuations can only be expressed by statistical means, which calls for empirical models to describe the turbulent flow, rather than a pure numerical approach.

As the kinetic energy in the flow is converted into internal energy by viscous shear stress, the turbulence dissipates rapidly. In order for the flow to sustain its turbulence it requires a persistent source of energy supply. The energy in a turbulent flow is as mentioned

stored and transported in the eddies. The large-scale structures hold most of the energy. The energy then cascades down an "eddy hierarchy", from the large-scale to form smaller and smaller structures. Eventually, the structures reach a small enough scale for viscous dissipation to take place, the Kolmogorov length scale (Landahl and Mollo-Christensen, 1992). The theory about energy dissipation and the creation of large and small scale eddies in turbulent flows is very important. It gives us an understanding of how we can model the turbulence in a flow when we are working with CFD. For instance, if we were to solve the Navier-Stokes equations with a direct numerical simulation (DNS), the grid size would have to be very small in order to capture the effects of the smallest scale structures. With a turbulence model however, it is possible to simulate how the flow will react in the most turbulent areas. As the Reynolds number increases in a flow, the level of turbulence increases, and the requirement of good, robust turbulence models is evident. The theory and application of such turbulence models will be discussed later in this chapter.
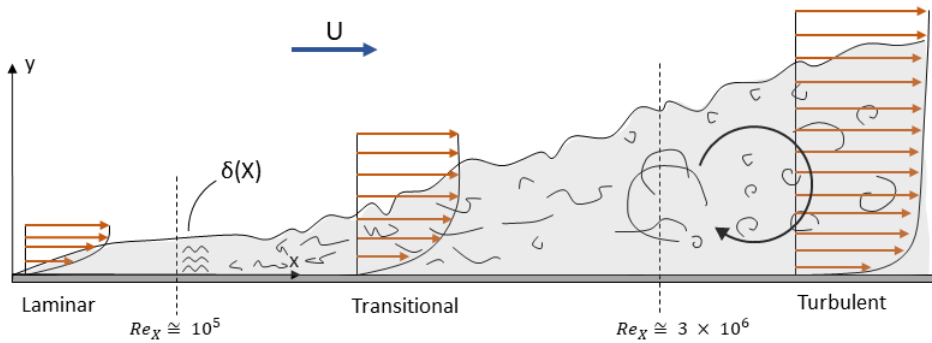
2.5.1 Boundary layer

As mentioned earlier potential flow theory does not take into account the viscosity of the fluid, and can therefore not give the correct solution for the forces on a body. Prandtl introduced the theory of a boundary layer appearing close to the surface of the body. The layer appears as a result of the tangential velocity being zero on the cylinder surface which origins from the no-slip condition. The velocity will gradually increase as we move away from the surface, and eventually it reaches approximately the same velocity as the free stream outside the boundary layer. Figure 2.3 shows how the boundary layer develops along a surface, and how the tangential velocity is zero at the wall, and 0.99U just outside the layer (Faltinsen, 1990). The distance from the surface of the body to the free stream is called the *boundary layer thickness*, δ.
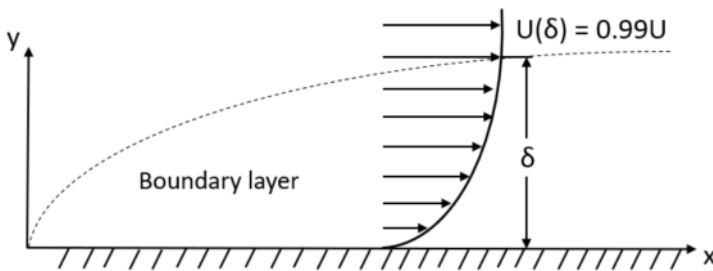
Figure 2.3: Example of tangential velocity inside steady laminar boundary layer

The boundary layer is dominated by the viscous forces, and the tangential shear stress at the surface, $\tau_W = u\frac{du}{dy}$, depends on the velocity gradient $\frac{du}{dy}$. This indicates that the boundary layer to a large degree is influenced by the defining properties of the flow, or in other words, Reynolds number. Evidently, the boundary layer can be both laminar and turbulent. The boundary layer flow will only be laminar up to a certain Reynolds number, beyond which transition to turbulence occurs. Figure 2.4 shows an illustration of the mentioned transition between a laminar and turbulent boundary layer.

Figure 2.4: Transition of the laminar boundary layer on a flat plate into a fully turbulent boundary layer, (Cengel and Cimbala, 2010)

The figure shows the development of the boundary layer along a flat plate. In order to highlight the three different "events" in the development, the figure is divided into three regions of different Reynolds number. The local Reynolds number Re_x marks the transition from one region in the boundary layer to another, namely from laminar to transitional, and from transitional to turbulent. At Reynolds numbers up to approximately 10^5 the boundary layer is laminar and ordered. As the Reynolds number increases the boundary layer becomes more turbulent, and at approximately $3 \cdot 10^6$ it is fully turbulent. It is worth mentioning that the figure is not to scale as the vertical length is greatly exaggerated, and the horizontal length is shortened. In actual scale the boundary layer thickness is very small compared to the characteristic length. It is also worth mentioning that in real-life engineering flows the transition to turbulence occur more abrupt and for lower Reynolds numbers. Factors to cause earlier transition include surface roughness, free-steam disturbances, flow unsteadiness, vibrations and curvature of surface. (Cengel and Cimbala, 2010).

In CFD it is very important to know the theory behind the boundary layer, and how it develops along a surface. In order to observe how a object reacts to the flow surrounding it, it is necessary to capture the smallest details and chances closest to the surface. It is therefore essential to create an sufficiently small mesh close to the surface in order to completely resolve the boundary layer.

Another significant phenomenon connected to the boundary layer is flow separation. Because the flow in the boundary layer has very low energy (relative to the free stream), it is very sensitive to changes in pressure, which may initiate a separation of the boundary layer. A more detailed description will be given later, as this phenomenon is determining for the flow problem in this thesis.

2.5.2 Laminar boundary layer

As mentioned in the beginning of this chapter one of the pioneers in boundary layer theory for flat plates was Ludwig Prandtl. Considering two-dimensional incompressible flow he used nondimensionalized Navier-Stokes equations to derive equations governing the boundary layers. By assuming a large Reynolds number it is possible to determine which terms in the equations of motion that are negligible. The resulting equations of motion in x- and y direction for a laminar boundary layer are:

$$u\frac{\partial u}{\partial x} + v\frac{\partial u}{\partial y} = -\frac{1}{\rho}\frac{\partial p}{\partial x} + \nu\frac{\partial^2 u}{\partial y^2} \tag{2.2}$$

$$\frac{1}{\rho}\frac{\partial p}{\partial y} = 0 \tag{2.3}$$

Equation 2.3 indicates that the pressure is constant throughout the vertical axis of the boundary layer. In x-direction (parallel to the wall) however, the pressure may vary. With this foundation the Bernoulli equation is applicable, and the momentum in x-direction can be further simplified to:

$$\frac{\partial p}{\partial x} = -\rho U\frac{\partial U}{\partial x} \tag{2.4}$$

Differentiating with respect to x, the pressure term is eliminated from the boundary layer equation. This leads to a set of equations of motion for a steady, incompressible, laminar boundary layer:

$$\frac{\partial u}{\partial x} + \frac{\partial v}{\partial y} = 0 \tag{2.5}$$

$$u\frac{\partial u}{\partial x} + v\frac{\partial u}{\partial y} = U\frac{dU}{dx} + \nu\frac{\partial^2 u}{\partial y^2} \tag{2.6}$$

These boundary layer equations provide the foundation for the differential equations derived by the German fluid dynamic physicist, Paul Blasius (White, 2005). He describes a steady two-dimensional laminar boundary layer that forms along a flat plate. By using a numerical approach to solve these differential equations he found exact solutions to the boundary layer thickness.

Knowing information about the thickness of the boundary layer is essential in the process and evaluation of finding the required grid resolution to resolve the boundary layer. Although the Blasius boundary layer equations are derived for a flat plate, they are applicable for different geometries, like curved surfaces. Different to boundary layers on flat surfaces the normal pressure gradient is no longer negligible for curved surfaces. However, in his studies (White, 2005) concludes that as long as the boundary layer thickness δ is considerably smaller than the radius of the curvature, the normal pressure gradient will be equally small, thus the boundary layer equations are valid.

2.5.3 Turbulent boundary layer

Because turbulent flows are unpredictable and unsteady by nature, the time-dependent term in the Navier-Stokes equations cannot be neglected. This makes the derivation of turbulent boundary layer equations complicated. Therefore, in order to describe a turbulent boundary layer, a different approach has to be made. Among the most common techniques to tackle turbulent flows is to apply Reynolds decomposition. With this method the equations are averaged with respect to time and the instantaneous flow properties are decomposed into a mean part and a fluctuating part. By applying the same order of magnitude-analysis as for the laminar boundary layer equations, and assuming that $\delta << L$, it is possible to simplify the momentum equations. The result of Reynolds decomposing leads to equations describing what is referred to as "inner and outer" regions of the boundary layer (Schlichting and Gersten, 2017). Because these to regions are governed by different sets of flow scales (small scale for inner layer close to wall), it has proven to be difficult to find an universal equation for the complete turbulent boundary layer.

An important approach to find a good solution that spans both regions of the flow is to asymptotically match solutions from the two regions. A good boundary layer approximation method is the so-called log-law method. This method was first introduced by the famous physicist Theodore Von Kármán in 1930. The log-law states that the average velocity of a turbulent flow at a certain point is proportional to the logarithm of the distance from the surface to the point. Equation 2.7 is applicable for turbulent flows close to the surface. The variable u* is called the friction velocity, or shear velocity, and it is used to describe motion related to shear forces.

$$\frac{u}{u^*} = \frac{1}{\kappa} \ln\left(\frac{yu^*}{\nu}\right) + B \qquad (2.7)$$

where $\quad u^* = \sqrt{\frac{\tau_w}{\rho}}, \quad$ κ is the Von Kármán constant and B is a constant

In the general log-law formulation it is common to use so-called "inner variables", in this case y^+ and u^+.

$$y^+ = \frac{yu^*}{\nu} \qquad and \qquad u^+ = \frac{u}{u^*} \qquad (2.8)$$

y^+ is a non-dimensional wall coordinate based on the distance from a point y to the wall. u^+ is the dimensionless velocity, based on the velocity u tangential to the wall and the friction velocity. These variables are important in CFD application as they are determining for defining the behaviour of the turbulent boundary layers. Understanding the concept behind the modelling of turbulent boundary layers is very important, especially in the process of applying the computational grid closest to the surface.

The method of log-law approximation has proven to be effective in many applications with turbulent boundary layer flow (Cengel and Cimbala, 2010). In this this thesis the Reynolds numbers will be nowhere near the transition to turbulent boundary layers, thus

the near wall treatment of turbulent boundary layers will not be implemented in the model. However, the importance of knowledge about turbulent boundary layer theory is very important in order to distinguish the two concepts.

2.5.4 Flow separation

As mentioned earlier the boundary layer has very low energy (relative to the free stream), thus it is very sensitive to changes in pressure, which may initiate separation of the boundary layer. Flow separation is the defining phenomenon that develops the characteristics of the vortex formation in the wake behind a cylinder in a flow. The separation occurs as a result of the changing pressure gradient over the length of the body. The upstream portion of the body is subject to a ***favorable pressure gradient***, meaning accelerating velocity U(x) and decreasing pressure P(x). However the downstream portion of the body is subjected to an ***adverse pressure gradient***, meaning decelerating velocity U(x) and increasing pressure P(x). If the adverse pressure gradient is strong enough, the boundary layer is likely to separate from the body (Cengel and Cimbala, 2010).
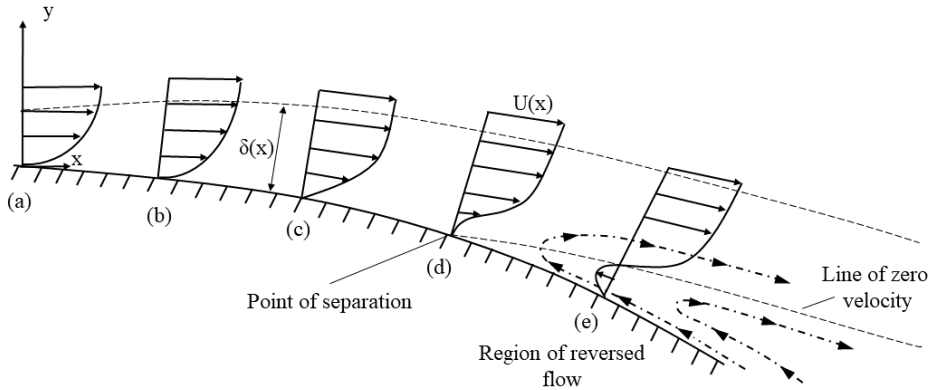
Figure 2.5: Development of boundary layer velocity profiles, point of separation and reversed flow

Figure 2.5 depicts the development of the flow velocity along a cylinder wall. As the flow passes the cylinder the viscous forces (no-slip condition) increase the boundary layer thickness $\delta(x)$. This can be observed in Figure 2.5 (a) (b) and (c).

The following equation is the parabolic x-momentum Navier-Stokes equation.

$$u\frac{\partial u}{\partial x} + v\frac{\partial u}{\partial y} = U\frac{dU}{dx} + \nu\frac{\partial^2 u}{\partial y^2} \tag{2.9}$$

The left side of the equation disappears due to the velocity being zero at the wall (no-slip condition), leaving only the viscous term and the pressure term.

$$\nu(\frac{\partial^2 u}{\partial y^2})_{y=0} = -U\frac{dU}{dx} = \frac{1}{\rho}\frac{dP}{dx} \tag{2.10}$$

If the adverse pressure gradient is large enough, $(\partial u/\partial y)_{y=0}$ in Equation 2.10 becomes zero, which is the place on the body surface the separation point is located. A sketch of the velocity profile at the separation point can be observed in Figure 2.5 (d). Downstream from this point the velocity with the corresponding shear stress will be reversed as the value of $(\partial u/\partial y)_{y=0}$ will be negative. Figure 2.5 (e) shows how the velocity close to the wall has reversed, and that the boundary layer has separated from the surface of the body.

The point on the cylinder surface where the separation occurs is highly dependent on the flow properties, especially Reynolds number. As mentioned in section 2.5.3 the boundary layer will remain laminar up to a certain Reynolds number (approx. 10^5), where the flow becomes unstable and we get a turbulent boundary layer.
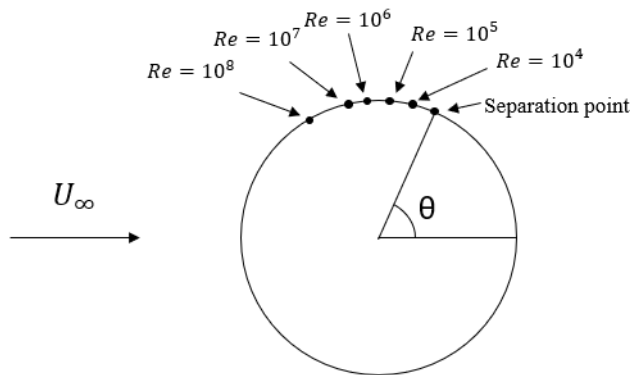
Figure 2.6: Position of instability for different Reynolds numbers Re, incident flow past circular cylinder (Schlichting and Gersten, 2017)

Figure 2.6 shows different points of separation instability on a cylinder for different Reynolds numbers (Schlichting and Gersten, 2017). For the higher Reynolds numbers, the instability will happen further upstream on the cylinder. For laminar flow the separation angle is approximately $\theta = \pm 80°$. It is also worth noting that for supercritical and trans-critical flows dominated by inertial forces the separation point will occur at angles about $\theta = \pm 120°$. Thus we can see that the separation point also will be dependent on Re, and move up and downstream for different Reynolds numbers. The flow separates more easily in a laminar boundary layer than in a turbulent layer.

2.5.5 Wake behavior

The boundary layer and flow separation described in the previous sections are the triggering factors for what happens in the wake of the cylinder. In order to calculate the forces on a body in an incident flow it is important to know how the wake behavior is. When a flow separates from the body it creates a low-pressure region where backflow and recirculating occurs, often called the separated region. This region of reversed flow can be observed at the bottom right in Figure 2.5 (e). The larger this region is, the larger the pressure drag

becomes. The region appears as a result of a free shear layer forming after the separation. This layer is highly dominated by viscous shear stresses which initiates the vorticity. The free shear layers can easily become unstable and turbulent, even if the flow is laminar at the separation point. Behind the separated region is the wake. For a body in incident flow the wake is the "birthplace" for vortices.

2.5.6 Vortex shedding

Research done by (Sumer and Fredsøe, 1997) show that for flow over a circular cylinder with $Re > 49$, the phenomenon of *vortex shedding* will occur as a result of the separation. From an unsteady perspective the eddies created in the wake are alternatively shed from each side of the cylinder and convected with the flow.
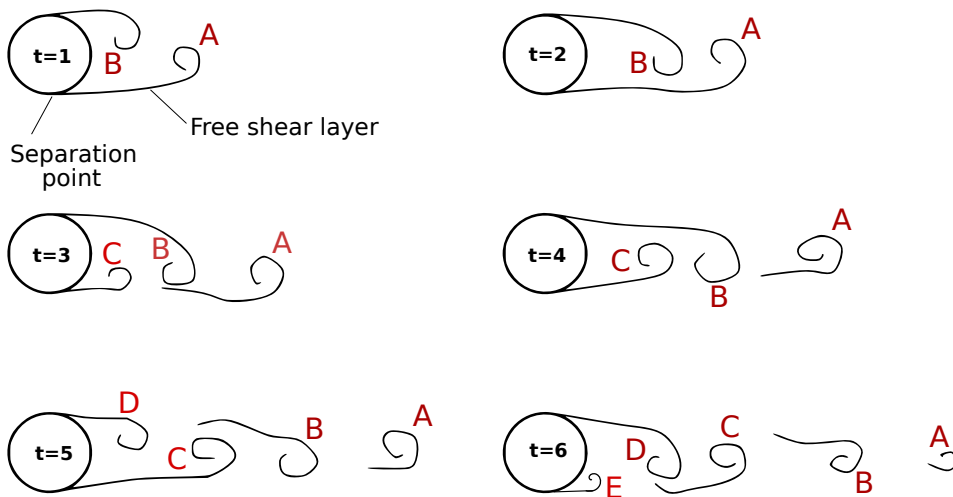
Figure 2.7: Development of periodic vortex shedding for a circular cylinder

Because of the instability of the flow the alternating pattern will occur. Figure 2.7 shows how vortices are typically shed behind a cylinder for different time instances. In this case we are located in the laminar flow regime with Re around 150. Figure (a) shows how one vortex A grows larger, and drags the other vortex B across the wake. When vortex B moves across the wake it cuts of the supply of vorticity to vortex A, which leads to shedding of vortex A. Figure (c) shows how an additional vortex C appears behind the cylinder, and the same procedure is repeated. Vortex C cuts of vortex B, and B is shed. This periodic and alternating pattern continues , and new vortices are created.

The asymmetric pattern in the vortex shedding happens due to the instabilities in the flow. Mathematician Theodore von Kármán studied the stability of the vortex shedding that appeared in the wake of a bluff body. He found that the eddies were situated in two parallel rows forming a "*vortex street*". He concluded that the vortex street is more or less unstable, but can in some cases become stable, depending on the ratio between the vortex street width h and the distance L between two adjacent vortices in the same row (Lamb,

1975). A typical von Kármán vortex street is sketched in Figure 2.8. For a circular cylinder the distance h typically is equal to the cylinder diameter D. The vortex shedding length L is important as it can be used to describe the oscillating flow mechanism.
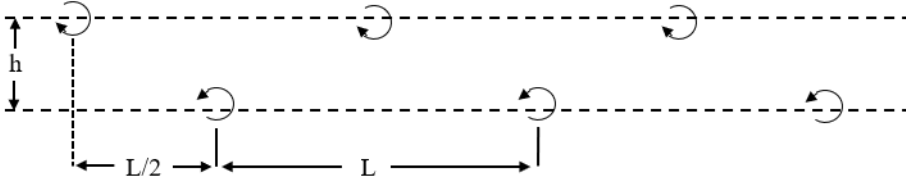

Figure 2.8: Arrangement of vortices in a von Kármán vortex street (Faltinsen, 1990)

The flow theory presented up to this point has mainly been confined to two-dimensional space. However, very interesting effects occur when we enter the three-dimensional space. A flow is considered to be two-dimensional if all the eddy filaments are parallel to the cylinder axis (Zdravkovich, 1997), but in many cases the free shear layers deviate from the parallel plane and shed at an angle. This phenomenon is called oblique shedding, and has been featured in extensive experiments performed by (Williamson, 1992). In many cases the oblique shedding occurs naturally for three dimensional flow of different Reynolds numbers. However, the observations from experiments also show that the oblique shedding may be initiated by disturbances from the boundaries of the geometry, namely end effects from the cylinder setup. By attaching angled end-plates to the experimental setup, Williamson was able to suppress the oblique shedding and induce parallel shedding. The phenomenon of oblique shedding has been featured in many studies, as there are uncertainties on what actually are the triggering effects. Later in the thesis examples of oblique shedding and wake effects will be presented and discussed, both experimental and numerical.

2.5.7   Lift and drag coefficients

The idealized vortex street formulated by von Kármán can be used to estimate the vortex shedding period T_v. The vortex shedding period can again be used to find the vortex shedding frequency f_v. The frequency is defined as $1/T_v$, and is an important component in the non-dimensional Strouhal number which describes the oscillating flow mechanism.

$$St = \frac{f_v D}{U} \tag{2.11}$$
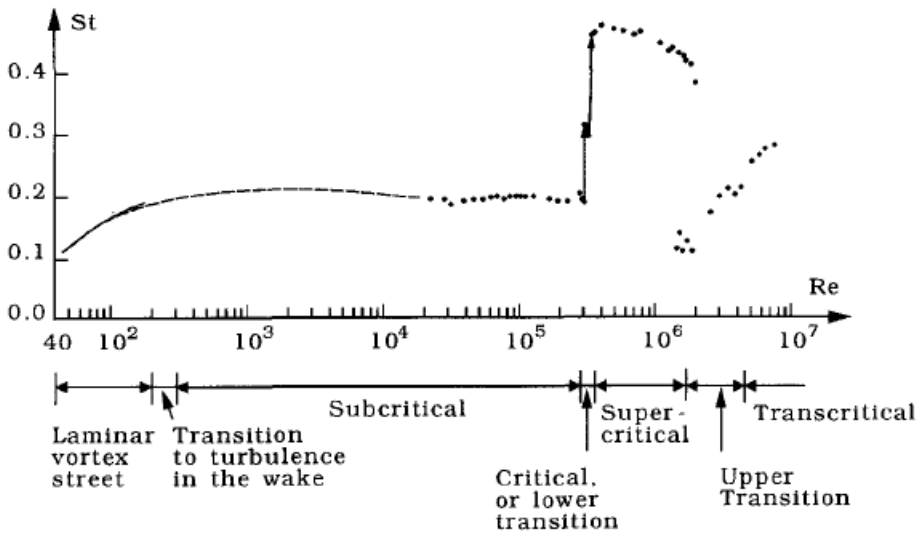
Figure 2.9: Strouhal number for smooth circular cylinder as function of Re. Experimental data from: Solid curve: Williamson (1989), Dashed curve: Roshko (1961), Dots: Schewe (1983) (Sumer and Fredsøe, 1997)

The Strouhal number represents local acceleration of inertia forces due to changes in velocity from one point in the fluid flow to another. When the Strouhal number is within the range between 0.1 to 0.3 it is dependent on the Reynolds number. For the most part Strouhal number increases with increasing Reynolds number. However for a large range of Reynolds numbers, the Strouhal number remains in the range between 0.18 and 0.22, which is a common range of Strouhal numbers in many flow situations, especially subcritical flow. This can be observed in Figure 2.9 reprinted from (Sumer and Fredsøe, 1997).

The result of the oscillating vortex shedding from a body in incident flow is forces in flow direction and normal to the flow direction. These forces are called drag and lift forces. The forces appear as a result of the unsteady nature of the vortex shedding which causes oscillations in the pressure distribution surrounding the body. These forces are dependent on parameters like fluid density ρ, upstream velocity U and the shape, size and orientation of the body. It is common to use a dimensionless coefficients to describe the parameters connected to both lift and drag.
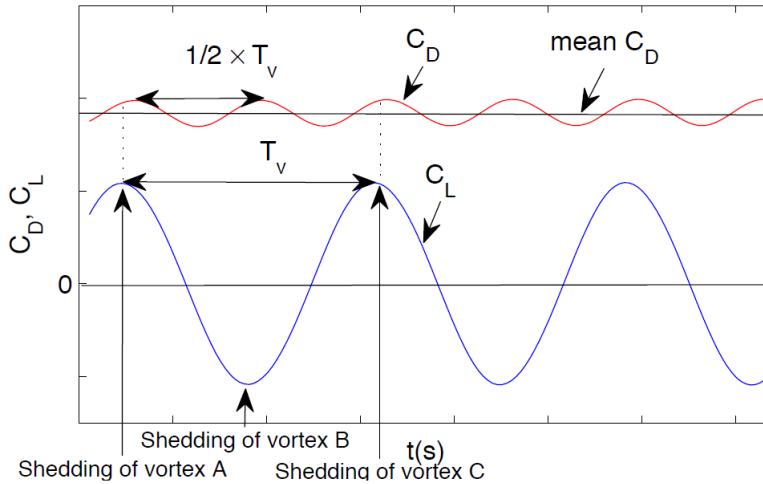
Drag coefficient:

$$C_D = \frac{F_x}{\frac{1}{2}\rho U^2 A_{ref}} \tag{2.12}$$

Lift coefficient:

$$C_L = \frac{F_y}{\frac{1}{2}\rho U^2 A_{ref}} \tag{2.13}$$

In Equation 2.12 and 2.13 the F_x and F_y represent the mean drag and lift force. A_{ref} describes the reference area, which for a three dimensional straight cylinder is equal to the cylinder diameter multiplied by the spanwise length of the cylinder. $1/2\rho U^2$ is the dynamic pressure. Both drag and lift forces are dependent on the Reynolds number, especially in the transition region between laminar and turbulent flow.


Figure 2.10: Oscillation of lift and drag coefficients as function of time (vortex shedding period noted T_V)

Lift and drag forces in steady incident flow both oscillate due to the alternating shedding of vortices. Figure 2.10 shows how the lift and drag coefficients oscillate. The lift coefficient oscillates about zero, and the drag coefficient about a higher value due to the contribution of frictional drag. The reason why the drag oscillation frequency is $2f_v$ is that a vortex is shed from the cylinder with period $T_V/2$. The lift force direction is dependent on what side of the cylinder the vortex is shed. The very important phenomenon called ***vortex induced vibrations*** appears as a result of the oscillating forces.

As mentioned in the introduction, vortex induced vibrations are a part of the underlying motivation behind the thesis as VIV is an important source of fatigue damage of offshore oil exploration and production risers. In worst case the structures can experience large excitation motions (resonance) occurring as a result of the vortex shedding frequency locking into the natural frequency of the oscillating object. In this thesis it is assumed that the body is rigid, thus the effects of an oscillating body are not taken into account. This assumption is made in order to reduce the complexity of the simulation model. Instead of trying to capture the direct relationship between response of a structure and the governing and influencing parameters, it is more rewarding to analyse what is the actual dominant response frequency of the body. Most studies and large scale experiments conducted today concern the interaction of rigid bodies (cylinders) with three-dimensional separated flows with large scale vortex structures.

For the case of cylinders and other bluff bodies there is a large scatter of both lift and drag coefficients. The coefficients are mostly determined through experiments, and many different experiments have resulted in different coefficients.
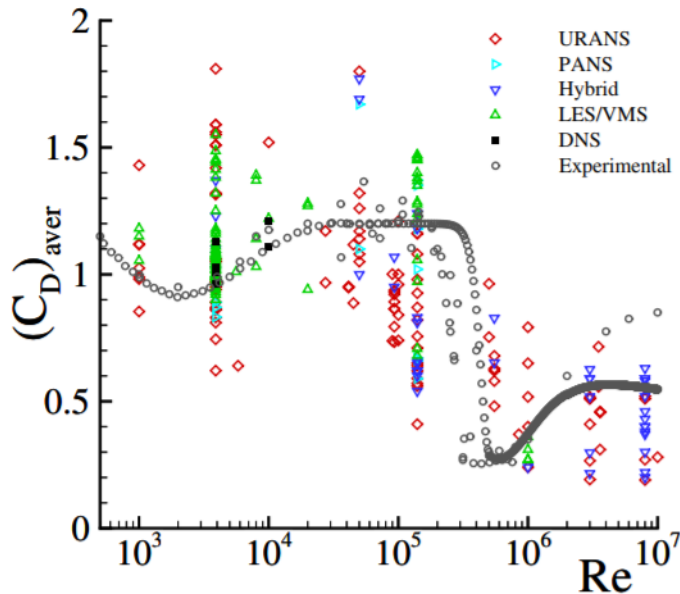
Figure 2.11: Values of average drag coefficient $(C_D)_avg$ of circular cylinder as function of Re from open literature (CFD predictions and experimental values), (Eca et al., 2014)

Figure 2.11 show numerical and experimental values of the mean drag coefficients of different Reynolds numbers. The data is collected from different sources all experimenting with flow over a circular cylinder. The figure shows how scattered the results are, and describes the difficulty of predicting the "correct solution". The different data points in the figure that are based on numerical studies, i.e. not experimental are performed with implementation of different turbulence modelling techniques (URANS, PANS, LES, DNS etc.). As can be observed from the figure, using different models have a great impact on the results, and thus it is very important to understand the difference between them. The topic of turbulence models will be visited later in this thesis.

Chapter 3

Literature Review

3.1 Introduction

The previous chapter gave a brief introduction to the world of fluid dynamics, and presented the necessary background theory. In this chapter a more specific literature review will be presented, to give a good foundation of the main topics of this thesis. The goal of the thesis is to obtain a better understanding of the physics of flow around different cylindrical configurations, where the final objective is to investigate and analyse a dual step cylinder. As mentioned earlier the dual step cylinder is a geometrical simplification that represents a small segment that comprises a part of the larger global system of an offshore oil riser.

Single and dual step cylinders are compound systems, meaning they can be seen as a combination of different geometric structures, and that the physics of their flow show great resemblance to other geometric configurations. A single step cylinder can for example be decomposed into three different geometries: straight cylinder, single cylinder attached to a flat plate, and a free end cylinder, which can be seen in Figure 3.1.
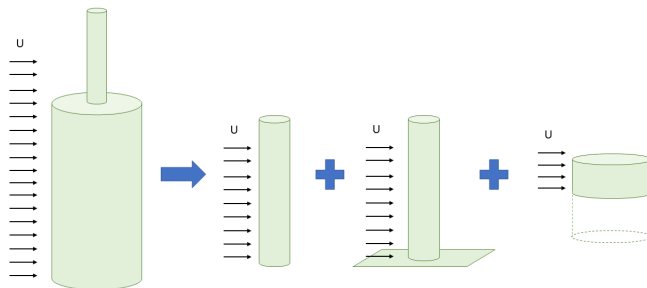
Figure 3.1: Step cylinder decomposed into straight cylinder, cylinder on flat plate and a step geometry

Each of these geometries have their own distinctive flow characteristics, which again will influence the wake in different ways. The wake behind a step cylinder can to some extent be considered as a summation of these flow cases. The next sections will cover the major findings from literature concerning the different geometrical configurations.

3.2 Flow around straight cylinders

The previous chapter has described what happens when a circular cylinder is placed in a steady incident flow. The effects of change in Reynolds number have been discussed, in addition to different flow characteristics and phenomena. The flow theory has been presented more or less from a 2D point of view. However, when we move into regimes of higher Reynolds numbers, the flow characteristics in the wake are present in three dimensions.

One of the more recent and comprehensive reviews of flow development over finite length circular cylinders is given by (Williamson, 1996). The paper presents an overview of the different vortex shedding regimes, and describes the transition from 2D laminar flow, via 3D laminar flow to 3D turbulent flow. The following list gives a brief explanation of the wake flow regimes considering different Reynolds numbers:

- $Re_D \approx 50$ $\longrightarrow$ Laminar Steady Regime

- $50 < Re_D < 190$ $\longrightarrow$ Laminar 2D Vortex Shedding

- $Re_D > 190$ $\longrightarrow$ Wake vortices gradually cease to be 2D

- $190 < Re_D < 260$ $\longrightarrow$ Vortex Dislocations developing

- $Re_D > 260$ $\longrightarrow$ 3D structures forming

- $1000 < Re_D < 2x10^5$ $\longrightarrow$ Turbulent transition in shear layer (separated boundary layer)

Because this thesis will undertake simulations with low Reynolds numbers (in the transitional region of Re 100-300), most of the literature review will focus on studies performed for laminar and transitional wake regimes.

In the regime of 3D structures the wake is highly dominated by vortices, and the flow is unpredictable and unsteady. Earlier studies have shown that a three dimensional wake is, in addition to the Reynolds number, highly dependent on the aspect ratio L/D. L is the length of the cylinder, and D is the diameter. The free end of the cylinder has also proven to be an important factor for three dimensionality. The free end has a big influence on the near wake, and the vortex formation region. An experiment in a wind tunnel performed by (Okamoto and Sunabashiri, 1992) show that the wake behind a cylinder of small aspect ratios ($L/D = 1 - 2$) is symmetric, but that the pattern of the wake becomes three dimensional when the aspect ratio is larger than $L/D = 4$.

Earlier studies performed by (Williamson, 1988) describes in more detail the transition from laminar and two dimensional flow wake, to the region where three dimensional vortex formations are observed. Up to that point, several studies, including (Tritton, 1959), had documented the presence of different shedding modes of different frequencies, and it had been debated what was the triggering cause of these effects. In his experimental research (Williamson, 1988) found that the different shedding modes and the discontinuity in shedding frequencies could be explained by the oblique shedding which to a large extent was caused by the cylinder end conditions. By attaching slanted end plates to the cylinder ends he was able to achieve parallel shedding along the whole span of the cylinder, with no sudden discontinuities. Thus demonstrating that parallel shedding is the intrinsic shedding mode in the periodic-laminar region of Reynolds numbers up to 180.

In another study to find the origins and development of transition in the wake (Gerrard, 1978) observed the formation of secondary vortices in streamwise direction. In his experiments Gerrad used green dye to visualize the structure of the wake behind the cylinder. His findings included the observations of these streamwise vortices, and described them as "fingers of dye", as they stretched between the vertically shed vortices. The fingers were visible along the whole span for all Reynolds numbers in the region between 140 and 500, and endured for 2-3 cycles downstream. Figures 3.2a and 3.2b show a visual representation of the vortex formation in the wake of cylinders at different Reynolds numbers. The visualization is from a later conducted experiment by (Williamson, 1996), and clearly show the streamwise vortices first described by Gerrard.

(a) Mode A, Re = 200, spanwise wavelength of 4D   (b) Mode B, Re = 270, spanwise wavelength of 1D
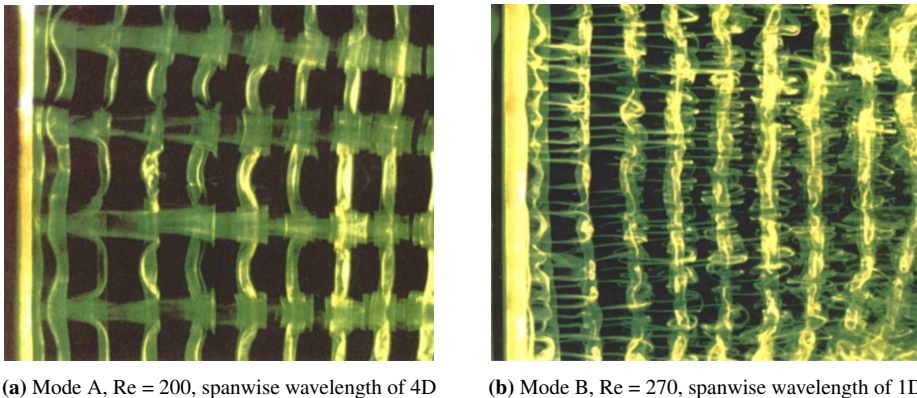
Figure 3.2: Experimental visualization of mode A and B (Williamson, 1996)

In his experimental studies, (Williamson, 1996) described discontinuities in the shedding patterns in the transitional range $180 < Re < 250$, which gave rise to the definition of two distinctive shedding modes, Mode A and Mode B. The prominent difference between the two modes is the spanwise wavelength of the streamwise vortices. As illustrated in Figure 3.2a and 3.2b Mode A has wavelengths in the range 3-4D, while Mode B has considerably smaller wavelengths closer to 1D. Mode A is reported to appear as a result of instabilities in the primary vortex core which deforms the vortex and pulls a part of it towards the body, forming vortex loops. Mode B on the other hand are thought to appear

as a result of instabilities in the smaller scale structures of the flow, resulting in the smaller wavelengths.

3.3 Flow around cylinder on flat plate with free end

A cylinder attached to a flat plate is another geometrical configuration that can describe a part of the combined problem of step cylinders. When the flow moves along the step on the top of the large cylinder towards the smaller cylinder, a boundary layer gradually builds up along the surface. This means that the flow that hits the free standing cylinder have a varying velocity gradient. This effect is illustrated with an example of flow along a flat plate, as shown in Figure 3.3
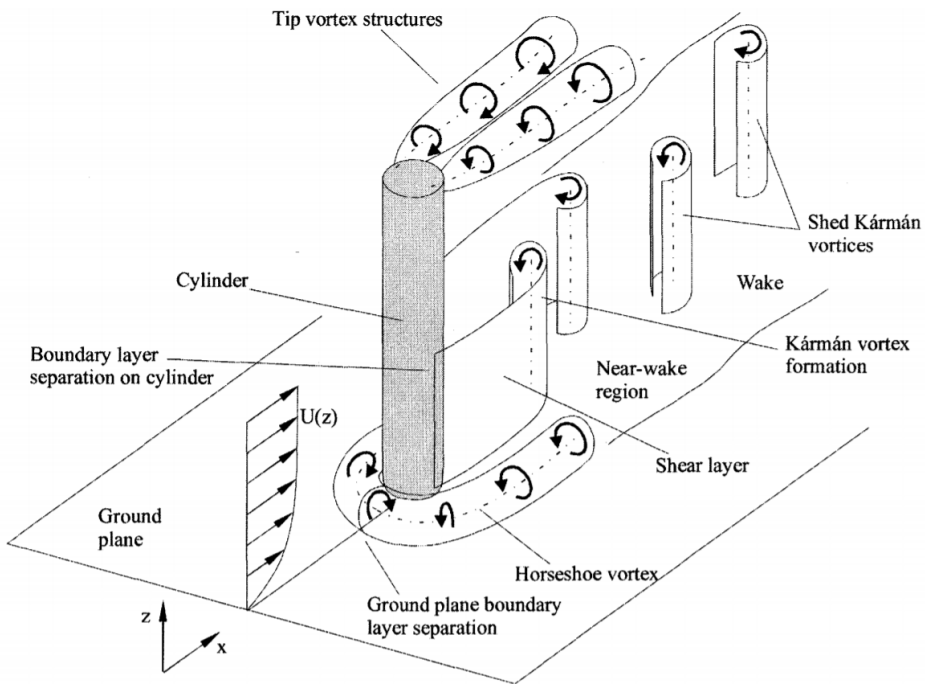
Figure 3.3: Wake structure of a circular cylinder with a free end on a flat plate, (Heseltine, 2003)

The boundary layer separates as it approaches the free standing cylinder, an recirculates at the leading edge of the cylinder (the junction). The fluid is swept around the cylinder base, rotating and rolling up in so called horseshoe vortices. If the cylinder is long enough, the region above where the streamwise vortex form, will separate in a manner similar to a straight cylinder. The formation of the horseshoe vortices gives the wake its distinctive characteristics with vortices rotating about different axis, crating a more chaotic and disturbed wake. Figure 3.3 shows the horseshoe vortices forming in the junction between the plate and the cylinder.

After the boundary layer flow washes along the surface of the step, it reaches the end of the cylinder top. The flow pattern caused by this area may partially be described by a free end cylinder, however the flow structure in vicinity of the free end is not very well understood, and there are different theories on what effect the free end actually has on the wake. One of the theories proposes the formation of counter-rotating trailing vortices being shed from the cylinder tip, Figure 3.3. The formation of these vortices is described to begin upstream as the flow inclines slightly to flow over the free end, a phenomenon called upwashing. When the flow then passes over the end of the trailing edge of the cylinder top it is directed down into the low pressure region in the wake of the cylinder. This phenomenon is called downwashing.

A study was performed by (Park and Lee, 2000). They tested different aspect ratios for the finite circular cylinder, $L/D = 6, 10, 13$, for Re of 20 000. The research showed how the flow interacted with the free end of the cylinder. They observed that two streamwise and counter rotating vortices formed and separated from the top of the cylinder. It was also observed that these vortices expanded in size and shifted downwards in spanwise direction, thus illustrating the effect of downwashing. Through the experiments performed it is evident that the downwash and the trailing tip vortices have a significant impact on the vortex shedding in the wake, and that the aspect ratio is an important factor.

3.4 Flow around stepped cylinder

When we move from a single finite cylinder to a step cylinder additional phenomena appear in the wake. The flow is now dependent new parameters, namely the diameter ratio d/D and the length aspect ratio between the small and large cylinder L/D. A simple sketch of a step cylinder is made in Figure 3.4. Different from the single circular cylinder, a more limited number of studies and experiments have been completed on the topics concerning more complex geometric shapes like the step cylinder. However, the step cylinder is a very common geometry in many engineering applications, and it is therefore important to investigate its characteristics.
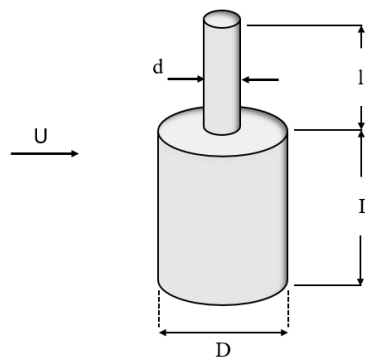

Figure 3.4: Geometry parameters for step cylinder

There has been performed experimental studies on the topic of stepped cylinders. Three different studies have looked at step cylinders with diameter ratios $0.36 \leq d/D \leq 0.87$ (Dunn and Tavoularis (2006), Lewis and Gharib (1992), Chua et al. (1998)). The results from the experiments have been sketched by (Dunn and Tavoularis, 2006). Figure 3.6 shows a schematic of the flow development over a step cylinder. The flow characteristics of the stepped cylinder is mainly dominated by the two separate vortex shedding frequencies from the large and the smaller cylinder, namely f_{vD} and f_{vd}.

The studies show that the vortices away from the step, in the rear wake, can be expected to follow the same pattern as the wake for uniform circular cylinders. Close to the step however, there is observed a significant area of disturbance between the vortices shed from the large and the small cylinder. Through the experimental results (Lewis and Gharib, 1992) there is observed two distinct types of wake behavior. The two modes are identified as **direct** and **indirect** modes of interaction. The two modes appear as a result of change in both Reynolds number and cylinder diameter ratio d/D (r). The interaction regions are categorized as the following:

- $r > 0.8$ $\longrightarrow$ **direct** mode dominates

- $0.64 < r < 0.8$ $\longrightarrow$ transitional (mode as function of Re)

- $0.64 > r$ $\longrightarrow$ **indirect** mode dominates

(a) Direct mode - Re=76, d/D=0.75

(b) Indirect mode - Re=99, d/D=0.57
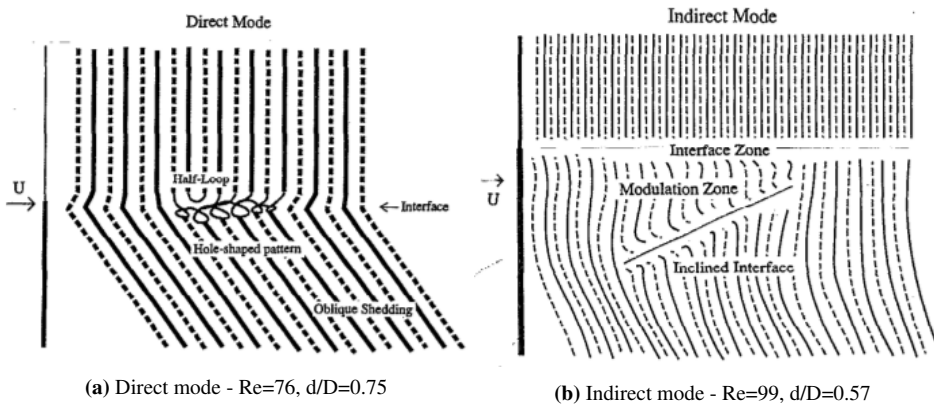
**Figure 3.5:** Direct and indirect mode vortex lines and linkage (Lewis and Gharib, 1992)

The direct mode is described as a direct interaction between the two vortex shedding frequencies, f_{vD} and f_{vd}. The vortex lines are found to be interrupted along a plane, which is called the *interface*. Figure 3.5a shows a sketch of a typical visualization of a direct mode. The vortices that are in phase (from small and large cylinder) connect across the interface. As the vortices become more out of phase, they link to each other on the same side of the interface. The result of this is "holes" in the wake, where there are no vortex tubes. This is a typical characteristic of the direct mode. Some of the vortices from

the smaller cylinder connect to the vortex that follows it, and forms a half-loop. This effect can be explained by the higher shedding frequency of the smaller cylinder.

The indirect mode is detected for diameter ratios smaller than 0.64. It is a more complex mode as an additional frequency, f_N, appears near the interface in the large diameter wake. The region where this effect occurs is called the modulated zone. The modulated zone shown in Figure 3.5b acts as a buffer between the two wakes from the small and large cylinder. This means that the two frequencies f_{vD} and f_{vd} do not interact directly. The new modulating frequency f_N is found to always be lower than the two cylinder frequencies. The vortex linkages occur in the modulation zone along the inclined interface (Lewis and Gharib, 1992).

Another important experimental review continued the work of describing the vortex behavior behind a stepped cylinder (Dunn and Tavoularis, 2006). In the studies they introduce specific terminology describing the observed vortex shedding patterns. They categorize the vortices generated in the wake of the step cylinder into two groups; *spanwise* and *streamwise* vortices.
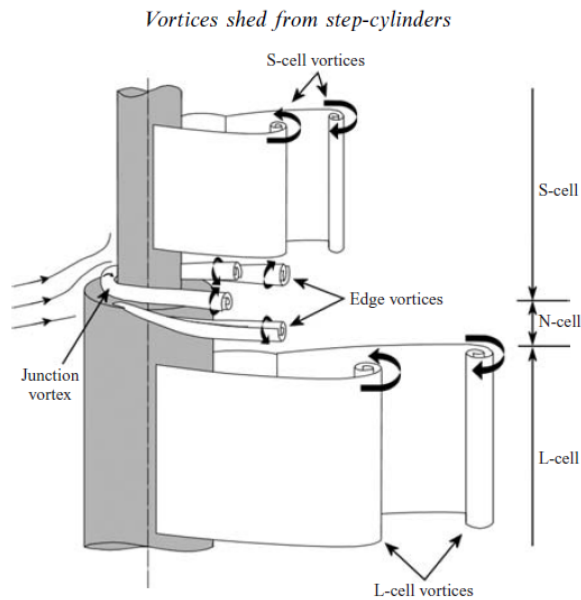
Figure 3.6: Sketch of different types of vortices near step cylinder with d/D = 0.5 (Dunn and Tavoularis, 2006)

3.4.1 Spanwise vortex shedding cells

The spanwise vortices can be seen in Figure 3.6. The vortices in the wake of the step cylinder are split into three separate regions based on the vortex shedding frequency. The vortex frequency in the wake of the small cylinder f_{vd} is dominant for the region called S-cell. The frequency f_{vD} for the larger cylinder is dominant for the region called L-cell. The last cell region is called N-cell. This region is dominated by the newly detected additional frequency f_N. It is is observed to appear only behind the larger cylinder close to the step.

Based on the local spanwise Reynolds number, the shedding of the vortices in the S-cell and L-cell show a similar pattern to that of a regular straight circular cylinder (Dunn and Tavoularis (2006), Lewis and Gharib (1992), Morton and Yarusevych (2009)). Away from the step, behind the smaller cylinder there is observed more or less undisturbed two-dimensional vortex shedding for lower Reynolds numbers. This is shown in the visualization in Figure 3.7 from the experiments performed by (Dunn and Tavoularis, 2006).
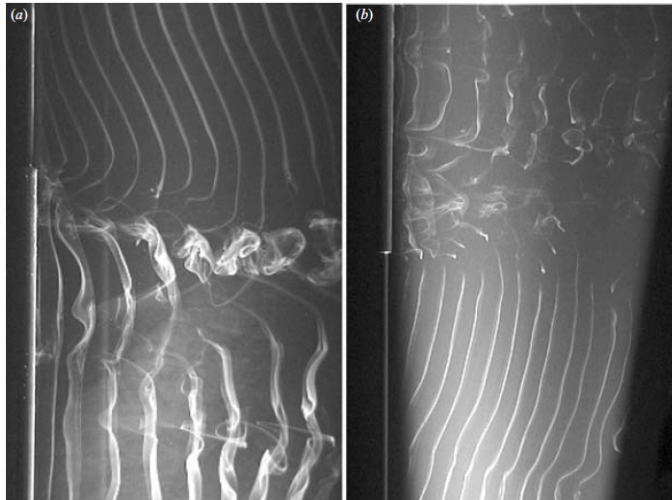
Figure 3.7: Vortex shedding patterns from step cylinder, (a) standard orientation $Re_D = 152$, (b) inverted orientation $Re_D = 168$ (Dunn and Tavoularis, 2006)

The wake behind the larger cylinder can be observed to be more influenced by the step than the smaller cylinder. Experimental studies performed by (Norberg, 1992) show that for different d/D and lengths l/L the larger cylinder is more affected by the step. The interaction region, later named N-cell region, is observed to have a great influence on the wake behind the larger cylinder. This means that there is not detected regular vortex shedding for the larger cylinder until approximately 3-4D in spanwise direction. In some cases the interaction region, N-cell region, was detected as far as 10D into the larger diameter side. The same conclusion is made in papers and experiments (Dunn and Tavoularis (2006), Lewis and Gharib (1992), Morton and Yarusevych (2009)).

Figure 3.7 also shows how the vortices shed from the smaller cylinder extends into the N-cell region. The vortices are found to extend about 1D into the wake of the larger cylinder. This is observed for a diameter ratio d/D of 0.5. (Dunn and Tavoularis, 2006) explain that the extension of the small cylinder vortices occur due to a lower pressure base behind the the larger cylinder. The vortices are therefore drawn into the wake of the larger cylinder.

An important part of the understanding of the flow over a step cylinder is what happens in the vicinity of the step (diameter change). As mentioned before the step is found to initiate an additional shedding frequency f_N which is dominant in the intersection region called N-cell. This flow characteristic is detected for step cylinders with diameter ratios $d/D < 0.6$. The shedding frequency in this region is found to be lower than that of the small and the large cylinder, fv_d and fv_D. Both (Lewis and Gharib, 1992) and (Morton and Yarusevych, 2009) describe how the expansion of the N-cell region varies in cycles. By performing experiments, and CFD-analysis they observe the characteristics of the N-cell region. They both describe how the region gradually grows and disappears, before starting a new cycle. There are some contradictions to whether the region disappears completely, or if it just grows so small that it is hard to detect. However the papers agree on the fact that the spanwise region between the large and the small cylinder identifies a cyclic behavior. The papers also describe how the N-cell extends more into the wake of the larger cylinder, thus influencing the flow characteristics behind it. The case has been tested for Reynolds numbers ranging with a factor of 20, and with several different diameter ratios, and a similar behavior for the N-cell region was detected in all cases.

3.4.2 Streamwise junction and edge vortices

Previous experimental investigations show visualizations of how the flow interacts with the step. (Dunn and Tavoularis, 2006) describe what the call *junction* and *edge* vortices. These vortices are streamwise vortices forming when the fluid moves past she step of the cylinder, much like the cylinder attached to a flat plate like mentioned earlier. The process is in essence explained as follows: the streamlines tend to separate from the leading edge of the step forming a recirculation bubble at the root of the small cylinder. The recirculated fluid forms a junction vortex on each side of the small cylinder as the fluid wraps around the cylinder. The rotating nature of the vortices causes them to "spill" over the edges forming two so called edge vortices. Figure 3.8 shows how the edge and junction vortices form around the cylinder. Both the recirculation bubble and the resulting junction and edge vortices can be observed in Figure 3.9.
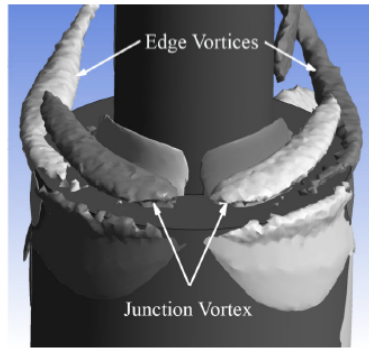
Figure 3.8: Edge and junction vortices around step. 3D vorticity visualization, (Morton and Yarusevych, 2009)

The images in Figure 3.9 show the results from two different research papers. Figures (a) and (c) are visualization of the streamlines, using computational fluid dynamics. Figures (b) and (d) show experimental visualization obtained by performing tests in a water channel. The comparison of the results suggests that the numerical simulations adequately reproduces the flow characteristics obtained in the experiment.
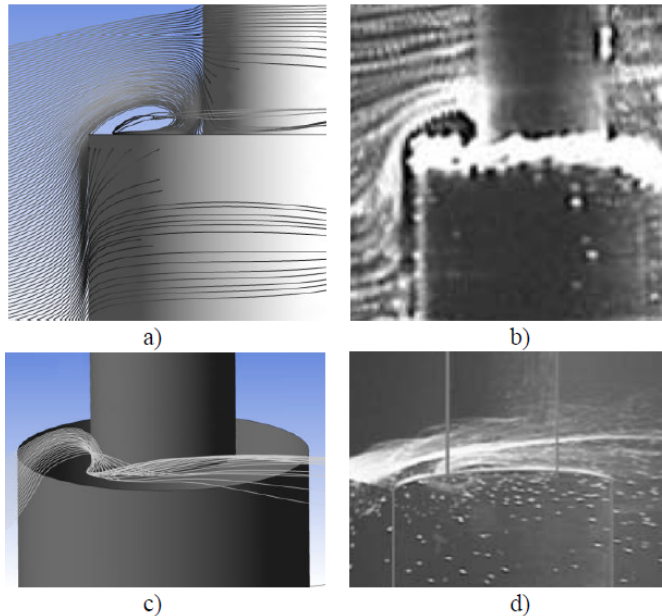
Figure 3.9: Development of junction vortex: (a) and (b) are computed streamlines around step (Morton and Yarusevych, 2009), (c) and (d) are experimental visualization from (Dunn and Tavoularis, 2006) d/D = 0.5 and Re = 1230

3.4.3 Vortex inclination and vortex dislocation

From the visual representation of the complex vortex shedding patterns it can as mentioned earlier be observed a strong inclination of the vortices in the S-cell region, with respect to the cylindrical axis. In addition to this, a similar inclination can be observed in the transition between N-cell and L-cell vortices. This inclination is not as strong. The inclination of the S-cell vortices is explained by (Dunn and Tavoularis, 2006). The inclination is thought to occur due to the varying separation points along the spanwise direction of the smaller cylinder. The inclinations have a great influence on how the vortices from the small and large cylinder connect and reattach.

Vortex dislocations occur as a result of the different vortex shedding frequencies, fv_d, fv_D and f_N. When the frequencies are out of phase, dislocations form between the vortices in the L- and S-cells, and the vortices in the N-cell. The phase difference results in the vortices forming connections to the following vortex in a looping manner, rather than connecting through the N-cell region.

3.5 Describing vortex pattern behind stepped cylinders

The nature of vortex formation in the wake of stepped cylinders is complex, and it is difficult to capture the characteristics both with experimental and numerical models. In more recent publications, (Tian et al., 2017a) and (Tian et al., 2017) have used Direct Numerical Simulation (DNS) to simulate flow around a step cylinder with diameter ratio $d/D = 2$ and $Re_D = 150$. They use snapshots of the wake structures at different time instances to give a detailed description of the vortex structure development and interaction. The simulation results are then compared with earlier findings to draw conclusions on whether there are direct similarities or if the results deviate. Different wake phenomena can be observed in the consecutive snapshots in Figure 3.10.

A numbering system is used in order to distinguish vortices shed from each side of the cylinder, e.g., 1,2,... indicate vortices shed from the "+Y" side, while 1',2',... indicate vortices shed from the "-Y" side. From previous studies it is known that the N-cell vortices are changing cyclical, and that they are characterized by vortex dislocations between N-cell, and L-cell vortices. During the vortex dislocation process two L-cell vortices disconnect with their adjoining N-cell vortices and form a L-L half loop. This event is visualized in snapshot (g) and (h) in Figure 3.10. The green line shows the detached half loop in the L-cell region. The detached vortex is a clear example of vortex dislocation.

In their study (Tian et al., 2017) they also observe additional features of the vortex structure. In the N-cell region two other types of loop-structures are identified. They classify the looped vortices as "real loops" and "fake loops". In the sequential snapshots in Figure 3.10 the real loops are highlighted with blue lines, while the fake loops are highlighted with solid and dotted red lines. The explanation behind the definition "fake loops" is that the loops have similar appearance as a vortex-ring structure, but the actual connection topology is different. When a L-cell vortex detach from a corresponding N-cell

vortex from the same side, the L-cell vortex cannot have a loose end and must therefore attach with a N-cell shed from the opposite side. This effect can be observed in figure 3.10 (c). The result of this connection is a fake loop structure.
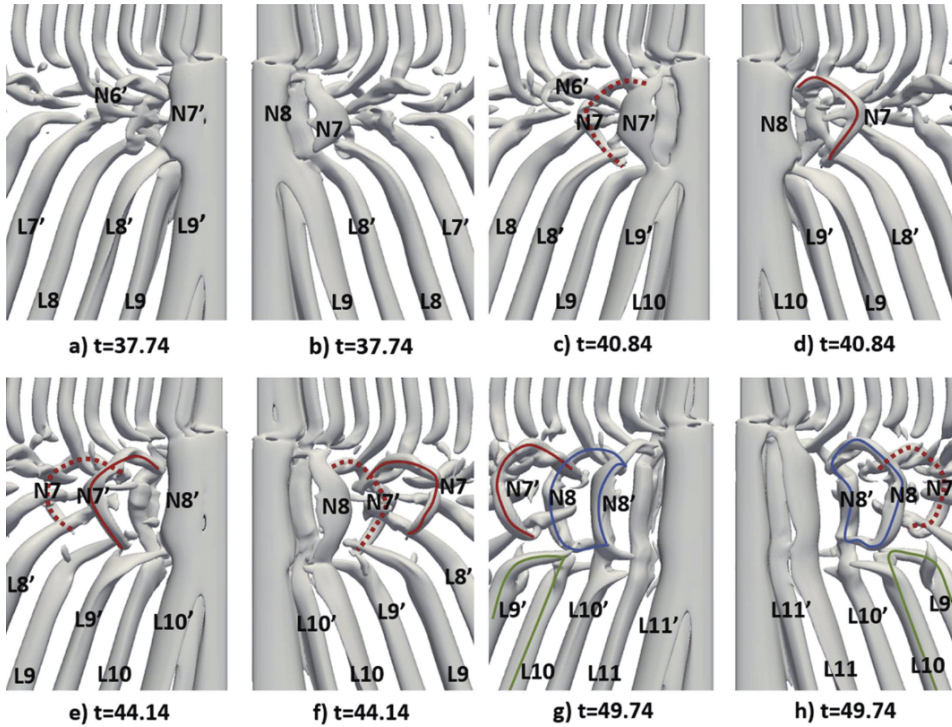
Figure 3.10: Vortex interactions at N-L cell boundary during the dislocation process, (a), (c), (e) and (g) are observed from "+Y" side while (b), (d), (f) and (h) from the opposite side. Solid and dashed red curves indicate "fake-loops", blue curves show real loops and green curves show half loops/dislocations. (Tian et al., 2017)

The real loops are formed in another manner, as a N-cell vortex is connecting directly with a N-cell vortex from the opposite side. This vortex structure is highlighted with blue lines in Figure 3.10 (g) and (h). Understanding the vortex shedding patterns and the structure in the wake has many advantages. Categorizing the different structures makes it possible to recognise similarities and to draw parallels from similar flow cases. By observing the structural composition of the vortices it is also possible to connect each feature with the actual forces and responses exerted on the body.

3.6 Flow around dual step cylinder

Where many studies have been conducted on the topic of single step cylinders, fewer have been performed for dual step cylinders. However, one of the more detailed reviews of flow over dual step cylinders includes (McClure et al., 2015). The paper presents the results

from numerical investigations performed at Reynolds numbers in the laminar/transitional regime ($Re_D = 150$), for a range of aspect ratios, $0.2 \leq L/D \leq 5$ and diameter ratios, $1.1 \leq D/d \leq 4$. Th most important findings reveal four distinct types of vortex topology in the wake of the large cylinder:

(i) shedding of hairpin vortices

(ii) transient asymmetric shedding

(iii) primarily spanwise shedding

(iv) no vortex shedding

(McClure et al., 2015) investigate how a change in diameter ratio will affect the wake topology. Figure 3.11 provide details of the vortex structure behind four dual step cylinders with different diameter ratios. As can be observed vortex shedding occurs behind the small and large cylinder for all cases except (a), where the Reynolds number for the small cylinder is below the critical value of primary shedding instability.
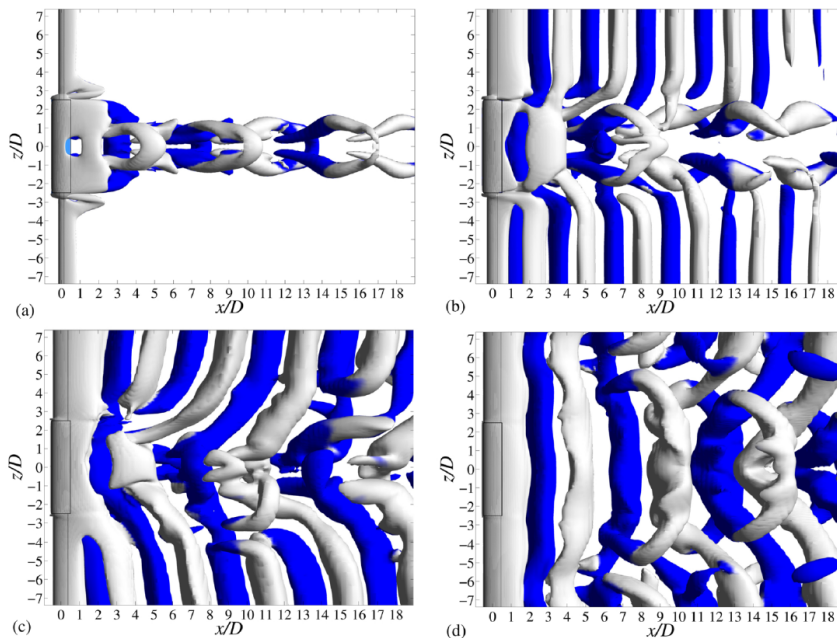
Figure 3.11: Instantaneous isosurface of $\lambda_2 = 0.01$ for L/D = 5 and $(a)D/d = 4$, $(b)D/d = 2$, $(c)D/d = 1.33$, $(d)D/d = 1.1$ (McClure et al., 2015)

For the larger D/d ratios you can clearly see the significant formation of streamwise vortices, described by the authors as "hairpin-like" vortices. The deformations in the wake are pronounced for the larger steps, and become more suppressed for the smaller ratios, until the vortices shed from the large cylinder are nearly parallel to the body. When there is a large difference in diameter between the small cylinder and the large cylinder, the

vortices are shed with different frequencies, which leads to a phase difference. This difference allows for vortices to split and form half-loop connections with adjacent vortices. (McClure et al., 2015) also note that shedding from the upper small cylinder is approximately $180 \deg$ out of phase with the shedding from the lower small cylinder for $D/d = 2$ and $D/d = 1.33$. This out of phase alignment leads to oblique shedding and asymmetric vortex interactions in the wake of the large cylinder.

In the same study they also investigate the effect of cylinder aspect ratio on wake topology for $D/d = 2$ and $0.2 \leq L/D \leq 5$. Figure 3.12 shows the vortex structures behind the dual step cylinder for different aspect ratios.
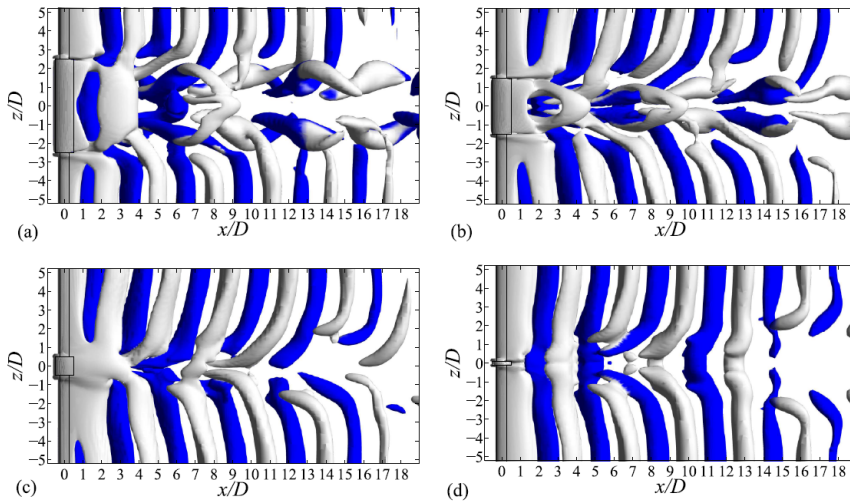
Figure 3.12: Instantaneous isosurface of $\lambda_2 = 0.01$ for D/d = 2 and $(a)L/D = 5$, $(b)L/D = 3$, $(c)L/D = 1$, $(d)L/D = 0.2$ (McClure et al., 2015)

The wake observed for $L/D = 5$ shows the hairpin-style vortices appearing downstream of the large cylinder, with half loop vortices forming in the small cylinder wake. For $L/D = 3$, a similar vortex structure is observed, but now the spanwise extent of the hairpins is gradually diminishing. For the cylinders with the lowest aspect ratio the streamwise vortices cease to exist, and the cylindrical vortices connect across the wake. It can also be observed that when the relative alignment of the small cylinder vortices changes, the direct connections are replaced by half loops between two subsequent vortices shed from the small cylinders.

3.7 Short summary of earlier studies

The studies conducted on the topic of flow over circular step cylinders include both experimental and numerical solutions. The use of Computational Fluid Dynamics, hereafter referred to as CFD, has increased rapidly the last few decades. Numerical simulation allows for the opportunity to make predictions and visualizations of the flow characteristics. The articles presented in the theory part of the step cylinder are partly experimental, and partly numerical. By combining the two research methods you increase the accuracy of the studies. The numerical studies performed by (Morton and Yarusevych, 2010) and (Valles and Andersson, 2002) are reproductions of experimental cases. This way the numerical results can be directly compared to a set of experimental data, which can be used as both a validation and a verification of the research process.

In the papers (Morton and Yarusevych, 2009) and (Morton and Yarusevych, 2010) they perform numerical simulation based on DES (Detached Eddy Simulation, LES (Large Eddy Simulation) and URANS (Unsteady Reynolds Averaged Navier Stokes) numerical solvers. The theory behind these solvers will be presented in the next chapter. In their studies they recreate the experiment performed by (Dunn and Tavoularis, 2006) by using the same diameter ratios and the same Reynold numbers. Their results show many similarities to the experimental data.

The scientific papers concerning computational numerical simulations will form the basis behind this particular project thesis, as many of the findings in the papers draw the same conclusions. The next chapter will go through the important theory behind the numerical solvers used in fluid dynamics.

Chapter 4

Governing equations and numerical framework

Computational Fluid Dynamics (CFD) is a generic term used to describe the process of numerically solving partial differential equations (PDE) that describe fluid flows. In the world of viscous fluid dynamics, the governing equations are the Navier-Stokes equations (N-S), which describe the fluid motion. The computational process includes discretization of the equations within a computational domain, and the solving of these equations given a set of boundary conditions and initial flow conditions. By calculating the fluid motions in each discretized grid point within the boundary, it is possible to retrieve data and local properties like pressure p and velocity components u, v, w. These output values can again be used to calculate forces and make visualizations of the flow characteristics.

CFD has many different areas of application. These may include incompressible and compressible flows, laminar or turbulent flows, flows with free surface effects, flows with heat transfer etc. It is when it comes to the transition between laminar and turbulent flows that the real challenges of CFD appear. CFD can with great precision predict laminar flows, but when we move into the turbulent regime it is very difficult to analyse the flow without the use of turbulence approximations, or so-called ***turbulence models***. Because many engineering systems are subjected to turbulent flow, we rely on the accuracy of these turbulence models.

Direct Numerical Simulation (DNS) is considered the most accurate method, as the Navier-Stokes equations are solved directly, with no need for turbulence modelling or simplifications of the equations. However, the method is very time consuming and requires a large amount of computer power, especially when the Reynolds number increases and the flow becomes more turbulent. Other methods have been developed in order to simulate the higher levels of turbulent flow, and amongst the more common is the Reynolds Averaged Navier Stokes method (RANS). RANS is based on the theory of averaging the partial differential equations describing the fluid motion. This means that instead of resolving

all the eddies down to the absolute smallest scales in the turbulent flows, the Kolmogorov microscale, a mathematical turbulence model is applied to predict the effects of turbulence. Another method of predicting turbulent flows is the Large Eddy Simulation (LES) method. The principle idea behind the method is to resolve the larger eddy structures, while using some means of turbulence modelling on the smallest eddy structures. In the research papers and studies presented in the previous chapter many different methods have been utilized, ranging from DNS and LES to, RANS. It is therefore important to get a basic understanding on the main differences between them, on order to distinguish the results.

The following sections will go through the fundamental theory behind numerical solutions of the governing equations used in CFD. There will also be discussed the importance of, and the differences between turbulence models, and for which situations each model should be applied. The chapter will also include the basic principles of the process of using CFD as a tool.

4.1 Governing equations

The governing equations describing viscous fluid flow are the ***Navier-Stokes Equations*** and the ***Continuity Equation***. The N-S equations describe the motion of the fluid in terms of conservation of momentum, while the continuity equation represent the conservation of mass. In relevance to this thesis, and for the sake of simplicity, several assumptions can be made concerning the fluid properties. Since the fluid of interest in this case is sea water, it is reasonable to assume that the density ρ is constant in the whole domain, i.e. incompressible. Moreover, the dynamic viscosity μ and the kinematic viscosity ν can also be regarded constant through the whole domain, i.e. Newtonian. In addition to these assumptions, the fluid is considered to be isothermal, meaning variations in temperature throughout the fluid can be neglected. Thus there is no need for additional differential equations describing the conservation of energy.

With the underlying assumptions the equation of continuity can be expressed as:

$$\frac{\partial u}{\partial x} + \frac{\partial v}{\partial y} + \frac{\partial w}{\partial z} = 0 \tag{4.1}$$

The Navier-Stokes equations in three dimensions can be expressed as:

x-direction: $\quad \dfrac{\partial u}{\partial t} + u\dfrac{\partial u}{\partial x} + v\dfrac{\partial u}{\partial y} + w\dfrac{\partial u}{\partial z} = -\dfrac{1}{\rho}\dfrac{\partial p}{\partial x} + g_x + \nu\left(\dfrac{\partial^2 u}{\partial x^2} + \dfrac{\partial^2 u}{\partial y^2} + \dfrac{\partial^2 u}{\partial z^2}\right) \quad$ (4.2)

y-direction: $\quad \dfrac{\partial v}{\partial t} + u\dfrac{\partial v}{\partial x} + v\dfrac{\partial v}{\partial y} + w\dfrac{\partial v}{\partial z} = -\dfrac{1}{\rho}\dfrac{\partial p}{\partial y} + g_y + \nu\left(\dfrac{\partial^2 v}{\partial x^2} + \dfrac{\partial^2 v}{\partial y^2} + \dfrac{\partial^2 v}{\partial z^2}\right) \quad$ (4.3)

z-direction: $\quad \dfrac{\partial w}{\partial t} + u\dfrac{\partial w}{\partial x} + v\dfrac{\partial w}{\partial y} + w\dfrac{\partial w}{\partial z} = -\dfrac{1}{\rho}\dfrac{\partial p}{\partial z} + g_z + \nu\left(\dfrac{\partial^2 w}{\partial x^2} + \dfrac{\partial^2 w}{\partial y^2} + \dfrac{\partial^2 w}{\partial z^2}\right) \quad$ (4.4)

The foundation of the N-S equations is Newton's second law of motion, which describes the relationship between a body with exerted forces, and the motions in response to those forces. The first term in the equation is the unsteady term. The next three terms on the left side are acceleration terms. On the right side there are three different terms; the pressure term, the body force term and the viscous term. In many cases the body force (gravity) term is neglected.

Together the N-S equations makes a powerful tool when modeling viscous flows, but since they are non-linear differential equations they become increasingly difficult to solve numerically as the complexity of the flow increases. For that reason it is necessary to simplify the equations, and a possible way this can be done is through Reynolds averaging.

4.1.1 Reynolds Averaged Navier-Stokes Equations

Reynolds-Averaging is based on the principle of time averaging the equations of motion for fluid flows. The purpose of the method is to decompose the N-S equations into a time-averaged and a fluctuating quantity. This mathematical operation can be completed with the assumption that the instantaneous value of a parameter can be expressed by the sum of its mean and fluctuating value. The N-S equations can therefore be rewritten in the following manner (Chen et al., 1990):

$$\frac{\partial \widetilde{u}_i}{\partial t} + \widetilde{u}_j \frac{\partial \widetilde{u}_i}{\partial x_j} = -\frac{1}{\rho}\frac{\partial \widetilde{p}}{\partial x_i} + \nu \frac{\partial^2 \widetilde{u}_i}{\partial x_j \partial x_j} \tag{4.5}$$

The variable $\widetilde{u}_i$ represents the instantaneous value, which in this case is the instantaneous velocity. Thus the sum of this value can be expressed by the mean and fluctuating parts as shown below:

$$\widetilde{u}_i = U_i + u_i \tag{4.6}$$

The same time averaging principle is then performed for all the terms in the N-S equations. By applying Reynolds averaging rules such as; $\overline{U}_i = U_i$ and $\overline{u}_i = 0$ it is possible to simplify the equation. Further simplifications can be made as the mean velocity and the fluctuations conserve mass, indicating that $\frac{\partial U_i}{\partial x_i} = 0$ and $\frac{\partial u_i}{\partial x_i} = 0$. This yields the complete RANS-equation:

$$\frac{\partial U_i}{\partial t} + U_j \frac{\partial U_i}{\partial x_j} = \frac{1}{\rho}\frac{\partial}{\partial x_j}\left(-P\delta_{ij} + \mu\left(\frac{\partial U_i}{\partial x_j} + \frac{\partial U_j}{\partial x_i}\right) - \overline{\rho u_i u_j}\right) \tag{4.7}$$

In the RANS-equation the right side consists of three distinctive terms. The first term expresses the pressure stress, the second term expressed the viscous stress and the third term expresses the turbulent stress, or the so-called Reynolds stress. The turbulent stress term $\overline{\rho u_i u_j}$ is the most determining term as it generates turbulence in the fluid. One of the most challenging task when implementing turbulence modelling is to find good approximations for this term, as it is non-linear and has no analytical solution.

The most common types of turbulence models are the two-equation models. Among the most used in the engineering industry are; **k-epsilon model**, **k-omega model** and the **Menter SST k-omega model**. These two-equation models are based on the transported variable of turbulent kinetic energy k, the viscous dissipation, ϵ and the specific turbulent dissipation rate ω. The theory behind many of these models is extensive, and therefore no further elaboration is performed. However, the importance of choosing the appropriate turbulence model for the existing flow case is apparent. It is therefore important to know when to apply which model, as each one has its strengths and weaknesses. In general, for the mentioned turbulence models the following characteristics are known; the k-epsilon model is performing well for free stream flows and the k-omega model is most suitable for near wall interactions. Moreover, the SST model is created with the intent of using properties from both previously mentioned models. This makes it a robust model for flow situations of objects in free stream flow.

4.2 Solution procedure

The following list of steps is constructed based on (Cengel and Cimbala, 2010), and gives a good description of the procedure of solving the Navier-Stokes equations in CFD. This includes both pre- and post processing.

1. Choice of **computational domain** and construct a suitable **grid**. This is one of the most crucial parts of the process. The domain is divided into smaller cells. For 2D domains, these cells are areas, whereas for 3D domains the cells are small volumes. When the conservation equations are solved, they are solved within each of these cells. This means that the construction of the grid will have a profound influence on the solution. It is therefor important to make a high quality/purposeful grid before proceeding to the next step.

2. The **boundary conditions** have to be specified for each face of the domain. Boundary conditions are very important to ensure that the physical constraints are conserved.

3. Choose the fluid model used in the problem, and specify the fluid properties like density, viscosity, temperature, etc. Most CFD software have built-in databases for the most commonly used fluids.

4. Selection of the numerical parameters and solution algorithms. Examples may be the decision of choosing laminar or turbulent flow. If the flow is turbulent, the right/appropriate turbulence model must be applied.

5. Assigning suitable starting values for the flow field variables. This means specifying *initial conditions* for each cell. In other words this means setting a starting value in order for the iteration process to proceed. This is specially important for *unsteady* i.e. time dependent flow.

6. Initiating the calculations of the discretized forms of the conservation and transport equations. The process of numerically solving the equations involves an iteration process. For each iteration a *residual* value is retrieved for every cell. This residual value is an indicator on how much the solution from a transport equation deviates from the "exact solution", meaning if the sum of all terms in N-S is equal to zero for each cell in the domain. If the number of iterations is increased, the residual values will decrease. By monitoring the average of these values you can determine when the solution has converged, thus ending up with a final solution.

7. The next step is a part of the *post processing*. The converged solution is processed using visualization tools. Properties such as velocity and pressure are plotted and graphically analyzed. This part of the process is very important, as it gives the user a means of interpretation to determine if the solution is meaningful. When evaluating the data it is very important to know what to look for, and how you can process the data in a manner most suitable for the results you have obtained, or what you want to emphasize or highlight. The tools for the post processing is often included in CFD software.

8. Monitoring the quantities of the global properties along with residuals in order to determine if the solution actually has converged correctly and the values have stabilized.

4.3 Grid discretization and solver methods

Arguably the most important step in a CFD solution is the grid generation. The computational domain is discretized into smaller cells on which the different flow variables are calculated, such as local velocities and pressure. Usually a generation code is integrated in the software to discretize the domain. In the grid generation process it is common to distinguish between *structured grids* and *unstructured grids*.
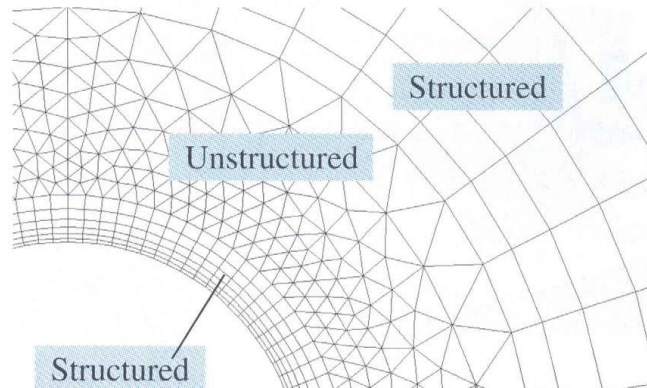
Figure 4.1: Structured quadrilateral and unstructured triangular grids, (Cengel and Cimbala, 2010)

Structured grids are consisting of planar cells with four edges (for 2D cases) or six faces (3D cases). Even though the cells in a structured grid have four corners, they do not necessarily need to be perfectly rectangular. However, their rectangular nature means that it is easier to number the cells according to indices, like (i, j and k) for 3D grids. The indexation makes it much easier for the solver to keep track of the calculation process. Unstructured grids on the other hand consist of shapes of more various nature, usually triangular or quadrilateral cells for 2D cases, and tetrahedron or hexahedron cells for 3D cases (Cengel and Cimbala, 2010). Contrary to structured grids, the unstructured grids cannot be indexed in the same manner, with uniquely identified cells. This means that the grid generation code uses other numbering techniques to order the grid cells. In general, unstructured grids are easier for the grid generation codes to create, especially around more complex geometries. However, structured grids are preferred in computational dynamics, as they have proven to be more efficient and converge more rapidly (Cengel and Cimbala, 2010).

After the computational domain has been discretized, the solver is ready to numerically compute the differential equations for each cell. The actual solver is the backbone of a CFD software. There are a number of different numerical discretization techniques available in the solving of fluid problems, such as the *Finite-difference method* (FDM), the *Finite Element Method* (FEM) and the *Finite Volume Method* (FVM), where the last mentioned method is among the most commonly used. The method does not require a transformation of coordinate system, and can therefore be applied directly to an unstructured grid. This is a great advantage as it reduces the memory usage and increases the solution speed. FVM involves in short an integration of the governing equations (Navier-Stokes, conservation and turbulence equations) over the computational domain. The equations are then recast in a conservative form through approximations, and solved over discrete control volumes (Versteeg and Malalasekera, 2007).

Before time integration is possible an additional discretization method must be applied in order to find good approximate solutions to the differential equations. An example of such a method is the Runge-Kutta scheme (Moukalled et al., 2016). Because transient

(unsteady) are time dependent, there is naturally a strong connection between the size of the computational time steps and the size of the discretized cells. To ensure that the solution converges, it is necessary to apply a small enough time step, while always keeping in mind the connection between time step and cell size. This subject, including the use of sensitivity analysis will be discussed more in the next chapter.

4.4   Boundary conditions

For the solver to complete the calculations of the flow inside the computational domain suitable boundary conditions have to be applied. At the boundaries of the domain certain physical conditions have to be prescribed to make sure solving the equations is possible. There are two commonly encountered boundary condition types; the ***Dirichlet*** and the ***Neumann*** conditions. A Dirichlet boundary condition specifies a value of a scalar that is fixed on the boundary, while the Neumann condition specifies the normal derivative (gradient) of a scalar fixed to the boundary. The type of boundary condition to apply is highly dependent on the geometry, flow properties and domains you wish to represent. The most relevant boundary conditions to this thesis are the following, taken from (Cengel and Cimbala, 2010):

Wall boundary:

The wall boundary is one of the more easy boundaries to represent, as the characteristic we want to highlight is the impermeability of the surface. This can simply be done by setting the normal component of velocity to zero relative to the wall along a surface on which the boundary condition is prescribed. Moreover, as mentioned in Chapter 2, a body at rest in a viscous flow will experience zero velocity close to the surface (boundary layer). This is referred to as the no-slip condition, and can mathematically be expressed as a boundary condition, meaning $u = v = w = 0$ at the wall (Dirichlet).
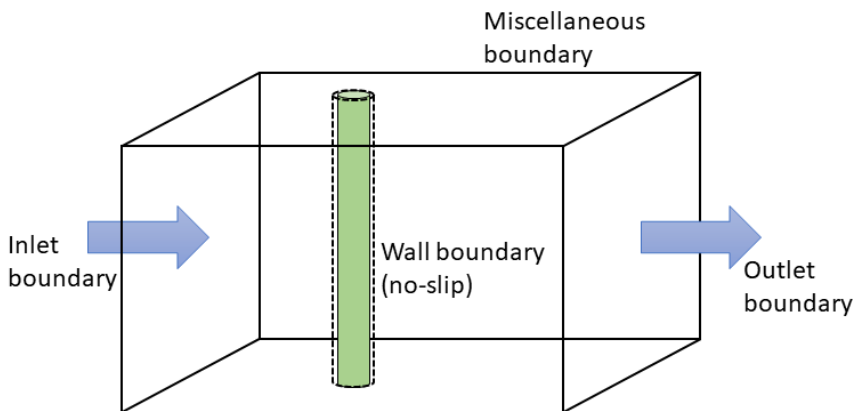
Figure 4.2: Boundary conditions for 3D computational domain, flow around cylinder

Inlet/outlet boundary:

There are several ways to model the boundaries that surround the computational domain. For example for uniform flow around a body, we need to apply a boundary that allows fluid to enter the domain (inlet), and a boundary that allows fluid to leave the domain (outlet). These boundaries are generally defined as either velocity boundaries or pressure boundaries (Dirichlet), depending on what kind of case you are modelling. One important factor to consider when working with domain boundary conditions is the effect they have on the flow inside the domain. The forced velocities at the boundaries will have a direct influence on the fluid in close proximity. If the boundary limits are not adjusted properly, meaning sufficiently distant from the body, they will have direct influence on the solution.

Miscellaneus boundary:

Miscellaneus boundary conditions represent the boundaries of the computational domain that are not inlets/outlets, nor wall boundaries. Usually these boundaries can be split into two categories, *symmetric* and *periodic* conditions. Symmetric boundary conditions use the principle of mirroring the flow field across the whole boundary, which is normally achieved by setting the gradients normal to the boundary to zero. Periodic boundaries can be constructed by setting the variables at the boundary equal to the variables of the neighbouring face. Periodic boundaries are usually used for flow fields with repeating patterns (Cengel and Cimbala, 2010).

4.5 FINE/Marine

An essential part of this master thesis is to learn how to incorporate a CFD software to a fluid flow problem. the software that will be utilized in this thesis is FINE/Marine 8.2 developed by NUMECA. FINE/Marine has specialized their numerical solvers for the use in marine applications, and it is performing well in free-surface/multi-fluid modelling such as hull design. However, the good computational foundation makes the solvers applicable for other flow problems such as mono-fluid flows and subsea applications. The software is built up of three main components/stages. HEXPRESS lets you create the desired geometry in a Computer Aided Design (CAD) extension. In HEXPRESS you also crate the computational domain, and initiate the grid discretization process. The geometry, with applied mesh is then uploaded in the actual FINE/Marine interface, where the computational parameters can be selected, such as; flow parameters, boundary conditions, and simulation setup. The backbone of the CFD software is the actual solver. FINE/Marine is based on the ISIS-CFD flow solver, developed at the University of Nantes. The solver uses the incompressible unsteady Reynolds-Averaged Navier-Stokes equations, and the Finite Volume Method (NUMECA, 2020). The third important part of the CFD software is the post-processing and visualization tool, CFView. The analysis tool lets you display data as vector plots, contour plots, streamlines and other means of visualization. CFView also provides a monitor, where it is possible to track calculated values during the computational process, such as residuals and forces.

4.6 Vortex detection

An important part of the visualization process, and the investigations of the wake structures involves the detection of vortices. Different methods have been developed in order to numerically determine the location of the vortices, based on the known characteristics of vorticity and vortex formation. The most sophisticated identification methods are λ_2 and ***Q-criterion***, developed in the late 80s, both based on the detection of vortex cores.

As mentioned in the theory chapter, vortices are often shed from blunt bodies in fluid flow. These vortices are characterized by fluid particles rotating in the same direction around a vortex core. The center of the core experiences the highest particle velocities, with decreasing speeds in the outer part of the vortex. This indicates that a low pressure region is formed in the center of the vortex.

The Q-criterion is based on the detection of vortical motions by monitoring of the velocity gradient tensor, Δu, defined by the second invariant Q (Kolár, 2007). The actual implementation of the Q-criterion involves setting a value for the second invariant, and thus visualize the vortex structures of that specific value. A lower, positive Q-value tends to be more sensitive in the detection than larger values. A disadvantage of the Q-criterion method involves the sensitivity, and that the detection may include shear layers close to the surface of the body due to high vorticity. This may give the visualization some additional structures besides the actual vortices in the wake.

The λ_2-criterion is based on the detection of the low pressure regions in the core of the vortices. Similarly to the Q-criterion a value has to be defined in order to detect vortices in that area. The eigenvalue λ_2 is by definition lower than zero, and similarly to the Q-criterion values closer to zero indicate more sensitivity, and thus more detected vortex structures (Kolár, 2007).

Both methods will be used in this thesis, as important tools for visualization.

Chapter 5

Validation case

Besides the theoretical studies in the first chapters in this thesis, an equally important part is to learn how to use computational fluid dynamics to solve fluid flow problems. It is evident that in the field of CFD, experience, knowledge and training are key attributes. The numerical solution of a fluid flow is a highly iterative process, and therefore it may take countless attempts of trial and error in order to obtain good results. The beat way to learn how to use CFD is to dive into a software, and learn along the way as you try to solve a fluid problem.

In this context, the next sections will describe the main steps of the process of solving a fluid flow problem connected to the topic of circular cylinders. The goal of the case is to perform calculations of viscous flow around a two-dimensional circular cylinder at $Re = 100$. The case will work as an introduction to the CFD software of FINE/Marine, and all the important elements that are needed to build up a good computational model. These include definition of geometry and domain in HEXPRESS, grid generation, boundary conditions, computational solver setup and post-processing in CFView. The most important part of this case study is to observe how variations in domain size, grid refinement and time steps will affect the solution, and also the computational time. The results obtained from the "optimized" solution will be compared with values and results from similar academic papers and literature. This way the case can be used as a validation of the CFD process, which enables for further development of the existing case.

In the simulations a constant Reynolds number of $Re = 100$ will be used. This indicates that the flow is laminar, with laminar separation. To achieve this Reynolds value both inlet velocity U and cylinder cross-section diameter D are set to unity (1 m/s and 1m respectively). The kinematic viscosity is set to 0.01 in order to get the desired Reynolds value. FINE/Marine uses dynamic viscosity as input parameter, which in this case is equal to $\mu = 10$, due to a choice of density $\rho = 1000[\frac{kg}{m^3}]$.
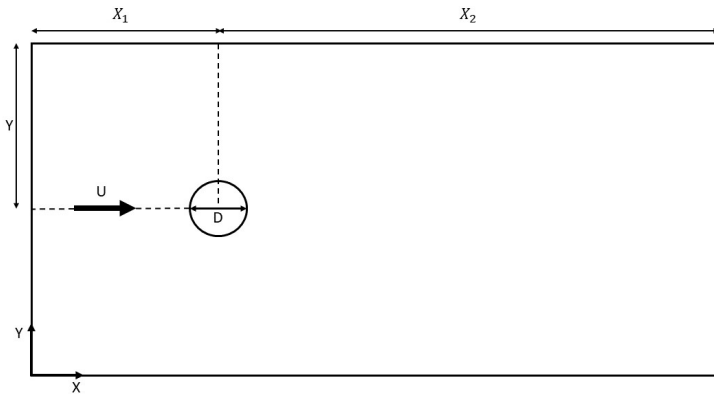
Figure 5.1: Two-dimensional circular cylinder with general computational domain

Figure 5.1 shows a generalized description of the geometry that will be implemented in FINE/Marine. For the computational domain, the three parameters Y, X_1, and X_2 are defining, and will be subjected to change to observe how their values affect the solution.

5.1 Geometry definition and grid generation process

The definition of geometry is performed in the CAD manipulator extension in HEX-PRESS. The approach when defining the geometry is in essence to define the computational domain. This can be done by creating a cylinder (at specified coordinate points), and a box surrounding the cylinder (of desired size). The cylinder body is then subtracted from the box, creating a domain. The generated domain and the HEXPRESS user interface is depicted in Figure 5.2.
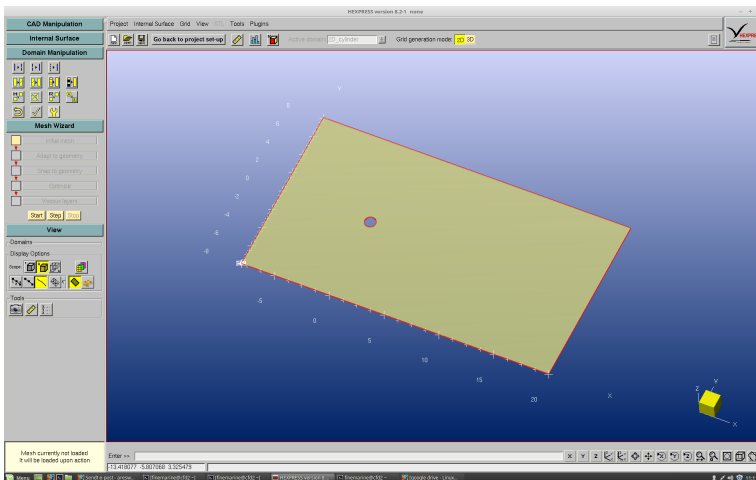
Figure 5.2: HEXPRESS user interface and generated domain geometry

As a means of keeping track of the coordinates, and to make it easier to change the individual domain size parameters, origin is set to the center of the cylinder.

In HEXPRESS you also initiate the grid generation process. Through an interactive user interface it allows you to set up the mesh generation for simpler geometries, like the one in this case study, as well as more complex geometries. The meshing process is completed through the steps depicted in Figure 5.3. This simple interface allows the user to stepwise generate the desired discretization of the computational domain tailored to fit the geometry.

Figure 5.3: HEXPRESS grid generation interface

An important term introduced in during the meshing process is ***refinement***. Refinement is defined as the "level of coarseness" of the cells in the computational domain. In FINE/Marine this level is specified by a number, with zero being the lowest number of refinement, and increasing number indicating a finer mesh. The cell size difference from one refinement level to the next is divided by a factor of two. The effect of this can be illustrated by setting the initial cell size to unity. This indicates that the cell size in the next refinement level (1) is twice as small, namely 0.5. For refinement level 2, the smallest cell size will be equal to 0.25, and so on. With this in mind it is easier to keep track of what is the smallest cell size in the model, thus giving an indication on how coarse or fine the mesh is.

The first step consist of creating the ***initial mesh***, which in this case study is set to 1m. Thus, with a domain length in x direction of 28 m, we get a total number of cells of 28 in that direction. The initial mesh is illustrated in Figure 5.4a. The next step involves the ***Adapt to geometry***, which allows you to tailor the mesh more around the specific geometry. In this case study we know that the areas of most interest (most complex flow characteristics) is around the cylinder, and in the wake. It is possible to create so called "box refinements", which are rectangular areas where the user can specify the number of refinements. In addition to the box refinements there is also an option to use surface refinements, where the user can specify number of refinements in proximity of the body, which in this case is around the cylinder. Both the box refinement and the surface refinement

can be observed in Figure 5.4b, where the number of refinements are 2 and 1 respectively. This indicates that the global number of refinements in the computational domain is equal to: $N_{global} = N_{box} + N_{surface} = 2 + 1 = 3$. With the cell size of 1m as initial value, we then know that the smallest cell size in the computational domain is $1m/2^{N_{global}} = 0.125$, and that these cells are located closest to the cylinder.

(a) Initial mesh (b) Box and surface refinement (c) Viscous layer
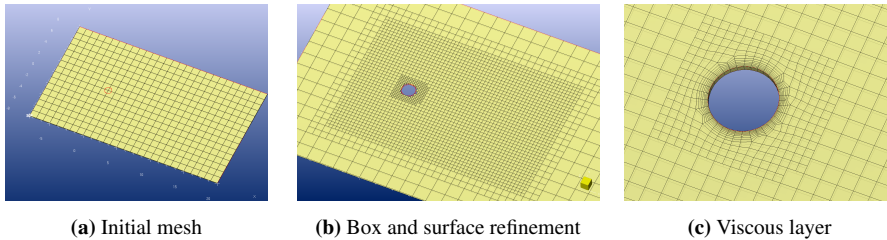
Figure 5.4: Refinement steps from HEXPRESS visualized

The next steps in the mesh generation process is the ***Snap to geometry*** and the ***Optimize*** steps. This includes the procedure of attaching the cells to the geometry, and optimizing the geometry of the most distorted cells in order to reduce the chance of numerical errors. These two steps are automatically performed by the software engine. The final step, ***Viscous layers***, is an important step as it is designed to resolve the boundary layer that forms along the surface of the geometry. Here, you can choose the total number of layers/refinement levels, as well as the stretching ratio that ensures a gradual transition between the viscous layer and the surrounding cells. As a rule of thumb the number of layers required to capture the boundary layer flow is in the area 5-10, and a stretching ratio of 1.2. However, this is highly dependent on the flow characteristics and the geometry itself, and knowledge about the boundary layer thickness should always be taken into account. An example of the viscous layer created in this case can be observed in Figure 5.4c.

5.2 Mesh refinement study

In order to ensure that the grid refinement is of high quality, and whether the flow is fully resolved, a convergence test can be performed. A larger total number of cells within the computational domain means longer computational time. Therefore it is important to find the point where solution accuracy and computational is most optimal. A mesh convergence study involves testing different mesh refinement configurations, and comparing the resulting output values, as well as the visual flow characteristics. If the mesh is too coarse there will be large numerical inaccuracies, as the solver will not be able to capture the areas where the change in flow velocity/pressure is large. This effect is particularly dominant in the proximity of the cylinder, where the flow accelerates around the body, and the boundary layer forms.

For a laminar flow around a cylinder the boundary layer thickness can be approximated by the relation $\delta = \frac{1}{\sqrt{Re}}$. In relation to this it is possible to estimate what the cell size of the cells closest to the surface should be, in order to capture the whole boundary layer

flow. With $Re = 100$ the thickness is approximated to be around $\delta = 0.1$. As mentioned in the previous section there should be a total of 5-10 cells within the boundary layer, with a stretching ratio of approximately 1.2. This indicates that the smallest cells closest to the surface should be approximately 0.01.

The mesh convergence study in this case study is performed for five computations with five different mesh refinement configurations. The following table (Table 5.1) gives an overview of the parameters used in the five computations. For the sake of consistency all the computations the same computational domain has been used ($Y = 8m$, $X_1 = 8m$ and $X_2 = 20m$), as well as the same time step $\Delta t = 0.05$.

Table 5.1: Mesh refinement parameters of different computations

	Mesh properties	Computation 1	Computation 2	Computation 3	Computation 4	Computation 5
	Total no. of cells	4563	7896	12235	18678	21566
Global properties	Initial mesh size	1	1	1	0.5	0.5
	Smallest mesh size	0.125	0.0625	0.03125	0.015625	0.0078125
Initial mesh	No. of cells	28*16=448	28*16=448	28*16=448	56*32=1792	56*32=1792
	Global no. of ref.	3	4	5	6	6
Adapt to geometry	Box ref. no.	2	2	3	3	4
	Surface ref. no.	1	2	2	3	2
	First layer thickness	NO	NO	NO	0.01	0.01
Viscous layer	Stretching ratio	NO	NO	NO	1.2	1.2
	No. of layers	NO	NO	NO	8	8

Because HEXPRESS has got many different options when it comes to configuration of the mesh refinement, it is challenging to know which features are most important for the quality of the mesh. This is one of the problems that can be explored by conducting a convergence study. For that reason the five computations explore the effects of different levels of refinement, to observe at what level the solution converges. Table 5.1 shows that for the first two computations the box refinement level is constant at 2, while the number of surface refinements is increasing from one computation to the next. The third computation has a total number of global refinements equal to 5, indicating that the smallest cell size in the computation is 0.03125. For the two last computations the number of refinements are increased further, and the viscous layers are added. This has been done to observe the effect of a more resolved boundary layer. The smallest cell size for the fifth computation is 0.0078125, which is smaller than the approximated cell size computed earlier of, 0.01. For that simulation it can be assumed that the boundary layer more or less have been resolved.

As a means of comparison, the mean drag coefficient has been used to compare the numerical solutions from the five computations. As the drag coefficient is calculated by integrating the surface pressure over the cylinder, it might be a source of error, and the solution may deviate somewhat from the "correct" solution. Figure 5.5 shows the time series of the oscillating drag coefficient for the five computations. The simulations have been running for a total of 250 seconds to ensure that the flow reaches a steady flow, with steady oscillations. The plot is based on the force history text files that are written out during the simulations. The drag coefficient (and lift coefficient) are calculated based on Equations 2.12 and 2.13 from Chapter 2.
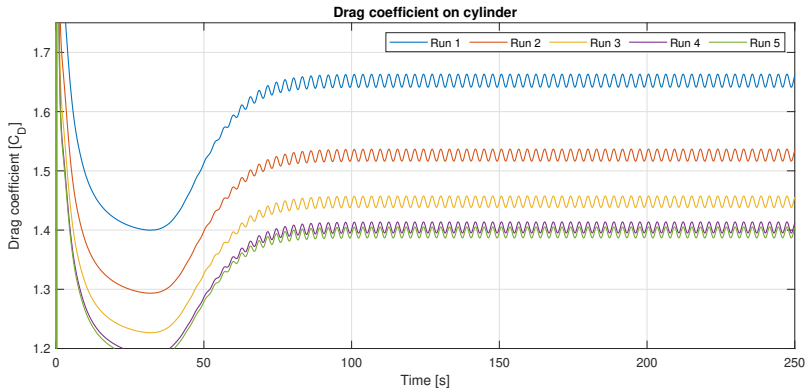
Figure 5.5: Comparison of drag coefficients of Run 1-5, with different number of cells and grid structure

Figure 5.5 show that the force oscillations are initiated at approximately 50 seconds. These oscillations appear as a result of the vortex shedding, a phenomenon expected to occur at this Reynolds number. After approximately 100 seconds the oscillations reach a steady state, and it is the results from this point and onward that are most interesting when calculating the mean drag coefficient. The mean drag coefficients from the five simulations are plotted in the following convergence plot, Figure 5.6, as function of total number of cells in the computational grid. The plot shows how the mean drag is decreasing with increasing number of refinement levels, and thus total number of cells. The solution clearly converges towards one value, as expected, since the mesh for the two last simulations were performed with a viscous layer ensuring the resolving of the boundary layer. To further validate the solution from the simulations two external sources (Calhoun, 2002) and (Wang et al., 2009) are used as reference values. The values are extracted from similar studies, where roughly the same flow parameters have been used. Table 5.2 show the resulting mean drag coefficient from the simulations compared to the reference values.

	$C_{D_{mean}}$	Cells
(Calhoun, 2002)	1.33	-
(Wang, 2009)	1.379	-
Run 1	1.651	4563
Run 2	1.526	7896
Run 3	1.447	12235
Run 4	1.401	18678
Run 5	1.295	21566
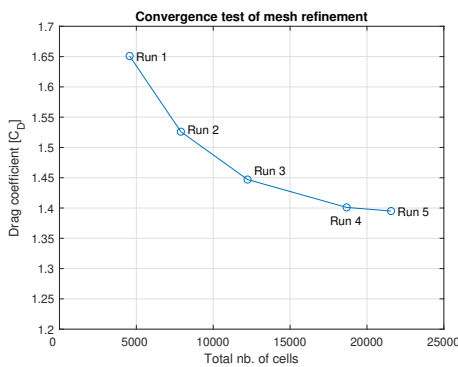
Figure 5.6: Mean drag coeff. for Run 1-5

Table 5.2: Reference data comparison

From the convergence test it is reasonable to assume that Run 4 and Run 5 have a sufficient mesh refinement. This indicates that the number of cells needed to achieve a sufficiently accurate solution is in the area between 15 000 and 20 000 cells. However, it is very important to keep in mind that the number of cells alone will not give the best results. The placement of the smaller cells is equally important.

Another good method of finding out if the boundary layer is fully resolved is to visually compare plots of different computed values, and the applied grid.

(a) Pressure contour with applied grid   (b) Velocity in y-direction with applied grid
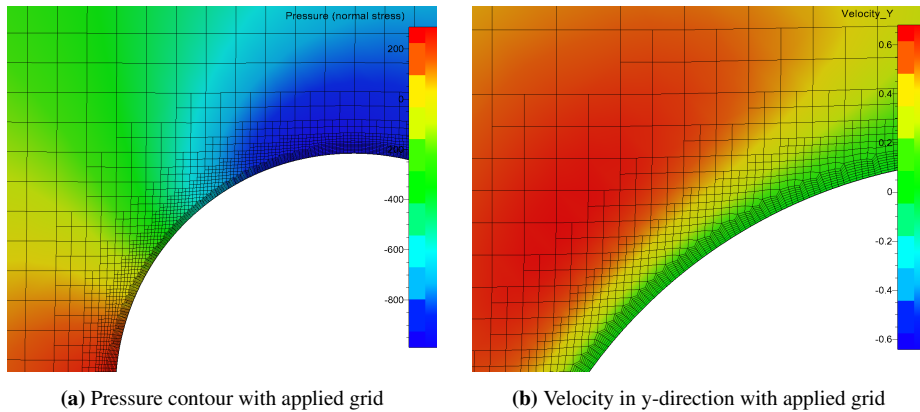
Figure 5.7: Comparison of computational values and applied grid

Figure 5.7 shows both a pressure contour plot and velocity in y-direction, with the applied grid drawn on top. By comparing the size of the cells near the surface of the cylinder with the visual flow characteristics of the boundary layer it can be determined whether to add more cells or not. The boundary layer is most visible in Figure 5.7b where the green shading shows velocities close to zero. The overlying grid clearly covers the lower part of the boundary layer, but can possibly consist of a thicker layer of fine grid to completely capture the whole boundary layer flow. However, as the values calculated earlier tell us, the results are not too influenced by this. If an area around the body shows large differences in velocity or pressure from one cell to the next, it is desirable to increase the refinement at that point. This is again a case of trial and error, always closely monitoring the flow characteristics in connection to the grid.

The result from the grid refinement study can be summarized as follows. Run number 4 is found sufficient when it comes to grid refinement and cell placement, as the results from the convergence test shows that the mean drag coefficient is reaching a point of convergence, close to the reference values provided. The mesh surrounding the cylinder surface is also thought to cover most of the boundary layer flow, resulting in a sufficient resolving. For these reasons the mesh configurations from Run 4 (18 678 cells) will be used when proceeding with the case study. Figure 5.8a and 5.8b shows the final configuration of mesh refinement, with placement of box refinement covering the wake behind the cylinder, and surface refinements covering the area in proximity of the cylinder surface.

(a) 2D mesh configuration Run 4   (b) Viscous layer near cylinder
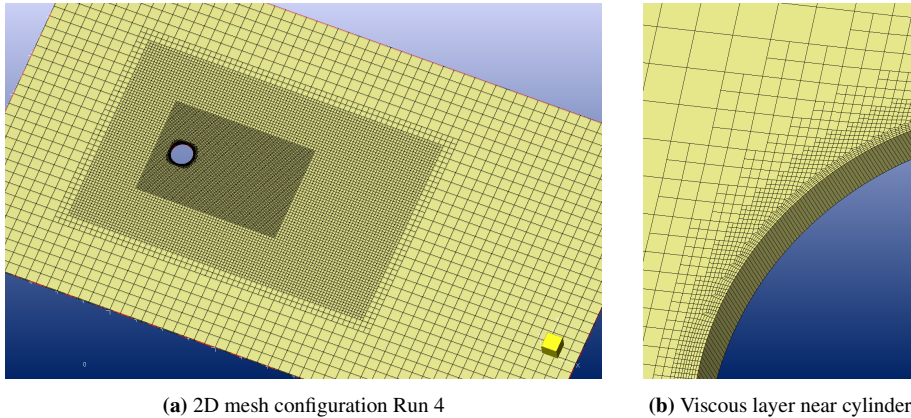
Figure 5.8: Configuration of final mesh refinement

5.3 Influence of domain size

In Chapter 3 definition of different boundary conditions were discussed. When it comes to the two-dimensional flow in this particular case study, some of these boundary conditions have been applied. For the cylinder surface, a no-slip boundary condition has been specified. The boarders of the computational domain (inlet upper and lower wall, outlet) have all been specified with constant velocity boundary conditions, meaning $u = 1$ in the flow direction (x-direction). This indicates that the fluid is in a way "dragged" through the computational domain. The flow inside the computational domain must meet the criteria of the applied boundary conditions in order to solve the numerical equations correctly. In other words this implies that when the fluid experiences an acceleration over the surface of the cylinder, the free stream velocity changes due to viscous effects. The computational domain will give the best solutions if the velocities near the boundaries are as close as possible to the applied boundary conditions

For the sake of computational time, the computational domain should be as small as possible, without being so small that the results are polluted by the applied boundaries. To ensure that this is not the case for the computational domain in this case study, a domain size test has been conducted. Three different domain sizes have been tested in order to find the most optimal one. It is worth mentioning that the boundaries that most probably will have the most influence on the flow are the upper and lower boundaries. The inlet boundary is assumed to not influence the flow around the cylinder to a large degree because the nature of the stagnation (upstream disturbance). The wall boundaries however can pollute the free stream in the domain, and must be investigated further with different lengths of Y, as illustrated in Figure 5.1. Different methods have been used in order to determine the quality of each domain. For comparison between the three domain types, mean drag coef-

ficient, Root Mean Square (RMS) of lift coefficient, and Strouhals number have been used.

For all the computations performed for the three different domain sizes, the same grid refinement has been used. This has been done in order to ensure the consistency, and to be able to achieve better comparisons between calculated values. The table below shows resulting values for the three computational domains, with height values $Y = 5m$, $Y = 8m$ and $Y = 10m$ (from origin of cylinder to top boundary).

Table 5.3: Table of results from three domain sizes

DOMAIN	1 (Y = 5m)	2 (Y = 8m)	3 (Y=10m)
Number of elements	15 539	18 678	23 281
C_D mean [-]	1.428	1.404	1.398
C_L RMS [-]	0.2046	0.2024	0.2028
St [-]	0.170	0.169	0.169

The mean drag coefficient is calculated in the same manner as earlier, as well as the lift coefficient. All measurements have again been performed in the 120-250 seconds region in order to ensure a stable developed flow. Because the lift coefficient is oscillation about zero, a better way to express its mean value is through a Root Mean Square calculation. This is done by taking the square root of the average lift coefficient squared. The final value used in the comparison is the Strouhal number, the dimensionless number describing the oscillating flow. The Strouhal number is calculated by monitoring the pressure at a point in the wake close to the cylinder. We know for a fact that the pressure will oscillate as the vortices are shed from the cylinder, and thus it is possible to detect the vortex shedding frequency between two similar values in the cycle. I order to retrieve as accurate measurements as possible, the frequency is monitored over several periods of shedding.

The result from the domain comparison show that there are significant differences in mean drag coefficient between the three domains. However, between the 2nd and the 3rd domain the change in coefficient is not that large. The RMS of the lift coefficient is not that sensitive to change in domain size. Moreover, the Strouhal number is also showing signs of independence between the three domains, indication that the separation frequency is not very sensitive to the computational domain inconsistency.

Another method used to observe what effect the top and bottom wall boundaries have on the flow field inside the computational domain, is plotting of velocity profiles. Velocity profiles have been monitored from the top of the cylinder, and radially outwards along a line towards the end of the domain. By doing this it is possible to determine the exact point the flow has returned to its initial inlet velocity. Figure 5.9 show three velocity profiles plotted from the top of the cylinder into the fluid, for the three domain configurations. The velocity measured is velocity in x.direction, meaning the streamwise direction, and this value is plotted against distance from the cylinder in meters.
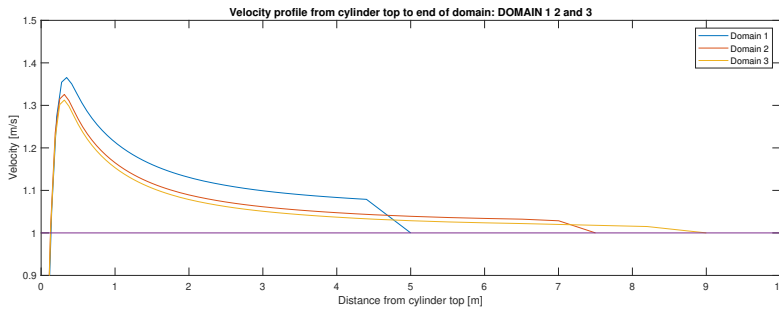
Figure 5.9: Comparison of velocity profile for different domains

The blue line in Figure 5.9 shows the velocity profile for the smallest domain. A clear and visible abrupt change in velocity occurs close to the boundary (at 5m from cylinder). This change indicates that the the domain is not large enough, as the velocity in the free stream has not reached the same level as the boundary condition at the upper wall in the domain ($u = 1m/s$). For the larger domains this effect decays, and the streamwise velocity converges towards the boundary condition value. It is also worth mentioning that also the maximum velocity is sensitive to change in domain size. This observation can be directly linked with the previous finding of the drag coefficient being highly dependent on domain size.

From the test it is possible to draw the conclusion that Y-values greater than 7-8 will give sufficient results, with increasing accuracy as the domain size increases. However, when we later move into the realm of 3D flow, and the computational domain increases with another dimension, it becomes even more crucial to make the domain as small as possible without compromising the results. The following calculations will proceed with the same mesh refinement, and with computational domain configuration similar to Domain 2.

5.4 Sensitivity analysis for different time step

Another important part of CFD calculations is the time step between calculations. The Navier-Stokes equations are time dependent, and thus time integration is necessary. If the time step is to large, the solver will have difficulties iterating between results. To prevent the solution to "explode" it is appropriate to choose a maximum number of iterations between different solutions to 8 (typically between 5-10). Table 5.4 shows a comparison of three runs with different time step, and the same two reference values used in the refinement study. It can be seen from the table that the values from the largest time step deviates somewhat from both reference values. However, for the two smaller time steps the values are more consistent and do not deviate. This might indicate that time steps in that range will yield a satisfactory solution. One important point however, is how the computational time increases drastically between the different time steps. This means that while we can observe an improvement of the solution when using smaller time steps, it comes at a cost as

the computational time increases. This observation is very valuable for future calculations, especially when we transit to 3D flow, and the number of cells increase drastically.

	$C_{D_{mean}}$	$C_{L_{max}}$	St	Computational time
(Calhoun, 2002)	1.33	0.298	0.175	–
(Wang et al., 2009)	1.379	0.357	0.17	–
Run 0.1	1.42	0.41	0.19	19 min
Run 0.01	1.34	0.32	0.18	2h 17 min
Run 0.005	1.33	0.31	0.18	4h 13 min

Table 5.4: Lift, drag and Strouhals number for different time steps

In order to determine the quality of a numerical simulation, it is important to know whether the solution converges smoothly. This can be determined by use of the ***Courant-Friedrichs-Levy*** (CFL) number. The CFL number gives the relationship between the time step (Δt) and the refinement cell size (Δx). For the solution to satisfy the requirements of time step iterations the CFL number must be smaller than 1. The CFL number is given by:

$$CFL = \frac{u\Delta t}{\Delta x} < 1 \qquad (5.1)$$

The extraction of CFL number in FINE/Marine is limited to multifluid calculations, which means that a manual test must be performed in order to obtain these values. To determine the CFL number for the runs, the local velocity is extracted from 3 cells with different cell sizes. The resulting calculations can be observed in Table 5.5.

Time step	CFL Point 1	CFL Point 2	CFL Point 3	**CFL Max**
0.1	1.024	1.235	0.567	**1.235**
0.01	0.355	0.327	0.218	**0.327**
0.005	0.124	0.0979	0.0288	**0.124**

Table 5.5: CFL number of three chosen points in the fluid domain

For the first time step the CFL_{max} value is above 1, which means that this time step should be rejected. For the CFL values lower than 0.1 the (run with time step 0.005) a finer mesh should be applied in order to get a more optimal solution.

It is important to note that the CFL number only was extracted from three cells in the domain. Ideally it should be extracted from all the cells in the domain. The calculations of CFL numbers can in this case only be used as a rough estimate. It should also be mentioned that the differences in lift and dag coefficients are small between the different Δt values. This may be caused by the large differences between Δt and Δx in the calculations with $\Delta t = 0.005$. The computations can be carried out with a finer mesh to obtain better results, but that will have a great impact on the computational time.

The results from the time step analysis show us the importance of applying the right Δt for the specific mesh refinement, especially with regards to the smallest cells in the grid. In this case study, for this particular grid configuration, time steps smaller than 0.01 is recommended. However, in further calculations there might be needed to make computational compromises in order to keep the computational time to a minimum. In this case study the maximum number of cells is never exceeding 25 000, which is possible to solve with standard size laptops. When we later will look at three-dimensional flow cases, the number of cells in the computational grid is expected to increase drastically (in the millions), and the importance of using appropriate time step is even more evident.

Chapter 6

Step cylinder simulations Results and discussion

After completing the validation case it becomes easier to expand the flow case and explore different and more complex geometrical configurations. The main motivation of this thesis surrounds the topic of stepped cylinders, and the natural step from a modelling perspective is to move into the realm of three-dimensional flow.

It has been mentioned earlier that working with CFD is a very extensive and iterative process. For flow problems extending beyond the current literature, new observations can be made as the model develops, and new territories within the field can be discovered. The reason why this is mentioned is because this thesis reflects exactly that. The underlying motivation is known, but the finish line is not determined. However, a general approach to the modelling will be given in the following sections, attempting to clarify what will be modelled, and why.

6.1 Modelling approach

A natural place to start the investigations is to expand the two-dimensional case, and make it three-dimensional. In addition, the choice has been made to jump straight into the case of step cylinders to maximize the available time and resources on that specific topic. In the early stages of the 3D modelling it is important to first and foremost define the geometry and apply a suitable mesh. Knowledge from the validation case study will be very valuable here, however additional considerations have to be made as we now can expect to observe 3D interactions in the wake. Similarly to the validation case, the mesh topology consists of initial refinements, box refinements, surface refinements, and viscous layers. As we now have an additional dimension (spanwise/z-direction), the number of cells in the horizontal plane is multiplied with the number of cells in spanwise direction, leading to a drastic increase in total cell in the computational domain, which again will lead to

increased computational time.

In a recent study performed by (Mortensen, 2019) the characteristics of mesh topology concerning 3D cylinder flow for low Reynolds numbers have been studied. The investigations concern both the spanwise number of elements, and the placement of the box refinement. The study is performed in FINE/Marine, for a straight circular cylinder with spanwise length $L_Z = 12D$ and $Re = 200$. The cell aspect ratio between streamwise and spanwise is defined as $\alpha = \frac{\Delta Z_1}{\Delta X_1}$. Aspect ratios of 1, 2 and 4 are tested in three separate simulations, and λ_2 vortex detection is used to compare the details of the vortex structure. Results from the visualization of both $\alpha = 4$ and $\alpha = 2$ show signs of streamwise vortices in agreement with the Mode A findings of (Williamson, 1996). However, the visualization of $\alpha = 1$ yields a more complicated and detailed wake regime. It is concluded from the refinement test that an aspect ratio of 1 will reveal more wake detail, and retrieve more reliable results.

(Mortensen, 2019) also conducts box refinement trials to investigate the effect of using different box sizes in the grid discretization process. Figure 6.1 shows the three different box dimensions used in the study.

(a) Box 1 dimensions   (b) Box 2 dimensions   (c) Box 3 dimensions
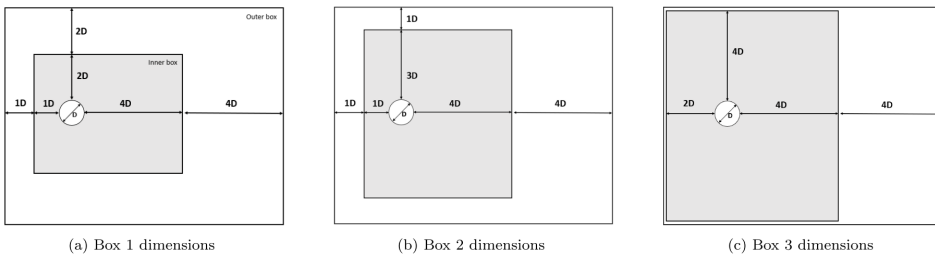
Figure 6.1: Box refinement dimensions, taken from (Mortensen, 2019)

The three mesh configurations are run through the same simulation process, and the resulting force components on the cylinder are used as comparison. In addition the level of detail in the wake is investigated for the three configurations. The results show that there are almost no differences in the resulting force between the three (only 1.6 % between larges and smallest drag coefficient). The conclusion from the box refinement trial is that the dimension of the refinement boxes tested does not directly affect the solution. The choice of refinement configuration is more or less decided by the desired level of flow detail in the wake. A long box refinement should be applied if the far wake visuals are demanded, and a smaller box if the wake close to the cylinder is of more interest. Again, the balance between results and computational time should be taken into account.

The results from the study of (Mortensen, 2019) will be taken into account when the model in this thesis is constructed.

6.2 Characteristics around the step

In order to gain confidence in the numerical model, simulations of flow around a step cylinder with diameter ratio $D/d = 5$ and $Re_D = 150$ has been compared with similar studies. The things that has been used in the comparison is the visual aspect of the flow structure around the step, and the vortex structure in the wake. The most prominent studies on this topic are discussed in the literature review (Chapter 3), and include (Dunn and Tavoularis, 2006) and (Morton and Yarusevych, 2010).

Initially the aim is to capture the most defining characteristics of flow over step cylinders. Figure 6.2a shows the visualization of an experiment performed by (Dunn and Tavoularis, 2006). Here, the diameter ratio D/d = 2 and Reynolds number $Re_D = 1230$. The figure clearly shows the detected recirculation bubble created at the upstream part of the step, in the junction between the large and the small cylinder. This rotating flow is the birthplace of the junction vortices appearing in the wake behind the step. Figure 6.2b shows a visualization of velocity vectors plotted in the same plane, at the leading edge of the step, for D/d = 2 and $Re_D = 150$. It is important to note that the Reynolds number is different in the two cases, a fact that has to be taken into account when making comparisons. However, the results from the simulation in 6.2b show many similarities to the experiment, as one should expect. For higher Reynolds numbers it is also expected to observe a more dominant rotation in the flow at the junction.
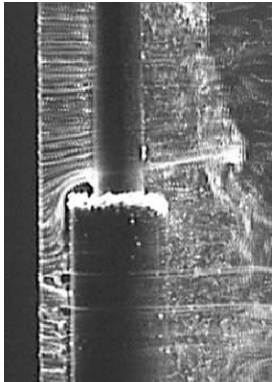
(a) Recirculation bubble detected in experiments performed by (Dunn and Tavoularis, 2006), D/d =2 and $Re_D = 1230$
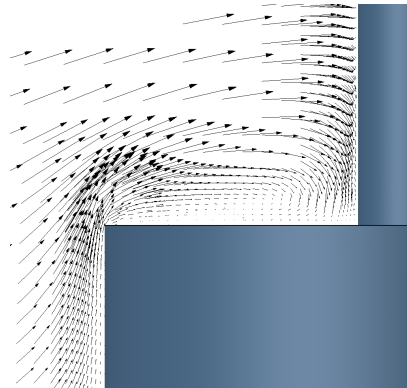
(b) Velocity vectors plotted in x-z-plane at leading edge of step, D/d = 5 and $Re_D = 150$

Figure 6.2: Comparison of flow at leading edge of step

From the literature review it is clear that of the more dominant and characteristic features of the step cylinder flow, are junction vortices and edge vortices. An attempt is made for the current simulation to visualize these effects, and again compare them to the experimental results of (Dunn and Tavoularis, 2006) and numerical results of (Morton and Yarusevych, 2009), to see if there are similarities.

Figure 6.3a is extracted from the numerical results of (Morton and Yarusevych, 2009). The figure show the clear development of both streamwise edge vortices and junction vortices. The visualization is based on vorticity detection, where the light grey color represents negative streamwise vorticity and dark grey represents positive streamwise vorticity. For this particular representation a step cylinder of D/d = 2 and $Re_D = 1100$ is used. Figure 6.3b shows a visualization of velocity streamlines from the same perspective, viewing downstream direction. You can clearly see how the fluid flows around the smaller cylinder when it reaches the junction. However, it is difficult to see whether the disturbance of the flow is sufficient to create vortices, and thus to conclude that we can observe junction vortices at this Reynolds number. There are no current references discussing at what Reynolds number junction vortices appear. By combining the figures 6.2b and 6.3b it is however reasonable to assume that we observe an initial stage of the junction vortex forming process. The rotation of the fluid at the junction combined with how the fluid curls around the small cylinder make the foundation of the creation of streamwise rotating vortices.
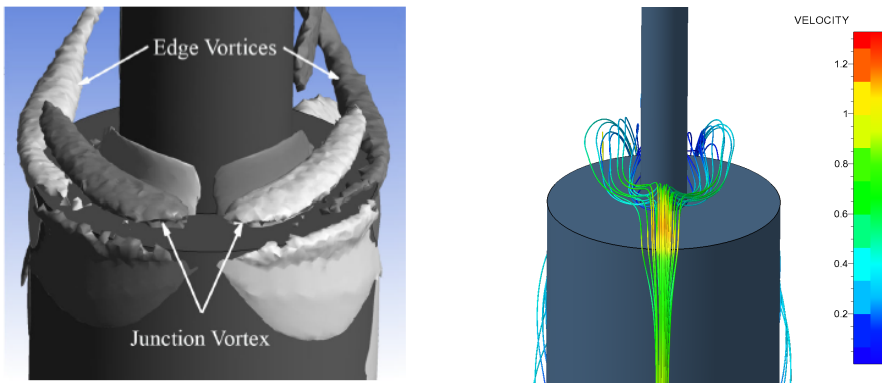
(a) Edge and junction vortices around step, 3D vorticity visualization, (Morton and Yarusevych, 2009)

(b) Visualization of velocity streamlines seen in streamwise direction

Figure 6.3: Comparison of vortex formation around the step

A visualization of the edge and junction vortices observed in the experimental studies of (Dunn and Tavoularis, 2006) can be seen in Figure 6.4a. The arrows point to the streamwise vortices created at the step of the cylinder. The figure to the right, Figure 6.4b, shows velocity streamlines flowing around and over the step of the D/d = 5 cylinder in the current simulation. The same conclusion can be made here, as for the junction vortices in the previous figures. No clear observations of the junction and edge vortices can be made for this particular low Reynolds number ($Re_D = 150$). However, the nature of the flow seems to follow the same pattern as for flows over other step cylinder configurations. The flow tips over the leading edge and washes over the sides of the large cylinder, and the flow close to the junction curls around the smaller cylinder. A clear observation that can be made from Figure 6.4b is the significant downwash that occurs as the flow washes over the trailing edge of the large cylinder. This phenomenon is known to create large three-dimensional disturbances in the wake behind the cylinder, and the effect of this will be investigated and discussed in the following chapters.

(a) Edge and junction vortices observed through experiments performed by (Dunn and Tavoularis, 2006), $Re_D = 1100$

(b) Flow around the step visualized by velocity streamlines seen in streamwise direction, $Re_D = 150$
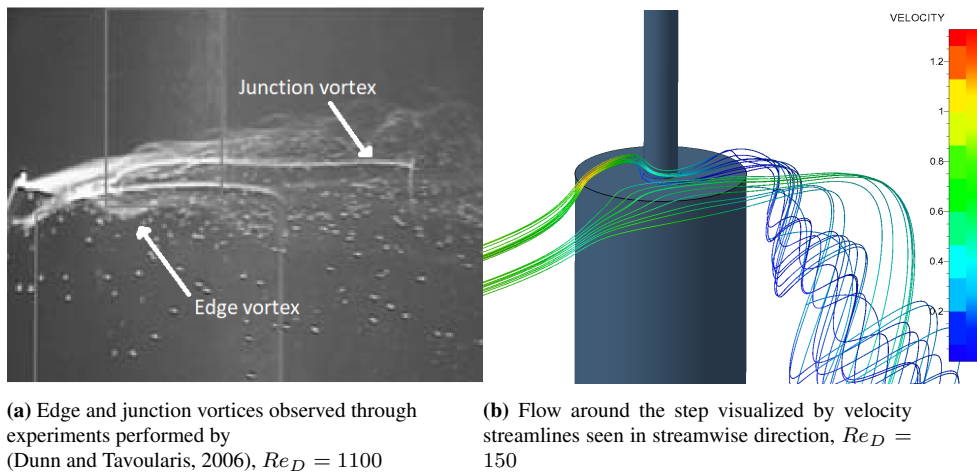
Figure 6.4: Comparison of vortex formation around the step

An important observation that can be made from the study of flow characteristics of the step, or any given geometry in general, is how the mesh is discretized and distributed around the body. In this case, when we want to look at the smallest details of the flow close to the cylinder, placement of the smallest cells is crucial. A fine grid close to the surface will give the model a better ability to capture the more complex characteristics of the flow. The conclusion is that if you want to pay extra attention to the detailed flow around the step, a finer mesh should be applied in that area of the domain. Figure 6.5 shows how the distribution of cells is close to the step, and what are an additional box refinement ideally should be placed to capture more flow details.
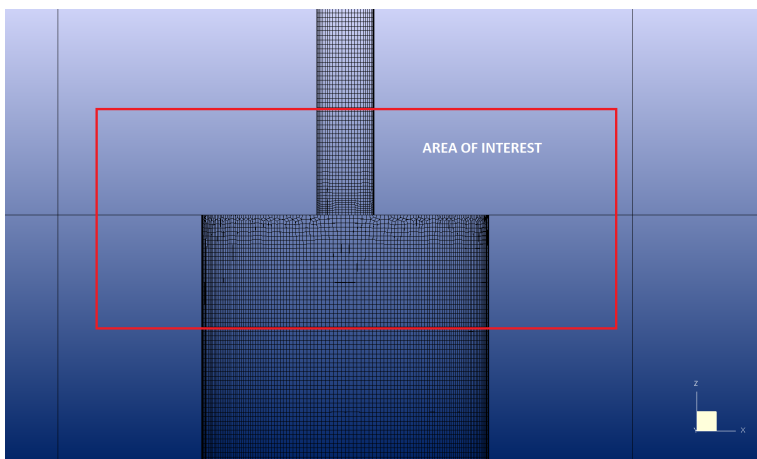
Figure 6.5: Current mesh for D/d = 5 step cylinder and area of interest for flow characteristics

6.3 Wake structure and spanwise length of step cylinder

In the previous section the phenomenon of downwashing and three-dimensional wake disturbance was discussed. The next natural step in the thesis is to explore the wake, and to observe the characteristics of vortex structures for different step cylinder geometries. The initial simulation was performed with the following dimensions and parameters:
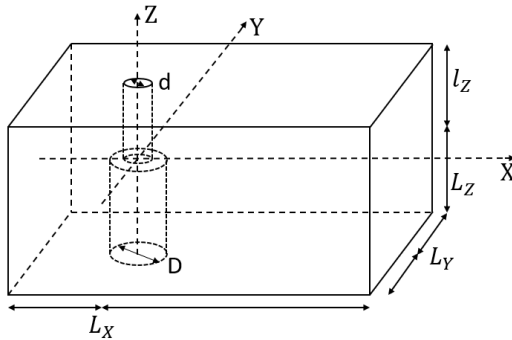
Figure 6.6: Computational domain dimensions

Computational domain parameters	
Domain length L_X	28 m
Domain width L_Y	16 m
Domain height $L_Z + l_Z$	10 m
Cylinder dimensions	
Small cylinder height l_Z	5 m
Small cylinder diameter d	0.2 m
Large cylinder height L_Z	5 m
Large cylinder diameter D	1 m
Flow parameters	
Reynolds number	150

Table 6.1: Parameters used in the initial step cylinder simulations

The length of each cylinder as well as the diameter ratio has proven to be determining for the wake flow structure. As mentioned in the literature review, (Lewis and Gharib, 1992) report of two distinct vortex interaction modes in the wake, namely *direct* and *indirect* modes. The direct mode is found to occur for diameter ratios smaller than 1.25. In this mode the vortices shed from both the small and the large cylinder interact directly in a narrow region close to the step. For larger diameter ratios (D/d > 1.55), the indirect mode is observed. This mode describes the indirect interaction between the vortices shed from the small and large cylinder, and the appearance of three distinct shedding frequencies. The area of interaction is defined as the N-cell region, and is one of the more dominating features of the step cylinder. The region behind the small cylinder is defined as S-cell, and the region behind the large cylinder L-cell.

(Norberg, 1992) reports that the influence of the N-cell region stretches as long as 10D (spanwise direction) in to the wake behind the large cylinder. This indicates that the current length of the large cylinder in the simulation, $L_Z = 5D$, is to short to properly capture the whole shedding interaction of the small and large cylinder. Figure 6.7 shows a visualization of the the initial simulation of the step cylinder, with parameters as shown in Table 6.1. The figure depicts the vortex detection λ_2 for velocity, and gives an indication of how the vortex structure is in the wake.
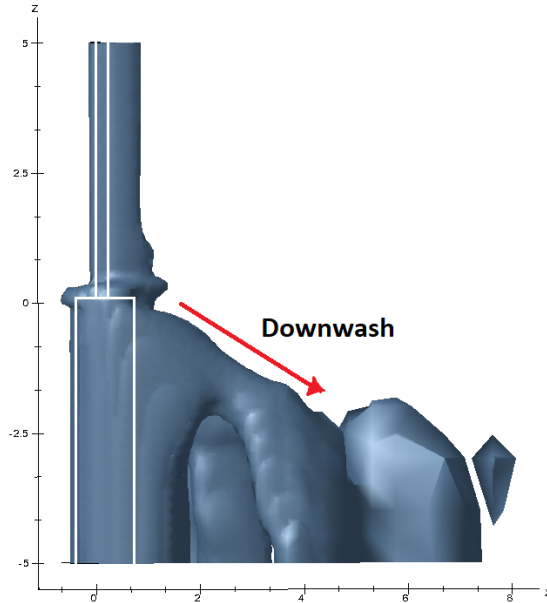
Figure 6.7: Initial simulation of step cylinder, Re = 150, D/d =1 and L/l = 1, $\lambda_2(velocity)$

Many interesting observations can be made by observing the initial model of the step cylinder flow. First and foremost we can see that observable vortices are only shed from the large cylinder. In the simulation $Re_D = 150$ which means that the Reynolds number of the small cylinder is five times as small, $Re_d = 30$, and thus we can expect to see little to no shedding. However, a clear influence of the flow over the step can be observed by the inclination of the vortices. Moreover, the importance of a well defined mesh is also visible in the figure. The last vortex structure to the right in the image is coarse and pixelated, indicating that the flow here is not resolved properly. All these observations combined are valuable in order to determine the next step of the simulation process. It is now clear that the next simulation will require some changes in order to properly capture the vortex structures in the wake behind the step cylinder. These changes include; longer spanwise length of the large cylinder and a finer mesh in the wake behind the step cylinder.

A simulation for a 10D step cylinder reveals that the interaction region behind the step is still not showing properly, and that there is no clear spacing between each separated vortex. The initial simulation was run for 500 000 cells, and the second simulation for about 1.2 million cells. By increasing both the length of the cylinder and the level of refinement we can see a clear change in computational time. It is apparent that an even larger spanwise length of the large cylinder is required, as well as a higher level of refinements.

The next simulation is performed for a 15D step cylinder, with the small cylinder length is unchanged. Figure 6.8a shows the isosurface representation of λ_2 for the 15D step cylinder. The snapshot is captured after 200 seconds, and the flow is at this time instance fully developed. For this geometric configuration we can more clearly see the interaction region between the disturbed flow in the wake of the step and the vortices shed from the large cylinder. As a comparison, the experimental results from experiments performed by (Dunn and Tavoularis, 2006) are visualized in the figure to the right, 6.8b.
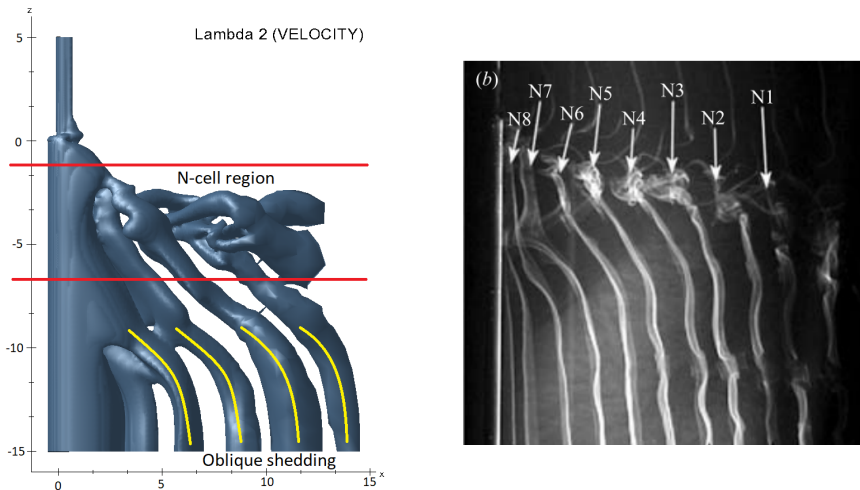
(a) Isosurfaces of $\lambda_2 = -0.01$ depicting vortex shedding in wake of step cylinder, D/d = 5 and $Re_D = 150$

(b) Experimental results showing vortex structure in wake behind a step cylinder with D/d = 2 and $Re_D = 152$, (Dunn and Tavoularis, 2006)

Figure 6.8: Comparison of vortex formation in the wake behind the step cylinder

Both figures have the same Reynolds number, but the diameter ratio is slightly different. Nevertheless, the comparison shows clear similarities. Because of the difference in D/d, the simulation results will not show the same vortex shedding occurring behind the small cylinder, but the interaction region in the wake behind the step, N-cell region, is in good agreement with the experimental results. From the simulation the N-cell region can be identified from $z/D = -1$ to $z/D = -7$. In addition to the vortex structure in the N-cell region we can see a clear example of oblique shedding occurring in the region $-8 > z/D > -14$.

Additional snapshots have been added to clearly identify both the phenomenon of oblique shedding as well as the downwash. 6.9a shows a contour plot of the crossflow velocity in the wake of the step cylinder. The positive and negative velocities in y-direction clearly highlight the alternating shedding from the large cylinder. The oblique shedding characteristic is also visible. You can also observe how the intensity of the vortex flow is rapidly decaying, gradually approaching the free stream velocity of 1 m/s. Figure 6.9b shows a contour plot of the spanwise velocity in the wake. In the area close to the trailing

edge of the cylinder the effect of downwash is visible, as the blue shaded area.

From Figure 6.9a it looks like the oblique shedding occurs almost for the whole length of the large cylinder. The shedding angle behind the large cylinder, Θ_L, is in the region between $20°$ and $30°$, which is consistent with findings of both (Dunn and Tavoularis, 2006) and (Tian et al., 2017a). At the lowest point on the cylinder, at approximately z/D = 13-14D the vortices straighten out, and show similar parallel shedding as for a single cylinder. It must be noted here that the boundaries at the top and bottom (mirrored boundaries) may influence the results, and cause some source of error. Ideally the large cylinder should be extended further to create a so called "buffer region", thus removing some numerical inaccuracies.

(a) Contour of velocity in y (crossflow), D/d = 5 and $Re_D = 150$

(b) Contour of velocity in z (downwash), D/d = 5 and $Re_D = 150$
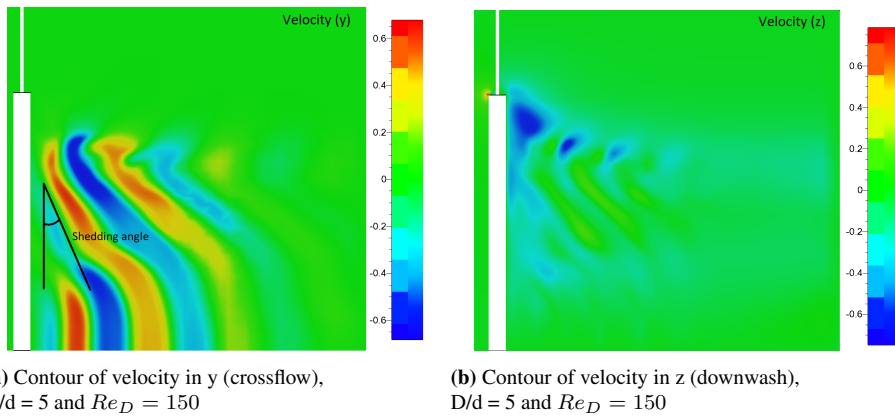
Figure 6.9: Velocity plots visualizing alternate oblique shedding and downwash, 15D step cylinder, Re_D = 150

6.4 Vortex dislocation

A known phenomenon that occurs in many cases of step cylinder flow is ***vortex dislocation***. Due to the difference in vortex shedding frequency for the S-cell, N-cell and L-cell regions, the number of vortices shed in each cell over a period of time is different. The "tension" in the wake that appears due to this difference is corrected by vortex connections. The dislocation occurs when a vortex shedding in a cell does not make a direct connection to a counterpart vortex in an adjacent cell.

Vortex dislocations have been observed for low Reynolds numbers and for small diameter ratios. In their study (Tian et al., 2017a) observe and investigate dislocations and vortex interactions at the N-L cell boundary for cylinder ratios of D/d = 2. It is therefore reasonable to assume that vortex dislocations will occur for the current simulation with Re = 150 and D/d = 5.

Figure 6.10 shows a plot of the force history of the 15D step cylinder at $Re_D = 150$. The simulation is run for 350 seconds. The blue graph shows the drag coefficient of the large cylinder, while the red graph shows the lift coefficient. In the figure you can clearly see the periodic oscillation of the lift, and the alternate shedding from both sides of the cylinder. The interesting thing to notice by observing the graph is how both the lift and the drag have an additional larger oscillating frequency. For example, by monitoring the drag coefficient, we can see that it has the usual small oscillations with twice the frequency of the lift (the "jagged" blue line). However, over a larger period, from about 150-350 seconds a slow oscillation can be observed. For this particular plot the drag oscillation has 6 distinct peaks. This oscillation can be directly linked to the vortex dislocation. Similar findings are presented in the study of (Tian et al., 2017).
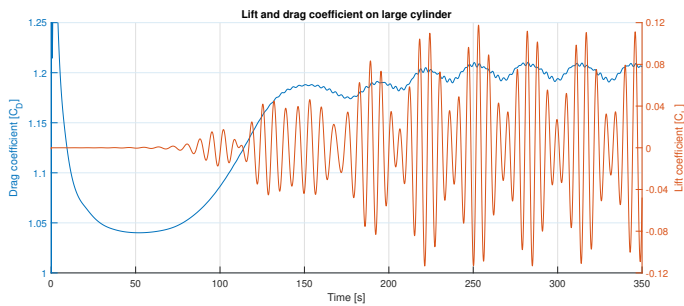

Figure 6.10: Comparison of lift and drag coefficient on the large cylinder for the 15D step cylinder, D/d = 5 and $Re_D = 150$

A good way to confirm this observation is to take snapshots of the vortex structure at different time instances. This way it is possible to capture the dislocation process, and to easier understand its nature. Figure 6.11 shows the isosurface of $\lambda_2 = -0.01$ for six different time instances in the simulation. The samples are taken from 315.5-336 seconds, a period that is measured to be sufficient to capture a whole process of dislocation.

To help with the explanation of each instance, the same numbering system had been used as introduced in the thesis of (Tian et al., 2017a). The vortices shed from each side of the cylinder are distinguished by using different numbering. 1, 2,... indicating vortices shed from the **-Y** side, and primed numbers, 1', 2',... indicating vortices shed from the **+Y** side. N is the index of the N-cell vortices, while L is the index of vortices shed in the L-cell region. In addition colored lines have been used to highlight the most defining vortices in each image. Yellow lines mark vortices shed from the "-Y" side, red lines mark the N-cell vortices, and the green line marks a half loop.

In Figure 6.11 (a) we can observe relatively uniform shedding, meaning direct connections between the N-cell vortices and the L-cell vortices. This is marked by the yellow lines in the figure. On the opposite side we can see the same direct vortex structure. In Figure 6.11 (b) however, the vortex N3 can be observed to disconnect from its adjacent L-cell vortex and connect with the L-cell vortex from the opposite side, L3'.
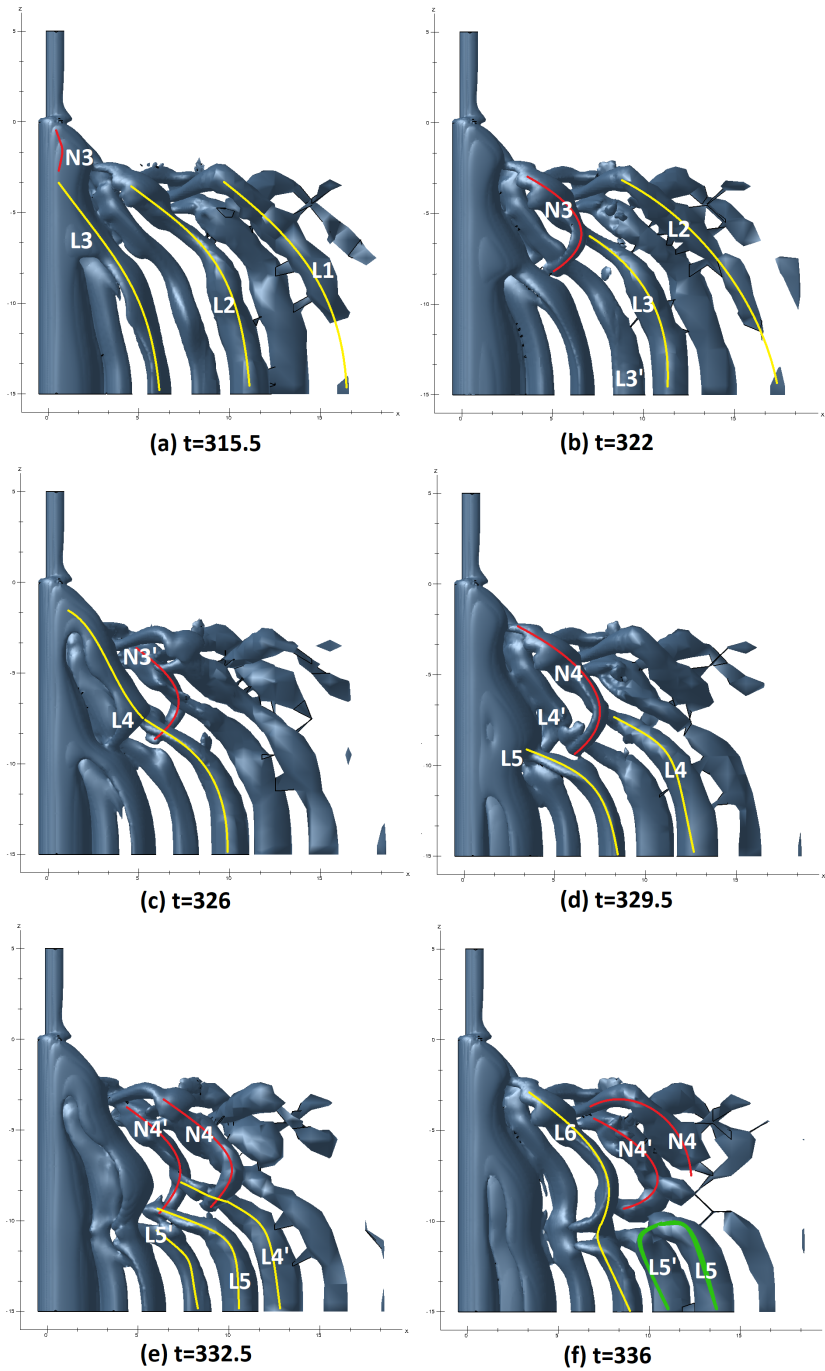
Figure 6.11: Isosurfaces of $\lambda_2 = -0.01$ showing vortex interactions occurring at N-L cell boundary during dislocation process

Similarly in image (c) the next N-cell-vortex, N3' dislocates, and connects with the opposite side L-cell vortex, L4. This process continues as we move to image (d), where the N4 vortex makes a connection with the L4' vortex. The interesting observation that now can be made is that in image (e) the N-cell vortex, N4', looks to have three connected L-cell vortices, namely; L4', L5 and L5'. The progress of this vortex structure can be traced onward to image (f) where we can observe that the two L-cell vortices, L5 and L5' connect to each other in a half-loop. This is marked by the green line. The next L-cell vortex, L6 then connect with its adjacent N-cell (both on -Y side) and forms a direct connection, marked with the yellow line in image (f).

As the L-cell vortex at the final instance have transited back to a direct connection with its adjacent N-cell vortex, a period of dislocation has passed. By observing the following development of the vortex shedding process it is clear that after the dislocation has taken place the offset between the N-cell and L-cell vortices is temporarily corrected. The offset then gradually builds up, until a new dislocation process begins. Figure 6.12 shows the period from the documented dislocation cycle to the next. The period of the vortex dislocations for this particular 15D step cylinder is found to be approximately 30 seconds.
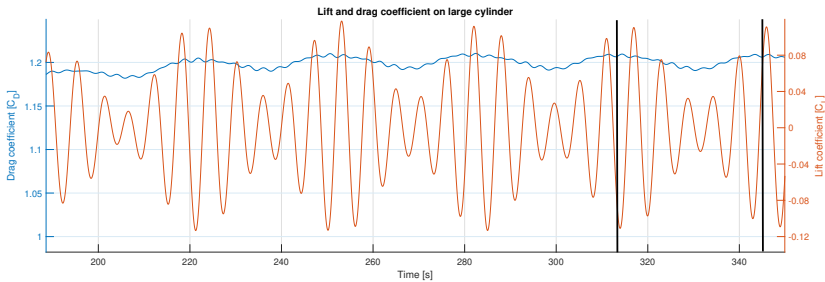
Figure 6.12: Period between two vortex dislocation cycles

After observing the wake structures of the 15D cylinder over a longer period, it is evident that the N-cell region stretches further down in the wake of the large cylinder. In Figure 6.8a in Section 6.3, the N-cell region was found to be $-1 > z/D > -7$. However, by studying the snapshots during the dislocation process the N-cell vortices can be observed to stretch as far as $z/D = -10$. The division of the different cell-regions can be seen in Figure 6.13. The S-cell region is not visible in the figure because the Reynolds number for the small cylinder is so small that the vortices are not detectable.

Additional figures from the 15D step cylinder simulations can be observed in Appendix A. The figures show the instantaneous pressure distributions for different cutting planes for the 15D cylinder. They are included as an addition to the discussion, because they describe well how the pressure in the wake changes in the spanwise direction.
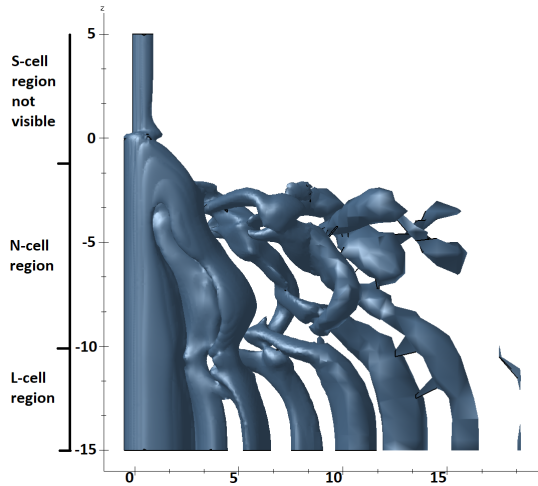
Figure 6.13: Different cell-regions for the 15D step cylinder, t=332.5

6.5 Dual step cylinder simulations

By having performed several simulations for the step cylinder (5D, 10D and 15D), we have familiarized with the nature of the wake, the forming of distinct vortical structures, and the process of vortex dislocation. The next step in the thesis is to perform simulations for dual step cylinders. The goal of the simulations is to observe how different cylinder lengths will influence the wake. The flow characteristics of the dual step cylinder will be investigated, as well as comparison with the single step cylinder. To make the simulations comparable with the single step cylinders, Reynolds number and the diameter ratio D/d will remain unchanged, meaning only the length of the large cylinder will change. The geometry, as well as the global parameters can be seen in Figure 6.14 and Table 6.2.
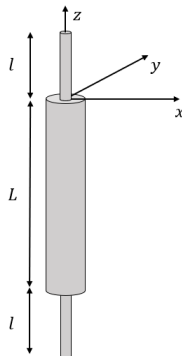
Figure 6.14: Dual step cylinder geometry

Computational domain parameters	
Domain length L_X	28 m
Domain width L_Y	16 m
Domain height $L_Z + l_Z$	10 m
Cylinder dimensions	
Small cylinder height l	5 m
Small cylinder diameter d	0.2 m
Large cylinder height L	VARIABLE
Large cylinder diameter D	1 m
Flow parameters	
Reynolds number	150

Table 6.2: Parameters used in the dual step cylinder simulations

The same domain and mesh configuration is used for the 20D dual step cylinder, to ensure consistency. The total number of cells in the computational domain is at this point is 3.7 million. With this high number of cells in the model we are approaching the limit of the computer power available for the work on this thesis, as the simulation at this point takes 3-4 days. At this point in the simulation process it becomes even more evident that the preliminary study of grid and domain management is extremely important.

The dual step simulation is run for 300 seconds and the lift and drag coefficients on the large cylinder can be seen in Figure 6.15. The first interesting observation that can be made is how the long oscillation of the drag coefficient (blue line) is not as significant as for the 15D single step cylinder (Figure 6.10). Moreover, during the period between 150 and 300 seconds the large cylinder experiences 3 "peaks" in drag coefficient, whereas for the 15D cylinder the number of peaks in that range is 5. If we draw a straight comparison to the vortex dislocations, this difference indicates that the 20D dual step cylinder has longer dislocation periods than the 15D single step cylinder. The distance between two peaks for the 20D cylinder is measured to be 40 seconds.
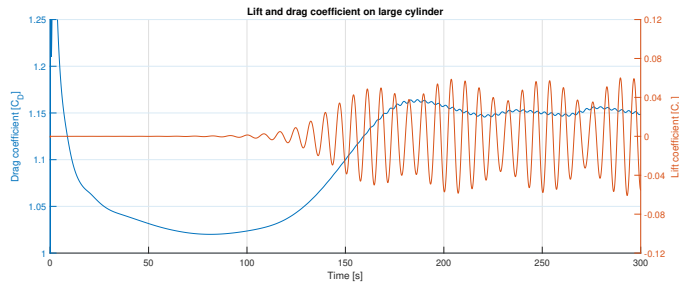
Figure 6.15: Comparison of lift and drag coefficient on the large cylinder for the 20D dual step cylinder, D/d = 5 and Re_D = 150

6.6 Vortex structure of 20D dual step cylinder

Figure 6.16 shows the isosurface of λ_2 = -0.01 of 5 different time instances for the 20D dual step cylinder. Each snapshot is captured when the "-Y" vortices are shed from the cylinder, thus images (a)-(e) show five consecutive -Y vortices. The figures show how both steps have an influence on the wake behind the large cylinder. The vortex structure is visibly symmetric about the center of the large cylinder, which makes sense considering the uniform inflow velocity and the symmetric geometry. The extent of the L-cell region is depicted with red lines. During the period between 271.5 and 299 seconds the region decreases considerably in size as the influence from both the upper and the lower step gradually increases. At the largest, the L-cell region can be measured to be approximately 7D, while at the smallest the L-cell region can be measured to be no longer than 4D.

From the simulation snapshots we can observe that the dislocation process is visible from time instance (c) 285. The connection of the vortices is observed to occur in the same manner as with the 15D single step cylinder.
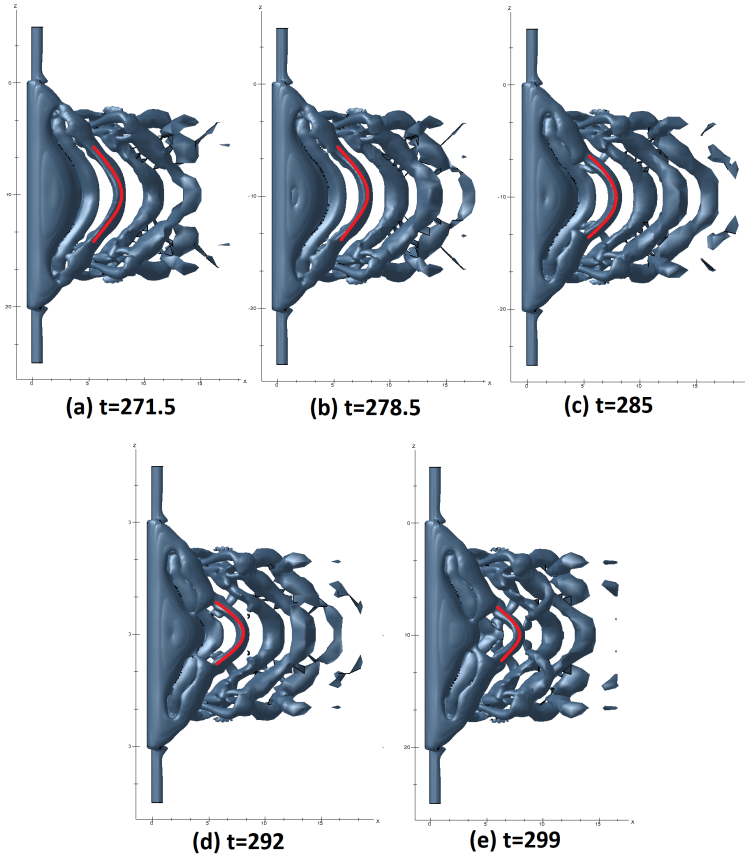
Figure 6.16: Comparison of isosurface $\lambda_2 = -0.01$ for 5 different time instances, 20D dual step cylinder

When it comes to the structure of the flow behind the large cylinder, we can observe hairpin-type vortices (marked in red). This phenomenon have many similarities with the observations made by (McClure et al., 2015). In that study the vortex topology of dual step cylinders with different aspect ratio (spanwise length) is investigated. Figure 6.17 shows the vortex structure for two different spanwise lengths of the large cylinder. The diameter ratio is in both images D/d = 2, so vortex shedding is occurring for the small cylinders. In the study they observe that the spanwise length of the hairpin vortices diminish with decreasing aspect ratio. Because the diameter ratios in the study are different to the diameter ratio in this thesis, direct comparison must be done carefully. However, a comparison may reveal patterns or trends, and in this case by comparing the current 20D simulation with the result from the study we can further extend the reasoning behind the influence

of aspect ratio. The hairpin vortices shed behind the large cylinder in the simulation are clearly more stretched out, and spans over a longer distance in the spanwise direction as Figure 6.16.
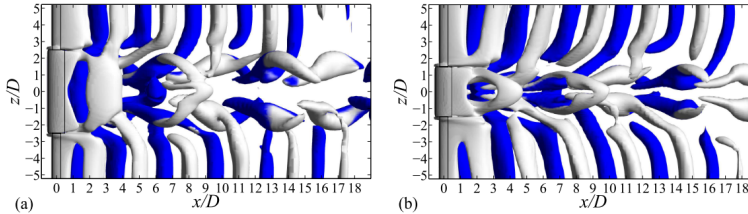
Figure 6.17: Isosurface of $\lambda_2 = 0.01$ for D/d = 2 and (a) L/D = 5 (b) L/D = 3, (McClure et al., 2015)

It is obvious from the 20D dual step cylinder case that the upper and lower step has a great influence on the wake behind the large cylinder. The two N-cell regions are observed to almost meet, and to make connections with each other. The length of the large cylinder is just long enough to separate the two flow regimes, which is the reason for the short spanwise L-cell region. The region is is barely visible, especially in the middle of the dislocation process, in image (e). To get an even better understanding of the interaction of the two steps, and to observe whether they influence each other a new simulation is run for a 30D dual step cylinder.

6.7 30D dual step cylinder

A 30D dual step cylinder simulation is run for 300 seconds to capture a well developed flow. For the 30D simulations the total number of cells in the computational domain is 7.5 million, and the calculation process lasts up to one week. The threshold for what is considered "efficient" has been reached, and for simulations with more cells, even stronger computing power should be applied.

Snapshots of the λ_2 isosurface of the 30D dual step cylinder can be seen in Figure 6.18. The initial observation that can be made is that the L-cell region is considerably longer, which is expected as the previous simulations on the 20D cylinder revealed the influencing limits of the N-cell vortices. Before the dislocation occurs, the L-cell region is measured to be approximately 16D, visual in Figure 6.18 (a). The dislocation process then is initiated, and the influence of the N-cell vortices gradually increases. At the smallest the L-cell region is no more than 7D. The N-cell region is therefore measured to be approximately 11D, from both sides. This is in fact very similar to both the 20D dual step, and the 15D single step cylinder.
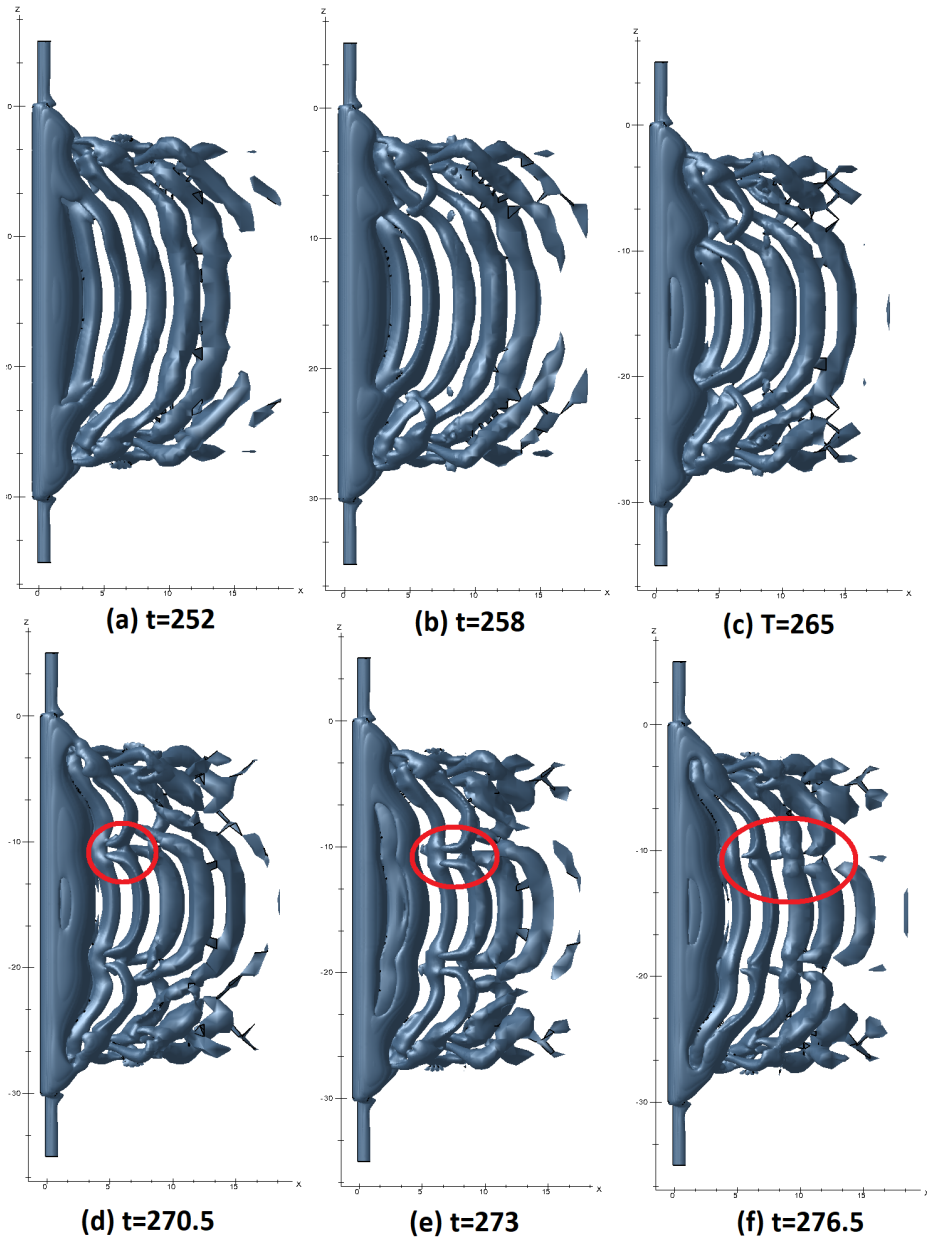
Figure 6.18: Comparison of isosurface λ_2 = -0.01 for 6 different time instances, 30D dual step cylinder

An interesting observation that is made at the end of a dislocation cycle is how two distinct streamwise vortices stretch out in the interaction zone between the N-cell and L-cell regions. This observation is marked with red circles in Figure 6.18 (d), (e) and (f), and is visual on four consecutive vortices shed. They are visible for a total of 8-9 seconds, before they seize to be created. It is difficult to say what causes these effects, and why the N and L-cell vortices doe not form direct connections during this transition from the dislocation. The phenomenon however does show resemblance with the ***modes*** presented in the literature review.

(a) Mode A, Re = 200, spanwise wavelength of 4D   **(b)** Mode B, Re = 270, spanwise wavelength of 1D
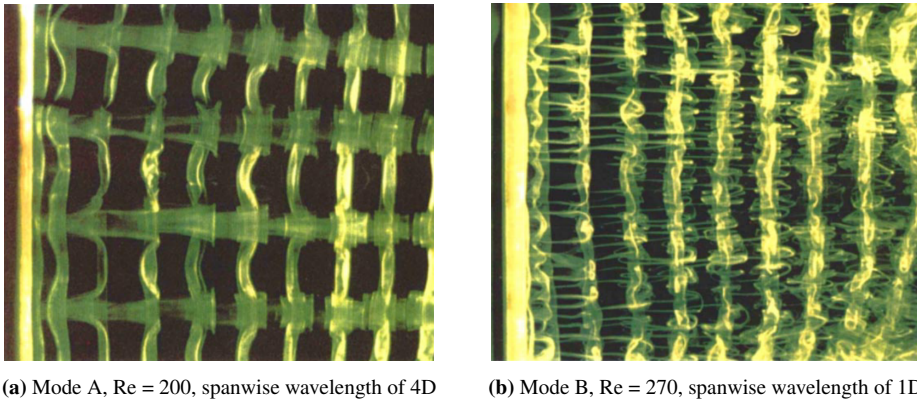
Figure 6.19: Experimental visualization of mode A and B (Williamson, 1996)

The spanwise wavelength of the streamwise vortices is measured to be between 1-2D. This is not consistent with the findings of (Williamson, 1996), where Mode A with 4D wavelengths was detected for Reynolds numbers of 200. With Re = 150, it is reasonable to assume that these "fingers" will have larger wavelengths, but this is not the case. Therefore no direct connection can be made between the observed phenomenon and the modes.

Chapter 7

Conclusion and further work

7.1 Conclusion

This thesis presents the research and numerical investigations on the topic of viscous flow around circular cylinders, and step cylinders. The first part of the thesis works as an introduction to the theory of viscous fluid flows and the main concepts behind flow around circular cylinders. The next part of the thesis involves a literature review presenting the most relevant research and findings from studies performed for the main topics of this thesis. Moreover, an introduction to computational fluid dynamics is given, as well as the theory behind the numerical framework of CFD-solvers. The actual simulations in this thesis are performed in the CFD-software FINE/Marine. Geometry, computational domain and mesh configuration is performed in HEXPRESS, the numerical solving is performed with the ISIS-CFD solver, and the post-processing is performed in CFView. All mentioned components are a part of the software designed by NUMECA. The main objective of the thesis is to explore the flow development around circular step cylinders of different lengths.

The initial simulations in the thesis were performed for a 2D cylinder case. This was done in order to get a basic understanding of how the software worked, and to gain valuable experience in setting up the geometry, meshing and the numerical model. The results from the validation case showed that the accuracy of the model was highly dependent on three important factors, namely mesh configuration/refinement, computational domain size and time step. By performing convergence studies of different mesh refinement configurations it was possible to observe how many cells were needed to get a converged solution. In addition the placement of the smallest cells proved very important for the results. Fine refinement close to the cylinder surface and in the wake gave the best results. The computational domain was created on the basis of understanding the applied boundary conditions. The best results were obtained when the properties of at the boundaries did not affect the flow around the cylinder. The time step sensitivity analysis revealed the importance of applying a sufficiently small time time step suitable for the applied mesh. A too large time step indicated a not well converged solution, while a too small time step

indicated unnecessarily long computational time. The results from the case study were in good agreement with the available literature, and values like drag coefficient C_D, Strouhal number and RMS of the lift coefficient were consistent with previous studies. The case study formed the important basis when transitioning to the three-dimensional regime.

Simulations were performed for different length step cylinders. All simulations were conducted for Reynolds number, $Re_D = 150$ and diameter ratio $D/d = 5$ for the sake of consistency. The initial simulations for the 5D step cylinder showed little effect of the step, as the spanwise length was to small to capture the full development in the wake. However, first signs of downwash from the step were visible. For the 10 and 15D step cylinders, the effect of the step was very visible. The disturbance from the step created significant downwash, and oblique shedding was clearly visible in the wake behind the large step. The fine mesh that was applied in the region around the step and in the wake of the cylinders gave satisfactory results. The flow in the junction between the large and the small cylinder was visually rotational, and in agreement with the early stages of junction and edge vortex formation. In addition, the vortex structures in the wake were captured well with the λ_2 vortex detection. The influence of the step was measured to stretch as far as 10D into the wake of the large cylinder, also referred to as the N-cell region. The more interesting observations made for the 15D step cylinder simulations was the long oscillating drag coefficient frequency that described the vortex dislocation process. The development of the dislocation process was thoroughly described, with results comparable to the important study of (Tian et al., 2017a).

More simulations were conducted for dual step cylinders, with the intent of investigating the influence of different spanwise lengths of the large cylinder. For the 20D cylinder the same vortex dislocation process was observed as for the 15D single step cylinder. With the contribution from both the upper and the lower step, the L-cell region changed much in size. Moreover, so-called hairpin vortices could be observed in the wake of the large cylinder, with maximum deflection at the "climax" of the dislocation process. As the N-cell region was measured to be approximately 10D at the longest, the L-cell region almost disappeared for the 20D cylinder. Simulations of a 30D dual step cylinder revealed that the N-cell region reached a maximum of 11D from both sides, and that the L-cell region now was 7D. An interesting observation made for the 30D simulations were the streamwise vortex fingers stretching out in the interaction between the N-cell and L-cell regions. The vortices showed resemblance to the modes first described by Gerrard (1978).

In conclusion the simulations performed in the thesis are in agreement with the most relevant studies on this topic. This thesis has investigated a diameter ratio and length ratios different to earlier studies, but the results are consistent with the literature. The same flow characteristics around the step are visible, as well as the characteristics of the vortex structures in the wake. However, after performing the simulations it is clear that further investigations will be required to obtain a robust understanding of the flow characteristics of the step cylinder flows. The following section gives some recommendations for further work that can potentially strengthen the research.

7.2 Further work

Recommendations for further work and possible improvements of the single and dual step simulations include:

- Exploring different values of Reynolds number. As the Reynolds number used in this thesis (150) is considerably small, and in the laminar shedding regime, the effects around the step and in the wake are subtle. With increasing Re, the flow will become more turbulent, and other characteristics will be possible to observe. It would be specially interesting to change the Reynolds number for the dual step cylinder, as there are a limited number of studies for that particular case.

- Investigating a change in diameter ratio D/d. The diameter ratio has been static throughout the simulations in the thesis, and it would be interesting to observe how the wake characteristics will change when more apparent shedding occurs behind the small cylinder.

- It would be very interesting to apply a very fine mesh around the step to investigate the absolute smallest details around the step, for higher Reynolds numbers. By doing this it is possible to find the origin of the junction and edge vortices, and how they interact with each other and mix in the wake.

- Investigating the different shedding frequencies in the wake, and monitor what are the dominating frequencies. In other words; which cylinder geometries give which frequencies, and which geometries are the preferred from a "dynamic response" point of view.

Bibliography

Calhoun, D., 2002. A cartesian grid method for solving the two-dimensional streamfunction-vorticity equations in irregular regions. Journal of Computational Physics Vol. 176, pp. 231–275.

Cengel, Y., Cimbala, J., 2010. Fluid Mechanics Fundamentals and Applications. 2 ed., McGraw-Hill.

Chen, H., Patel, V., Ju, S., 1990. Solutions of reynolds-averaged navier-stokes equations for three-dimensional incompressible flows. Journal of Computational Physics 88, pp. 305–336.

Chua, L., Liu, C., Chan, W., 1998. Measurements of a step cylinder. International Communications in Heat and Mass Transfer Vol. 25, pp. 205–215.

Dunn, W., Tavoularis, S., 2006. Experimental studies of vortices shed from cylinders with a step-change in diameter. Journal of Fluid Mechanics Vol. 555, pp. 409–437.

Eca, L., Vaz, G., Rosetti, G., Pereira, F., 2014. On the numerical prediction of the flow around smooth circular cylinders. International Conference on Ocean, Offshore and Arctic Engineering OMAE2014-23230, V002T08A013.

Faltinsen, O., 1990. Sea Loads on Ships and Offshore Structures. 1 ed., Cambridge University Press.

Gerrard, J., 1978. The wakes of cylindrical bluff bodies at low reynolds number. Philosophical Transactions of the Royal Society of London Vol. 288, pp. 351–382.

Heseltine, J., 2003. Flow around a circular cylinder with a free end. Univerity of Saskatchewan Canada , M.Sc.

Kolár, V., 2007. Vortex identification: New requirements and limitations. International Journal of Heat and Fluid Flow Vol. 28, pp. 638–652.

Lamb, H., 1975. Hydrodynamics. Cambridge Mathematical Library. 6 ed., Cambridge University Press.

Landahl, M., Mollo-Christensen, E., 1992. Turbulence and Random Processes in Fluid Mechanics. 2 ed., Cambridge University Press.

Lewis, C., Gharib, M., 1992. An exploration of the wake three dimensionalities caused by a local discontinuity in cylinder diameter. Physics of Fluids Vol. 104, pp. 104–117.

McClure, J., Morton, C., Yarusevych, S., 2015. Flow development and structural loading on dual step cylinders in laminar shedding regime. Physics of Fluids Vol. 27.

Mortensen, O., 2019. Simulation of viscous flow around a curved cylinder in crossflow. Norwegian Institute of Science and Technology, Department of Marine Technology 1.

Morton, C., Yarusevych, S. Carvajal-Mariscaal, I., 2009. Study of flow over a step cylinder. Applied Mechanics and Materials Vol. 15, pp. 9–14.

Morton, C., Yarusevych, S., 2010. A combined experimental and numerical study of flow past a single step cylinder. ASME 2010, US-European Fluids Engineering Summer meeting and 8th international conference , pp. 1209–1220.

Moukalled, F., Mangani, L., Darwish, M., 2016. The Finite Volume Method in Computational Fluid Dynamics. 113. 1 ed., Springer International Publishing.

Norberg, C., 1992. An experimental study of the flow around cylinders joined with a step in the diameter. Australasian Fluid Mechanic Conference Vol. 1, pp. 507–510.

NUMECA, 2020. Online Documentation Platform , FINE/Marine 8.2. . [Online; accessed 18-January-2020].

Okamoto, S., Sunabashiri, Y., 1992. Vortex shedding from a circular cylinder of finite length placed on a ground plane. The American Society of Mechanical Engineers Vol. 114, pp. 512–521.

Park, C., Lee, S., 2000. Free end effects on the near wake flow structure behind a finite circular cylinder. Journal of Wind Engineering and Industrial Aerodynamics Vol. 88, pp. 231–246.

Schlichting, H., Gersten, K., 2017. Boundary-Layer Theory. 9 ed., Springer-Verlag Berlin Heidelberg.

Sumer, B., Fredsøe, J., 1997. Hydrodynamics around Cylindrical Structures, Advansed Series on Ocean Engineering. 26 ed., World Scientific Publishing Co. Pte. Ltd.

Tian, C., Jiang, F., Pettersen, B., Andersson, H., 2017. Numerical investigation of flow around a step cylinder. Proceedings of 9th National Conference on Computational Mechanics , pp. 369–384.

Tian, C., Jiang, F., Pettersen, B., Andersson, H., 2017a. Antisymmetric vortex interactions in the wake behind a step cylinder. National Conferance on Computational Mechanics Vol. 29.

Tritton, D., 1959. Experiments on the flow past a circular cylinder at low reynolds numbers. Journal of Fluid Mechanics Vol. 6, pp. 547–567.

Valles, B., Andersson, H., 2002. Direct-mode interactions in the wake behind a stepped cylinder. American Institute of Physics Vol. 14.

Versteeg, H., Malalasekera, W., 2007. An Introduction to Computational Fluid Dynamics, The Finite Volume Method. 2 ed., Pearson Education Limited.

Wang, Z., Fan, J., Cen, K., 2009. Immersed boundary method for the simulation of 2d viscous flow based on vorticity-velocity formulations. Journal of Computational Physics Vol. 228, pp. 1504–1520.

White, F., 2005. Viscous Fluid Flow. 3 ed., McGraw-Hill.

Williamson, C., 1988. Defining a universal and continuous strouhal-reynolds number relationship for the laminar vortex shedding of a circular cylinder. Physics of Fluids Vol. 31.

Williamson, C., 1992. The natural and forced formation of spot-like vortex dislocations in the transition of a wake. Journal of Fluid Mechanics Vol. 243, pp. 393–441. Vortex Cylinder.

Williamson, C., 1996. Vortex dynamics in the cylinder wake. Annual Reviews Inc. Fluid Mech. 1996 Vol. 28, pp. 477–539.

Zdravkovich, M., 1997. Flow over Circular Cylinders. 1 ed., Oxford University Press.
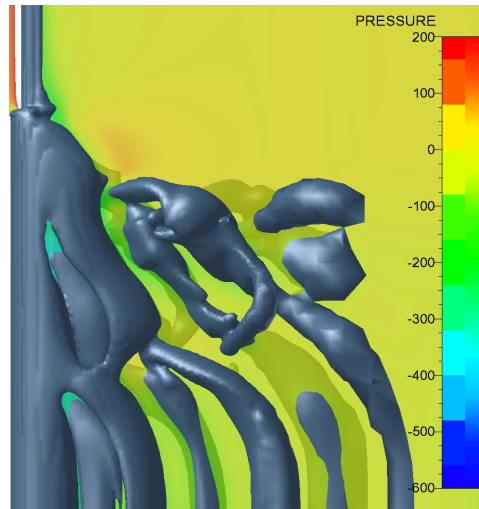
List of Tables

List of Figures

Appendix

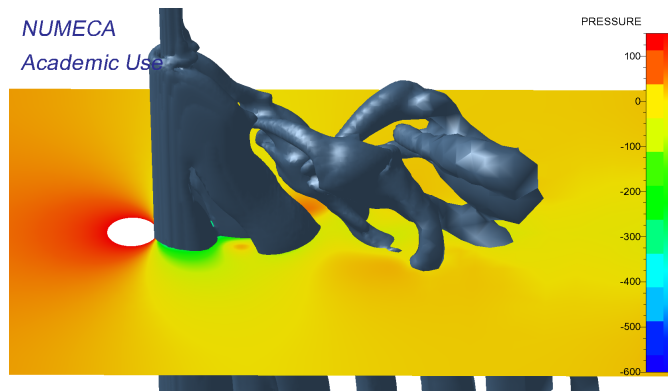## A. 15D single step cylinder plots (360s)
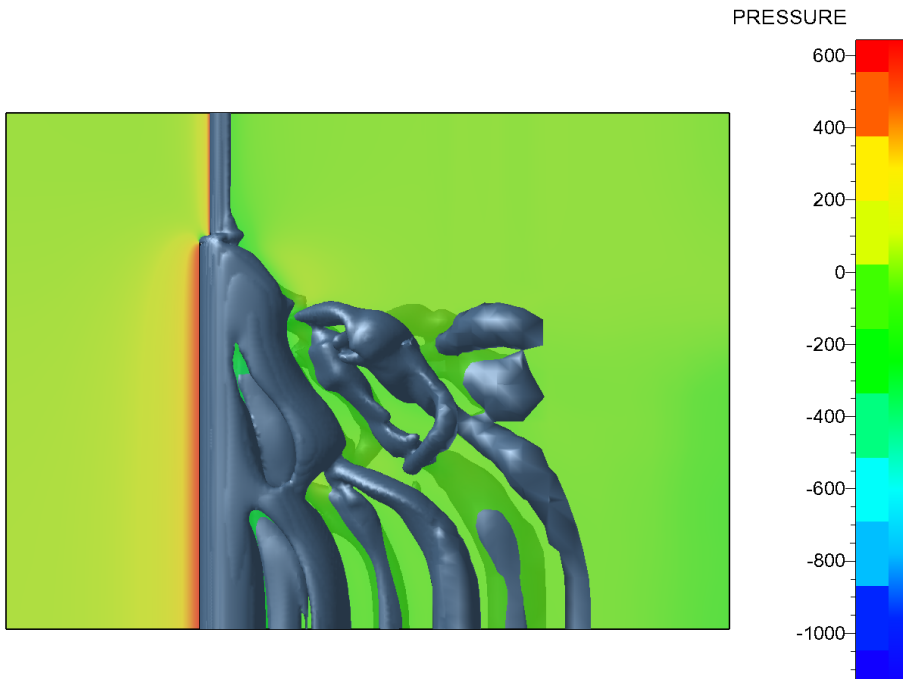
Figure 7.1: Isosurface of $\lambda_2 = -0.01$ and pressure distribution for 15D step cylinder
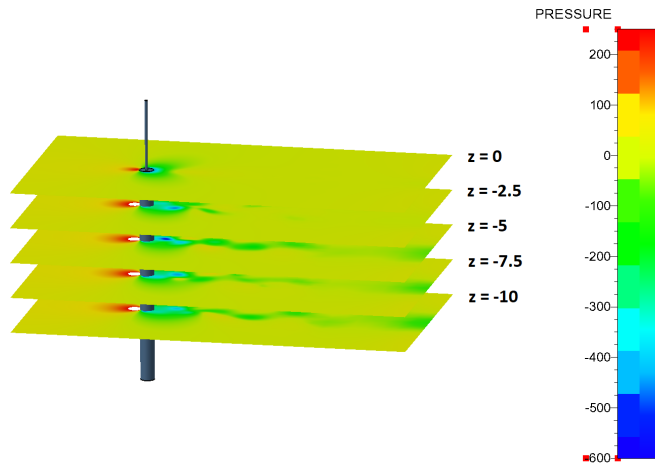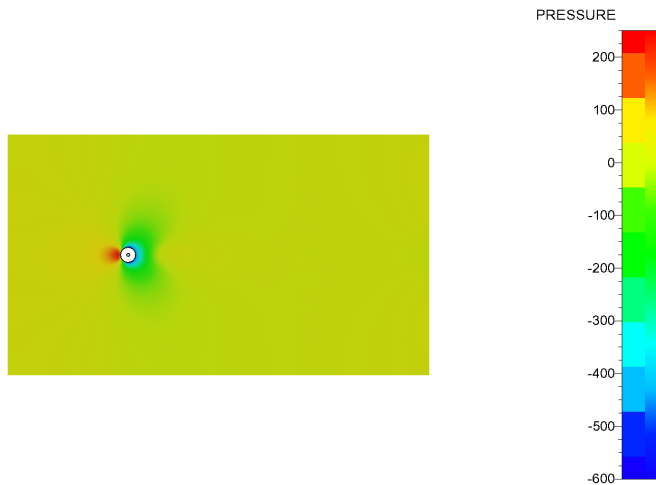
Figure 7.2: Isosurface of $\lambda_2 = -0.01$ plotted with lower values of pressure distribution
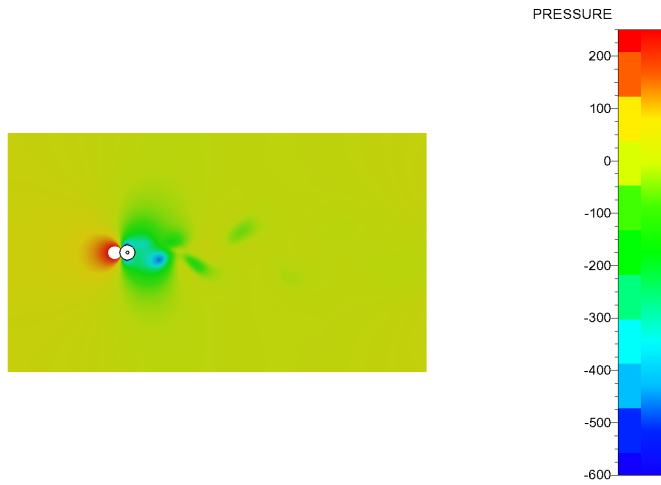

Figure 7.3: Isosurface of $\lambda_2 = -0.01$ and cutting plane at z = -0.7 with pressure distribution. We can see that the low pressure regions are coinciding with the vortex cores.
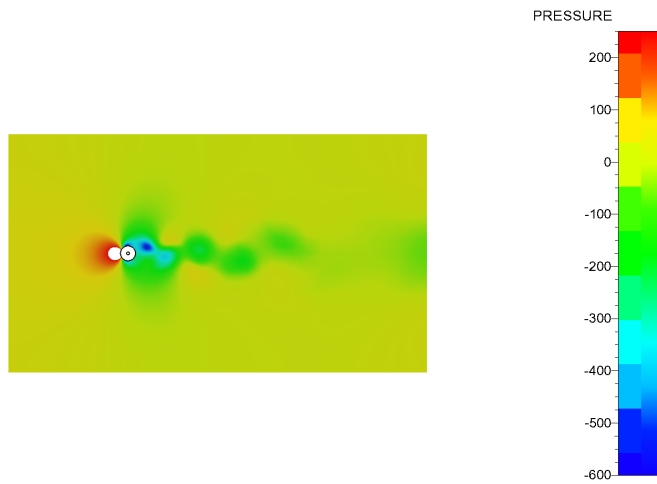
Figure 7.4: Pressure distribution for five different cutting planes for the 15D step cylinder, z = 0, z = -2.5, z = -5, z = -7.5, z = -10
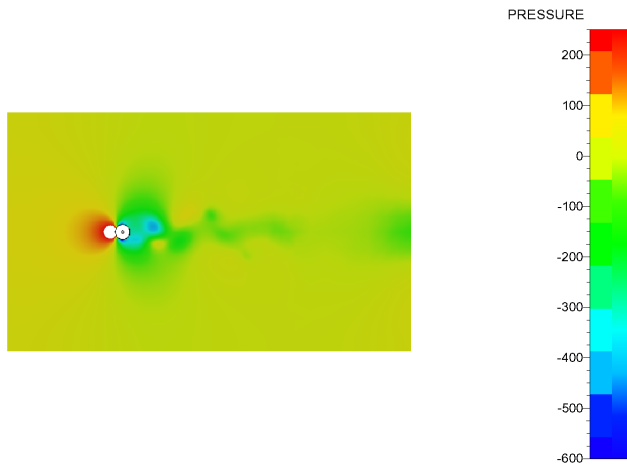

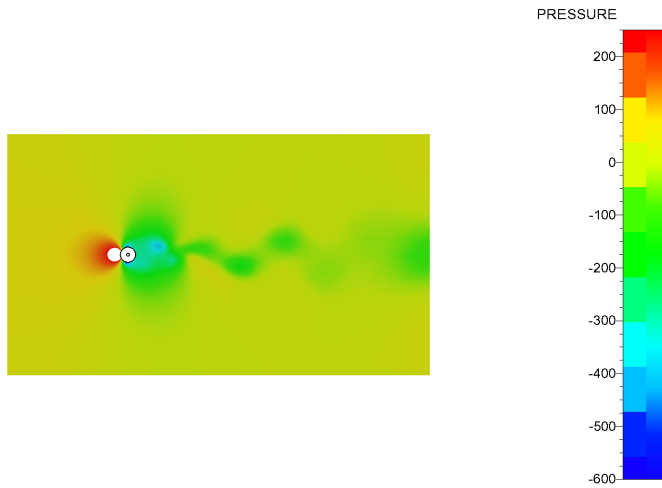**Figure 7.5:** Pressure distribution for cutting plane z = 0

Figure 7.6: Pressure distribution for cutting plane z = -2.5

Figure 7.7: Pressure distribution for cutting plane z = -5

Figure 7.8: Pressure distribution for cutting plane z = -7.5

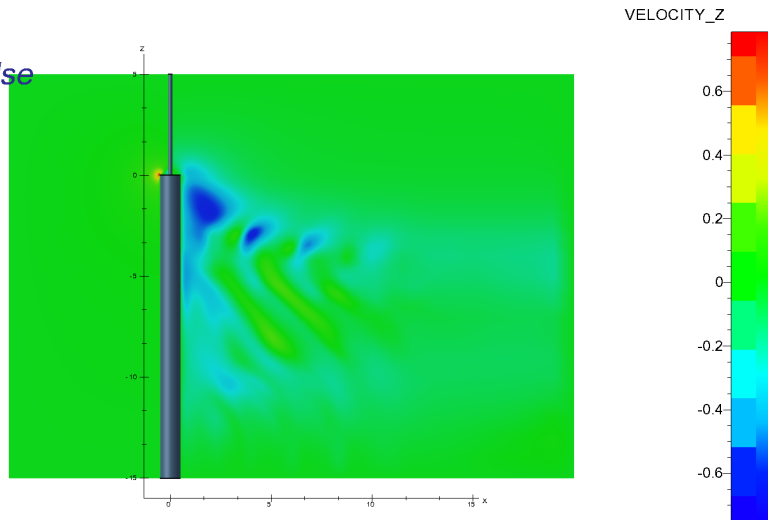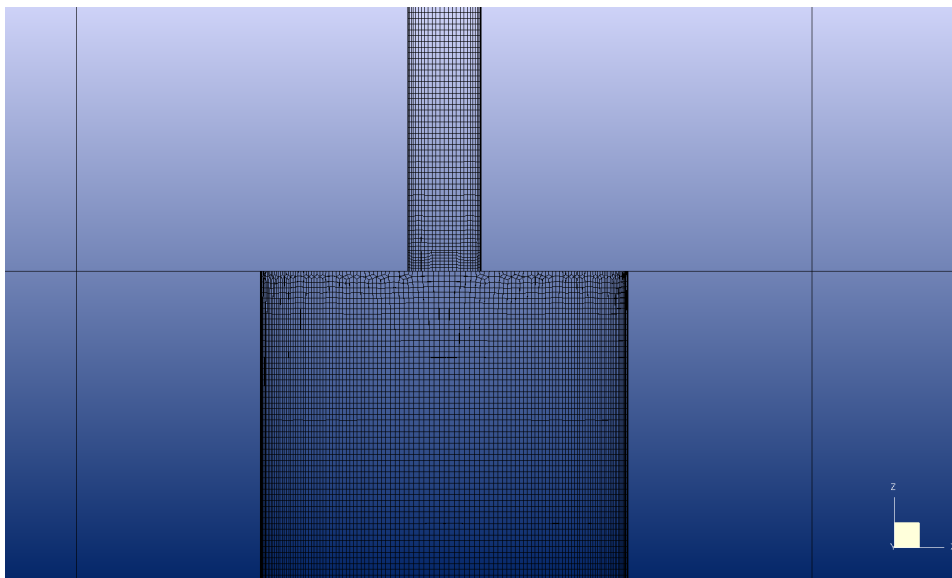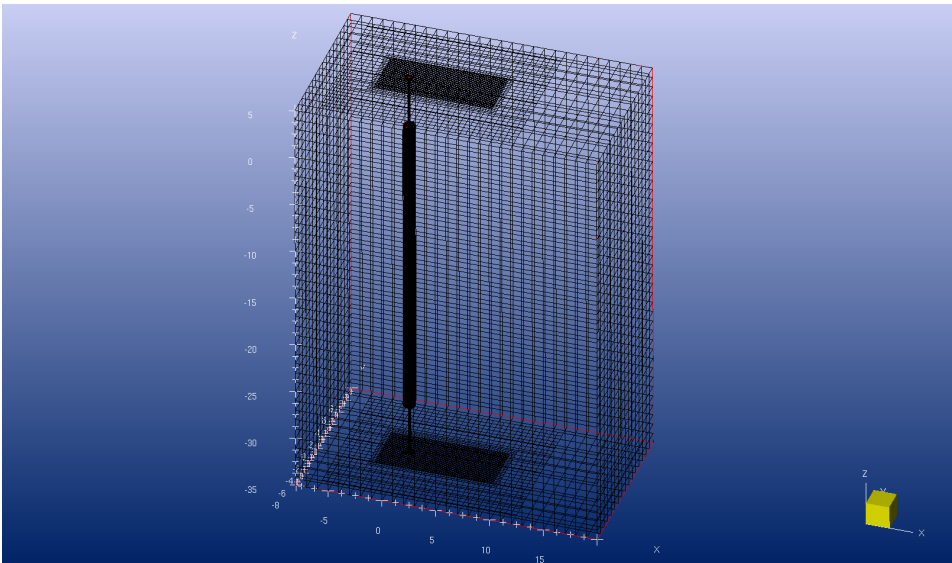**Figure 7.9:** Pressure distribution for cutting plane z = -10

Figure 7.10: Velocity in z-direction for 15D step cylinder, highlighting the downwash behind the step

Figure 7.11: Mesh refinement close to the step for the 15-30D cylinder simulations

Figure 7.12: Mesh configuration for the 30D dual step cylinder

B. Matlab Code

Calculating and plotting lift and drag coefficients

```matlab
1  %% Plotting lift and drag forces
2  clc
3
4  %% Importing data from simulation
5
6  run_x = importdata('eff_Fx_dual_step1_run3.dat');
7  run_x.data;
8
9  run_y = importdata('eff_Fy_dual_step1_run3.dat');
10 run_y.data;
11
12 %% Drag force and drag coefficient
13 %————————————————————————————————
14 %% LARGE CYLINDER
15
16 FD_large_cyl = run_x.data(:,4);
17 time_drag = run_x.data(:,1);
18
19 figure(1)
20 plot(time_drag,FD_large_cyl)
21 axis([0 350 10000 13000])
22 xlabel('Time [s]')
23 ylabel('Drag force [F_D]')
24 grid on
25 title('Drag force on large step cylinder')
26
27 CD_large_cyl = FD_large_cyl/(500*20);
28
29 figure(2)
30 plot(time_drag,CD_large_cyl)
31 axis([0 350 1 1.3])
32 xlabel('Time [s]')
33 ylabel('Drag coefficient [C_D]')
34 grid on
35 title('Drag coefficient on large step cylinder')
36
37 %% SMALL CYLINDER
38
39 FD_small_cyl = run_x.data(:,5);
40 time_drag = run_x.data(:,1);
```

```matlab
41
42  figure(3)
43  plot(time_drag,FD_small_cyl)
44  axis([0 350 920 940])
45  xlabel('Time [s]')
46  ylabel('Drag force [F_D]')
47  grid on
48  title('Drag force on small step cylinder')
49
50  CD_small_cyl = FD_small_cyl/(500*0.2*5);
51
52  figure(4)
53  plot(time_drag,CD_small_cyl)
54  axis([0 350 1.84 1.88])
55  xlabel('Time [s]')
56  ylabel('Drag coefficient [C_D]')
57  grid on
58  title('Drag coefficient on small step cylinder')
59
60  %% Lift force and lift coefficient
61  %———————————————————————————————
62  %% LARGE CYLINDER
63
64  FL_large_cyl = run_y.data(:,4);
65  time_lift = run_y.data(:,1);
66
67  a = [278 278];
68  b = [-1000 1000];
69
70  figure(5)
71  plot(time_lift,FL_large_cyl)
72  axis([0 350 -1000 1000])
73  xlabel('Time [s]')
74  ylabel('Lift force [F_L]')
75  grid on
76  title('Lift force on large step cylinder')
77  hold on
78  plot(a,b,'LineWidth',1)
79
80  Cl_large_cyl = FL_large_cyl/(500*20);
81
82  figure(6)
83  plot(time_lift,Cl_large_cyl)
84  axis([0 350 -0.13 0.13])
85  xlabel('Time [s]')
```

```matlab
86   ylabel('Lift coefficient [C_L]')
87   grid on
88   title('Lift coefficient on large step cylinder')
89
90   %% SMALL CYLINDER
91
92   FL_small_cyl = run_y.data(:,5);
93   time_lift = run_y.data(:,1);
94
95   figure(7)
96   plot(time_lift, FL_small_cyl)
97   axis([0 350 -0.7 0.4])
98   xlabel('Time [s]')
99   ylabel('Lift force [F_L]')
100  grid on
101  title('Lift force on small step cylinder')
102
103  Cl_small_cyl = FL_small_cyl/(500*0.2*5);
104
105  figure(8)
106  plot(time_lift, Cl_small_cyl)
107  axis([0 350 -0.0015 0.0007])
108  xlabel('Time [s]')
109  ylabel('Lift coefficient [C_L]')
110  grid on
111  title('Lift coefficient on small step cylinder')
112
113  %% Lift and drag in same plot
114
115  % figure(9)
116  % plot(time_drag, CD_large_cyl)
117  % axis([200 300 -0.2 2])
118  % hold on
119  % plot(time_lift, Cl_large_cyl)
120  % xlabel('Time [s]')
121  % ylabel('Lift  and drag coefficient [C_L, C_D]')
122  % grid on
123  % title('Lift and drag coefficients on large cylinder')
124
125
126  figure (10)
127  [ax,h1,h2] = plotyy(time_lift, CD_large_cyl, time_lift,
        Cl_large_cyl)
128  set(ax(1),'YLim',[1 1.25])
129  set(ax(2),'YLim',[-0.12 0.12])
```

```matlab
130   set(ax(1),'Box','off')
131   set(ax(2),'Box','off')
132   set(ax(1),'YTick',[1:.05:1.25])
133   set(ax(2),'YTick',[-1.12:0.04:0.12])
134   grid on
135   title('Lift and drag coefficient on large cylinder')
136   xlabel('Time [s]')
137   ylabel(ax(1),'Drag coefficient [C_D]') % left y-axis
138   ylabel(ax(2),'Lift coefficient [C_L]') % right y-axis
```

Calculating and plotting velocity profiles

```matlab
1   %% PLotting velocity profiles at top of cylinder
2   clc
3   clear
4   %% Calculation
5
6   A = importdata('vel_profile_2D.dat');
7   A.data;
8
9   X = A.data(:,1);
10  Y = A.data(:,2);
11
12  X1 = 1.1.*X;
13  X1 = X1(1:61);
14  X1(62) = 5;
15
16
17  Y1 = 1.03.*Y;
18  Y1 = Y1(1:61);
19  Y1(62) = 1;
20
21  X2 = 1.0.*X;
22  X2 = X2(1:67);
23  X2(68) = 8.2;
24  X2(69) = 9;
25
26  Y2 = 0.99.*Y;
27  Y2 = Y2(1:67);
28  Y2(68) = 1.015;
29  Y2(69) = 1;
30
```

```
31  L1 = [0 10];
32  L2 = [1 1];
33
34  figure(1)
35  plot(X1,Y1)
36  title('Velocity profile from cylinder top to end of domain:
       DOMAIN 1 2 and 3')
37  xlabel('Distance from cylinder top [m]')
38  ylabel('Velocity [m/s]')
39  axis([0 10 0.9 1.5])
40  grid off
41  hold on
42  plot(X,Y)
43  plot(X2,Y2)
44  plot(L1,L2)
45  legend('Domain 1','Domain 2','Domain 3')
```

Calculating Root Mean Square

```
1   %% Calculating Root Mean Square value of lift coefficient
2   clc
3   clear
4
5   %% Importing data from simulation
6
7   run_x = importdata('eff_Fx_2D_run1.dat');
8   run_x.data;
9
10  run_y = importdata('eff_Fy_2D_run1.dat');
11  run_y.data;
12
13  %% Calculating lift coefficient from 120 to 250 seconds
14
15  FL_large_cyl = run_y.data(:,3);
16  time_lift = run_y.data(:,1);
17
18  figure(3)
19  plot(time_lift,FL_large_cyl)
20  axis([0 250 -200 200])
21  xlabel('Time [s]')
22  ylabel('Lift force [F_L]')
23  grid on
```

```matlab
24  title ('Lift force on cylinder')
25
26  Cl_large_cyl = FL_large_cyl/(500);
27
28  figure (4)
29  plot (time_lift, Cl_large_cyl, '-o')
30  axis ([120 125 -0.4 0.4])
31  xlabel ('Time [s]')
32  ylabel ('Lift coefficient [C_L]')
33  grid on
34  title ('Lift coefficient on cylinder')
35
36  %% calculating root mean square
37
38  A = 2401;
39  B = Cl_large_cyl(A:5000);
40   N = length(B);
41   Y=0;
42   X = zeros (1,N);
43      for i=1:N
44          % B is the variable to read in user input
45              X(i) = sqrt((B(i).^2));
46      end
47        for j=1:N
48              Y = Y+X(j);
49        end
50        Y=Y/N;
51
52      %fprintf ('The root-mean-square value is:%d\n', x_rms)
```